










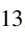





[C_{II}] 158 μ m emission as an indicator of galaxy star formation rate

Lichen Liang^{1,2*} , Robert Feldmann² , Norman Murray^{1,3} , Desika Narayanan^{4,5,6} ,
 Christopher C. Hayward⁷ , Daniel Anglés-Alcázar^{8,7} , Luigi Bassini² , Alexander J. Richings^{9,10} ,
 Claude-André Faucher-Giguère¹¹ , Dongwoo T. Chung^{1,12} , Jennifer Y. H. Chan^{1,12} ,
 Doğa Tolgay^{1,13} , Onur Çatmabacak² , Dušan Kereš¹⁴ , Philip F. Hopkins¹⁵ 

¹Canadian Institute for Theoretical Astrophysics, University of Toronto, 60 St. George Street, Toronto, ON M5S 3H8, Canada

²Institute for Computational Science, University of Zurich, Winterthurerstrasse 190, Zurich CH-8057, Switzerland

³Canada Research Chair in Theoretical Astrophysics

⁴Department of Astronomy, University of Florida, 211 Bryant Space Sciences Center, Gainesville, FL 32611, USA

⁵University of Florida Informatics Institute, 432 Newell Drive, CISE Bldg E251, Gainesville, FL 32611, USA

⁶Cosmic Dawn Center at the Niels Bohr Institute, University of Copenhagen and DTU-Space, Technical University of Denmark, Denmark

⁷Center for Computational Astrophysics, Flatiron Institute, 162 Fifth Avenue, New York, NY 10010, USA

⁸Department of Physics, University of Connecticut, 196 Auditorium Road, U-3046, Storrs, CT 06269-3046, USA

⁹E. A. Milne Centre for Astrophysics, University of Hull, Cottingham Road, Hull, HU6 7RX, UK

¹⁰DAIM, University of Hull, Cottingham Road, Hull, HU6 7RX, UK

¹¹Department of Physics and Astronomy and CIERA, Northwestern University, Evanston, IL 60208, USA

¹²Dunlap Institute for Astronomy and Astrophysics, University of Toronto, 50 St. George Street, Toronto, ON M5S 3H4, Canada

¹³Department of Physics, University of Toronto, 60 St. George Street, Toronto, Ontario M5S 1A7, Canada

¹⁴Department of Physics, Center for Astrophysics and Space Sciences, University of California at San Diego, La Jolla, CA 92093, USA

¹⁵TAPIR, Mailcode 350-17, California Institute of Technology, Pasadena, CA 91125, USA

Accepted 2022. Received 2022; in original form 2022

ABSTRACT

Observations of local star-forming galaxies (SFGs) show a tight correlation between their singly ionized carbon line luminosity ($L_{[\text{CII}]}$) and star formation rate (SFR), suggesting that $L_{[\text{CII}]}$ may be a useful SFR tracer for galaxies. Some other galaxy populations, however, are found to have lower $L_{[\text{CII}]}/\text{SFR}$ than local SFGs, including the infrared-luminous, starburst galaxies at low and high redshifts as well as some moderately star-forming galaxies at the epoch of re-ionization (EoR). The origins of this ‘[C_{II}] deficit’ is unclear. In this work, we study the $L_{[\text{CII}]}$ -SFR relation of galaxies using a sample of $z = 0 - 8$ galaxies with $M_* \approx 10^7 - 5 \times 10^{11} M_\odot$ extracted from cosmological volume and zoom-in simulations from the Feedback in Realistic Environments (FIRE) project. We find a simple analytic expression for $L_{[\text{CII}]}/\text{SFR}$ of galaxies in terms of the following parameters: mass fraction of [C_{II}]-emitting gas ($f_{[\text{CII}]}$), gas metallicity (Z_{gas}), gas density (n_{gas}) and gas depletion time ($t_{\text{dep}} = M_{\text{gas}}/\text{SFR}$). We find two distinct physical regimes: H₂-rich galaxies where t_{dep} is the main driver of the [C_{II}] deficit and H₂-poor galaxies where Z_{gas} is the main driver. The observed [C_{II}] deficit of IR-luminous galaxies and early EoR galaxies, corresponding to the two different regimes, is due to short gas depletion time and low gas metallicity, respectively. Our result indicates that the [C_{II}] deficit is a common phenomenon of galaxies, and caution needs to be taken when applying a constant $L_{[\text{CII}]}$ -to-SFR conversion factor derived from local SFGs to estimate cosmic SFR density at high redshifts and interpret data from upcoming [C_{II}] line intensity mapping experiments.

Key words: evolution — galaxies: high-redshift — galaxies: ISM — infrared: galaxies

1 INTRODUCTION

The census of cosmic star formation from the present day to the highest redshifts imposes a key constraint on galaxy evolution theory and physical cosmology (see *e.g.*, Madau & Dickinson 2014; Dayal & Ferrara 2018, and references therein). The rest-frame ultra-violet (UV) luminosity (L_{UV}) of galaxies, tracing the young, massive stars, is a common star formation rate (SFR) indicator of galaxies (*e.g.* Hao et al. 2011; Kennicutt & Evans 2012). However, a large fraction of

the UV light from galaxies in the Universe is absorbed by interstellar dust and gets re-emitted as thermal radiation at far-infrared (far-IR) wavelength (*e.g.* Fixsen et al. 1998; Takeuchi et al. 2005; Dole et al. 2006; Magnelli et al. 2009; Gruppioni et al. 2013; Burgarella et al. 2013; Whitaker et al. 2017; Salim & Narayanan 2020). Therefore, an accurate estimate of the cosmic SF history depends on a multi-wavelength, UV-to-millimetre (mm) analysis that accounts for both the direct, unobscured stellar light and the dust thermal emission of galaxies over cosmic time.

In practice, however, our capability of constraining the two components of stellar radiation is largely imbalanced (*e.g.* Casey et al.

* Email: lliang@cita.utoronto.ca

2018a). While the rest-frame UV-based, unobscured component has been constrained to up to redshifts $z \sim 15$ (e.g. Bouwens et al. 2007, 2011, 2015, 2019; Oesch et al. 2012, 2016, 2018; Ellis et al. 2013; McLure et al. 2013; Finkelstein et al. 2015; McLeod et al. 2015; Bowler et al. 2020; Naidu et al. 2022; Leethochawalit et al. 2023a,b; Donnan et al. 2023; Harikane et al. 2023) through deep imaging with the *Hubble* and the *James Webb Space Telescopes*, the obscured component is still not well constrained beyond $z \sim 3$ due to the lack of statistically-representative, unbiased galaxy samples in that regime (Casey et al. 2014; Casey et al. 2018a; Dayal & Ferrara 2018; Zavala et al. 2021). It is therefore important to have other SFR diagnostics in addition to UV+IR for early galaxies (see e.g. Khusanova et al. 2021, and references therein).

The $158\ \mu\text{m}$ (900.5 GHz) fine structure transition (${}^2P_{3/2} \rightarrow {}^2P_{1/2}$) of singly ionized carbon ($[\text{C}_{\text{II}}]$) has been proposed as a promising alternative SFR indicator, particularly for high- z galaxies (Hodge & da Cunha 2020). It is a major coolant of the neutral atomic gas of the interstellar medium (ISM) and often the strongest emission line of star-forming galaxies at rest-frame far-IR wavelength (Carilli & Walter 2013). The $[\text{C}_{\text{II}}]$ line of galaxies is usually not much affected by dust extinction (e.g. Abel et al. 2007).

To first order, a correlation between $L_{[\text{C}_{\text{II}}]}$ and global SFR of galaxies is expected. Much of the $[\text{C}_{\text{II}}]$ emission of galaxy originates from the neutral atomic gas regions (Hollenbach & Tielens 1999; Wolfire et al. 2003; Ferrara et al. 2019), where the far-UV (FUV) photons produced by the young O and B-type stars heat the gas via the photoelectric (PE) effect on small dust grains and polycyclic aromatic hydrocarbon (PAH) molecules (Tielens & Hollenbach 1985; Hollenbach et al. 1991; Weingartner & Draine 2001a; Helou et al. 2001). The photo-electrons ejected from the dust grains/PAH molecules collisionally couple to and heat the gas. Since the PE heating rate (\dot{E}_{PE}) traces galaxy SFR, and $L_{[\text{C}_{\text{II}}]}$ balances \dot{E}_{PE} given that $[\text{C}_{\text{II}}]$ line is the dominant coolant in those regions (assuming a thermal equilibrium), $L_{[\text{C}_{\text{II}}]}$ should therefore be correlated to SFR. Observations of local star-forming galaxies (SFGs) have indeed found a linear correlation between $L_{[\text{C}_{\text{II}}]}$ and SFR over the broad SFR range of $\approx 10^{-4} - 10 M_{\odot} \text{yr}^{-1}$ (e.g. Stacey et al. 1991; Leech et al. 1999; Boselli et al. 2002; De Looze et al. 2011, 2014; Herrera-Camus et al. 2015). These observations suggest that the $[\text{C}_{\text{II}}]$ line can be a useful SFR indicator for galaxies.

There is evidence, however, showing that this scaling relationship does not hold in all environments. For instance, observations find that local ultra-luminous infrared galaxies (ULIRGs, galaxies having $L_{\text{IR}} \geq 10^{12} L_{\odot}$) show a significant lower $L_{[\text{C}_{\text{II}}]}/L_{\text{IR}}$ ($\sim L_{[\text{C}_{\text{II}}]}/\text{SFR}$) ratio than normal SFGs by up to an order of magnitude (Malhotra et al. 1997, 2001; Luhman et al. 1998, 2003; Brauher et al. 2008; Farrah et al. 2013; Magdis et al. 2014), the so-called ‘ $[\text{C}_{\text{II}}]$ deficit’ problem. This result was at first revealed with the *Infrared Space Observatory* (ISO; Kessler et al. 1996) and later confirmed by observations with the *Herschel Space Observatory* (hereafter *Herschel*; Pilbratt et al. 2010) that has improved far-IR observing capabilities. Subsequent observations with *Herschel* also show that the $[\text{C}_{\text{II}}]$ deficit extends to lower L_{IR} and that the $L_{[\text{C}_{\text{II}}]}/L_{\text{IR}}$ ratio of galaxies exhibits a continuous decrease with increasing L_{IR} at $L_{\text{IR}} \geq 10^{11} L_{\odot}$ (e.g. Graciá-Carpio et al. 2011; Sargsyan et al. 2012; Díaz-Santos et al. 2013; Cormier et al. 2015; Herrera-Camus et al. 2015, 2018; Contursi et al. 2017; Díaz-Santos et al. 2017; Hughes et al. 2017; Smith et al. 2017).

Studies have investigated the $L_{[\text{C}_{\text{II}}]}$ -SFR relation of galaxies at higher redshifts (e.g. Stacey et al. 2010; Gullberg et al. 2015, 2018; Brisbin et al. 2015; Spilker et al. 2016; Zanella et al. 2018; Cooke

et al. 2018; Rybak et al. 2019; McKinney et al. 2020). At $z \approx 1-5$, the selected galaxies are mostly uncovered by sub-mm surveys, which are traditionally classified as ‘sub-millimetre-bright galaxies (SMGs¹)’. These are heavily dust-obscured systems having $L_{\text{IR}} \geq 10^{12} L_{\odot}$ (corresponding to $\text{SFR} \geq 100 M_{\odot} \text{yr}^{-1}$; Kennicutt 1998). In general, it is found that $[\text{C}_{\text{II}}]$ deficit persists at high L_{IR} at high redshifts, although the high- z populations appear to show larger scatter of $L_{[\text{C}_{\text{II}}]}/\text{SFR}$ at given L_{IR} than the local ones.

The advent of the Atacama Large Millimetre/submillimetre Array (ALMA) Telescope (e.g. Wootten & Thompson 2009) has triggered particular interest in searching for $[\text{C}_{\text{II}}]$ emitters at $z \geq 5$, and accumulating efforts have been made to constrain the $L_{[\text{C}_{\text{II}}]}$ -SFR relation of galaxies at this epoch (e.g. Ouchi et al. 2013; Ota et al. 2014; Maiolino et al. 2015; Capak et al. 2015; Willott et al. 2015b; Pentericci et al. 2016; Matthee et al. 2017, 2019; Carniani et al. 2018a; Smit et al. 2018; Schaerer et al. 2020; Fujimoto et al. 2021; Ferrara et al. 2022; Schouws et al. 2023). The ALMA observational programs are often designed to target the Lyman- α emitters (LAEs), Lyman-break galaxies (LBGs) and the quasar host galaxies (hereafter quasar hosts for simplicity) having pre-determined redshift (Hodge & da Cunha 2020). Though the earliest attempts targeting the bright LAEs were mostly unsuccessful (e.g. Maiolino et al. 2005; Ouchi et al. 2013; Ota et al. 2014; Inoue et al. 2016), follow-up programs targeting the LBGs and quasar hosts generally have had much higher success rate of $[\text{C}_{\text{II}}]$ line detection. Overall, there have been > 200 galaxies at $z \geq 5$ that have confirmed detection of $[\text{C}_{\text{II}}]$ line to date. While the quasar hosts are typically very luminous and have substantial SFR (e.g. Bañados et al. 2016; Decarli et al. 2018; Venemans et al. 2020), many of the selected LBGs/LAEs at $z \geq 5$ are normal SFGs having moderate SFR ($\approx 10 M_{\odot} \text{yr}^{-1}$). In particular, the ALMA Large Program to Investigate $[\text{C}_{\text{II}}]$ at Early times (ALPINE) survey (Le Fèvre et al. 2020; Béthermin et al. 2020; Faisst et al. 2020a) in Cycle-5, targeting a sample of 118 star-forming galaxies at $z \approx 5-6$, has contributed more than a third ($\sim 75/200$) of the total number of successful detections at $z \geq 5$ (Schaerer et al. 2020). More recently, the ALMA Reionization Era Bright Emission Line Survey (REBELS; Bouwens et al. 2022) in Cycle-7 has targeted a sample of 40 UV-bright, star-forming galaxies at $z \approx 7$ and confirmed $[\text{C}_{\text{II}}]$ line detection for 18 galaxies in their sample (Ferrara et al. 2022).

Observations have drawn divergent conclusions on the $L_{[\text{C}_{\text{II}}]}$ -SFR relation at $z \geq 5$. While some have argued a clear $[\text{C}_{\text{II}}]$ deficit of galaxies at $z \geq 5$ with respect to the local normal SFGs (e.g. Ouchi et al. 2013; Ota et al. 2014; Maiolino et al. 2015; Inoue et al. 2016; Knudsen et al. 2016; Pentericci et al. 2016; Bradač et al. 2017; Ferrara et al. 2019; Laporte et al. 2019; Carniani et al. 2020; Fujimoto et al. 2022; Fudamoto et al. 2023b), others have argued that they follow the same linear scaling relation (e.g. Matthee et al. 2017; Carniani et al. 2018a; Schaerer et al. 2020; Fujimoto et al. 2021; Ferrara et al. 2022; Schouws et al. 2023; Fudamoto et al. 2023a; Fujimoto et al. 2023). It should be noted, however, that the SFR estimates at such high redshifts can be highly uncertain. Galaxies at $z \geq 5$ typically have very few reliable photometric data points in the dust thermal continuum that are measured with ALMA (at band 6 or 7). A number of recent studies, both observational (Capak et al. 2015; Bouwens et al. 2016; Casey et al. 2018a; Faisst et al. 2020b) and theoretical (Liang et al. 2019, 2021; Ma et al. 2019; Sommovigo et al. 2020, 2021), have pointed out that based on the ALMA broad-band flux(es)

¹ In the literature, ‘SMGs’ typically refer to the galaxies detectable by single-dish sub-mm telescopes, of which the observed sub-mm flux density is above $\sim 1 \text{ mJy}$ (Casey et al. 2014; Hodge & da Cunha 2020).

alone, L_{IR} (and hence the obscured SFR) of galaxies at $z \gtrsim 5$ is likely to be poorly constrained due to the large variation in the shape of the spectral energy distribution (SED) of their dust emission. The reported (in)consistencies of the $L_{[\text{CII}]}$ -SFR relation at $z \gtrsim 5$ with the local SFGs by the observations therefore need to be more carefully assessed.

Much effort has been made to model $[\text{CII}]$ emission of galaxies and explain the origins of the observed $[\text{CII}]$ deficit over the last two decades. A broad variety of different methods are used by different studies, including pure analytic approaches (e.g. Muñoz & Oh 2016; Ferrara et al. 2019), numerical models of idealized gas clouds (e.g. Abel et al. 2009; Narayanan & Krumholz 2017), semi-analytic galaxy models (SAMs, e.g. Popping et al. 2014, 2016, 2019; Lagache et al. 2018; Yang et al. 2021, 2022) and hydrodynamic galaxy simulations (e.g. Vallini et al. 2013, 2015; Olsen et al. 2015, 2017; Pallottini et al. 2017, 2019; Katz et al. 2019; Leung et al. 2020; Lupi et al. 2020; Lupi & Bovino 2020; Kannan et al. 2022b; Richings et al. 2022; Bisbas et al. 2022). A pure analytic approach and/or a simplified cloud model can capture the key physical mechanisms that determine $L_{[\text{CII}]}$ of galaxies and provide useful insights at low computational cost, but does not provide the necessary galaxy statistics. SAMs can produce statistically significant galaxy samples probing a very wide dynamic range (in stellar mass, SFR, redshift and etc.) and are computationally efficient (Somerville & Davé 2015), but they do not provide any information of structures on the sub-galactic scales. Hydrodynamic simulations, in contrast, can calculate the detailed sub-galactic structures and thus provide more accurate prediction for the $[\text{CII}]$ emission properties of galaxies, at the cost of more computational expense.

Different explanations for the $[\text{CII}]$ deficit in the high L_{IR} regime have been proposed by the theory groups (see also e.g. Casey et al. 2014; Narayanan & Krumholz 2017, for a summary). For instance, some studies argue that the deficit is due to a strong UV radiative intensity (G) in the IR luminous galaxies (e.g. Malhotra et al. 1997, 2001; Luhman et al. 1998; Genzel & Cesarsky 2000; Helou et al. 2001; Luhman et al. 2003; Abel et al. 2009; Stacey et al. 2010; Graciá-Carpio et al. 2011; Lagache et al. 2018). This can have two important effects on the thermal balance of $[\text{CII}]$ -emitting gas. First of all, a high G leads to large positive grain charges, thereby reducing the kinetic energy of the ejected photo-electrons and hence the rate of PE heating (\dot{E}_{PE}) of gas (Tielens & Hollenbach 1985; Kaufman et al. 1999). As a result, $[\text{CII}]$ cooling rate drops. Besides, H^+ regions in those galaxies may become ‘dust bounded’ rather than ‘ionization bounded’ (e.g. Bottorff et al. 1998; Abel et al. 2009; see also Ferrara et al. 2019). In this scenario, most of the UV radiation from young stars is absorbed by dust in the H^+ regions, leading to both an excess of IR emission in the H^+ regions and a reduced \dot{E}_{PE} (and hence $L_{[\text{CII}]}$) in gas outside the H^+ regions due to a starvation of UV photons there.

Alternatively, Narayanan & Krumholz (2017) suggest that a high gas density can lead to a $[\text{CII}]$ deficit of galaxy in addition to having a high G . Using a stratified gas cloud model, the authors demonstrate that with increasing gas density, a larger fraction of carbon in gas turns into neutral (i.e. in CO and C_1) and $L_{[\text{CII}]}$ decreases due to a reduced mass fraction of $[\text{CII}]$ -emitting gas.

Apart from these studies, Muñoz & Oh (2016) posit an analytic model where $[\text{CII}]$ deficit is due to thermal saturation of the upper fine

structure transition state ($^2P_{3/2}$) of C^+ ions². At above 91.8 K (note: $T_* = 91.8$ K is the equivalent temperature of the $[\text{CII}]$ transition), $L_{[\text{CII}]}$ does not increase much with gas kinetic temperature and this has been suggested to be the reason for $L_{[\text{CII}]}$ not increasing much with SFR at high L_{IR} (\sim SFR) (see also discussions in the observational studies by Díaz-Santos et al. 2017; Croxall et al. 2017). Note, however, that the Muñoz & Oh (2016) model assumes that the bulk of the $[\text{CII}]$ emission of galaxies originates from the gas having density in excess of the critical density for the $[\text{CII}]$ transition (Goldsmith et al. 2012).

With the recent success of the ALMA programs in searching for $[\text{CII}]$ -emitters, there has been an increasing amount of effort to predict $[\text{CII}]$ emission properties of galaxies at $z \gtrsim 5$ by coupling cosmological hydrodynamic simulations or SAMs with photo-ionization codes (e.g. CLOUDY, Ferland et al. 1998, 2013; DESPOTIC, Krumholz 2014; RADMC-3D, Dullemond et al. 2012). The predicted $L_{[\text{CII}]}$ -SFR relation for galaxies, however, shows non-trivial discrepancy between different groups in both normalization and slope (e.g. Katz et al. 2019; Leung et al. 2020), which can be ascribed to the differences in the simulation methodology and $[\text{CII}]$ modelling techniques adopted by the different groups. Despite the discrepancy, many have predicted a $[\text{CII}]$ deficit of galaxies at $z \gtrsim 5$ with respect to the local normal SFGs. For instance, Lagache et al. (2018) couple a sample of ~ 20 K SAM galaxies at $4 \leq z \leq 8$ with CLOUDY and report a $[\text{CII}]$ deficit of > 0.5 dex and a trend of decreasing normalization of the relation with redshift. Olsen et al. (2017) post-process 30 star-forming galaxies at $z = 6$ extracted from the MUFASA ‘zoom-in’ simulations (Davé et al. 2016) using CLOUDY and predict a $[\text{CII}]$ deficit of about one dex. A similarly strong $[\text{CII}]$ deficit is reported by Pallottini et al. (2017, 2019) using the SERRA ‘zoom-in’ simulations that include more sophisticated chemical networks. More recently, Kannan et al. (2022b) predict an even more prominent $[\text{CII}]$ deficit at $z \geq 5$ than the above-mentioned earlier studies, especially at low SFR, using a galaxy sample produced by the THESAN ‘zoom-in’ suite (Kannan et al. 2022a; Garaldi et al. 2022), which includes the ILLUSTRIS-TNG galaxy formation model (Pillepich et al. 2018a,b).

It has been generally thought that gas metallicity (Z_{gas}) is the key factor in determining the $[\text{CII}]$ luminosity of the early galaxies (e.g. Vallini et al. 2015; Olsen et al. 2017; Ferrara et al. 2019; Heintz et al. 2021, 2022) since $[\text{CII}]$ emissivity is linearly scaled with Z_{gas} . The early work by Vallini et al. (2015) shows that the $L_{[\text{CII}]}$ -SFR relation of EoR galaxies is sensitive to Z_{gas} , and the significant $[\text{CII}]$ deficit found with the LAEs at $z \approx 5 - 7$, such as Himiko (Ouchi et al. 2013; Ota et al. 2014) and IOK-1 (Ota et al. 2014), can be well accounted for by assigning a very low gas metallicity ($Z_{\text{gas}} < 0.05 Z_{\odot}$) to the simulated galaxy in an ad hoc manner. The $[\text{CII}]$ deficit of galaxies at $z \gtrsim 5$ commonly found in the recent simulations, as mentioned above, is likely due to the much lower Z_{gas} of the early galaxies than the $z = 0$ ones predicted by these simulations. Observationally, however, direct measurement of Z_{gas} at $z \gtrsim 5$ is still very challenging, though some preliminary attempts have been made recently (e.g. Rigopoulou et al. 2018; Schaerer et al. 2022; Curti et al. 2023; Heintz et al. 2023a,b; Rhoads et al. 2023; Trump et al. 2023).

A few recent studies have predicted $[\text{CII}]$ emission of galaxies at lower redshifts using simulations. For instance, Popping et al. (2019) and Yang et al. (2021) predict the $L_{[\text{CII}]}$ -SFR relation for the catalog derived from the ‘Santa Cruz’ semi-analytic models (Somerville &

² Throughout this paper, we use ‘ $[\text{CII}]$ ’ when referring to the observable emission line, and ‘ C^+ ’ when discussing ionized carbon under the context of chemical abundances of gas.

Primack 1999; Somerville et al. 2015) using DESPOTIC. Their result is in good agreement with the observational data at $z \approx 2$, except that at high SFR (*i.e.* $\text{SFR} \gtrsim 10 M_{\odot} \text{yr}^{-1}$), they produce a noticeably weaker $[\text{CII}]$ deficit than is observed. More recently, Richings et al. (2022) ran a set of hydrodynamic simulations of isolated (dwarf and Milky Way-mass) galaxies implemented with the CHIMES non-equilibrium chemistry module (Richings et al. 2014a,b) (including a dust-depletion model) and predict the $[\text{CII}]$ emission of their galaxy sample using RADMC-3D. Despite having a small sample size, the predicted $L_{[\text{CII}]}$ of their galaxies appears to be in agreement with the observational result of local galaxies (*e.g.* De Looze et al. 2011, 2014; Herrera-Camus et al. 2015) at similar SFR (see also another recent work by Bisbas et al. 2022 using isolated dwarf simulations).

Apart from these studies, there has been limited effort to predict the $L_{[\text{CII}]}$ -SFR relation of galaxies at $z = 0 - 5$ using statistically representative galaxy samples and compare the result to the fruitful observational data in this regime. In particular, the origin of the $[\text{CII}]$ deficit of the IR-luminous galaxies has not yet been studied in detail using cosmological hydrodynamic simulations. This is largely because producing a statistically representative sample in this regime with well-resolved ISM is computationally demanding, which is possible only for a few large simulation consortiums. It is, however, of critical importance that a robust $[\text{CII}]$ model should be able to simultaneously reproduce the data of different galaxy populations over the entire SFR and redshift ranges.

In this study, we conduct a comprehensive analysis of the galaxy $L_{[\text{CII}]}$ -SFR relation using a simulated sample spanning an unprecedentedly broad redshift range of $z = 0 - 8$ extracted from the MASSIVEFIRE (Feldmann et al. 2016, 2017; Anglés-Alcázar et al. 2017) and FIREBOX (Feldmann et al. 2023) cosmological hydrodynamic simulations from the *Feedback in Realistic Environments* (FIRE) project³ (Hopkins et al. 2014, 2018, 2023). The sample covers a very broad range of galaxy stellar mass and SFR, allowing us to make direct comparison with the observational data in different regimes. In particular, the sample includes local normal SFGs (having $\text{SFR} \approx 0.1 - 10 M_{\odot} \text{yr}^{-1}$) that can be compared with the observations where a linear $L_{[\text{CII}]}$ -SFR correlation has been found by the observations. It also includes IR-luminous ($L_{\text{IR}} > 10^{11} L_{\odot}$) galaxies at $z = 0 - 5$ that are candidates for (U)LIRGs and SMGs, where observations have shown to have $[\text{CII}]$ deficit. Moreover, the sample includes early galaxies at above $z = 5$ spanning a broad SFR range. Many of these galaxies have similar mass and SFR to the samples of the ALPINE and REBELS projects and therefore can be used to provide useful interpretations for a variety of their recent observational results (*e.g.* Fujimoto et al. 2020; Ginolfi et al. 2020; Schaerer et al. 2020; Fudamoto et al. 2021, 2022; Ferrara et al. 2022; Sommovigo et al. 2022).

The main goal of this work is to predict the $L_{[\text{CII}]}$ -SFR relation for the FIRE galaxy sample (spanning $z = 0 - 8$ and $\text{SFR} \approx 0.1 - 10^3 M_{\odot} \text{yr}^{-1}$) and to understand what physical parameters of galaxies determine their overall $L_{[\text{CII}]}$ -to-SFR ratio. This will then help us find the origin of the observed $[\text{CII}]$ deficit of galaxies at both high L_{IR} and high redshifts.

Note that the results from this work will be useful for interpreting the data of several upcoming $[\text{CII}]$ line intensity mapping (LIM) experiments (see *e.g.* Kovetz et al. 2017, 2019; Bernal & Kovetz 2022; Horlaville et al. 2023, and references therein), such as TIME⁴ (Sun

et al. 2021), CCAT-PRIME⁵ (CCAT-Prime collaboration et al. 2021), CONCERTO⁶ (CONCERTO Collaboration et al. 2020; Gkogkou et al. 2023) and EXCLAIM (Switzer et al. 2021; Pullen et al. 2023). The LIM experiments have been designed to measure the emission from spectral lines originating from galaxies at all luminosities, including the ones that cannot be resolved by the current surveys (*e.g.* with ALMA). The experiments that will target $[\text{CII}]$ emission, in particular, will be useful for constraining the cosmic star-formation history (see *e.g.* Gong et al. 2012; Silva et al. 2015; Serra et al. 2016; Fonseca et al. 2017; Padmanabhan 2019; Yue & Ferrara 2019; Chung et al. 2020; Padmanabhan et al. 2022; Karoumpis et al. 2022; Sun et al. 2023). It is, however, not yet certain whether the $[\text{CII}]$ line always acts as a reliable SFR tracer for galaxies of all types and at all redshifts.

This paper is structured as follows. We describe in Section 2 the simulation methodology and in Section 3, the method used to simulate $[\text{CII}]$ emission. In Section 4, we compare the predicted $L_{[\text{CII}]}$ -SFR relation of the FIRE galaxy sample with the observational data at different redshifts. In Section 5, we investigate the origin of the tight $L_{[\text{CII}]}$ -SFR linear scaling relation of normal SFGs at $z = 0$ and the causes of the $[\text{CII}]$ deficit of galaxies. We discuss our results in Section 6 and finally summarize and conclude this study in Section 7. Throughout this paper, we adopt the cosmological parameters of the Planck 2015 Cosmology (Planck Collaboration et al. 2016), specifically $\Omega_{\text{m}} = 0.309$, $\Omega_{\Lambda} = 0.691$, $\Omega_{\text{b}} = 0.049$, $\sigma_8 = 0.816$, and $H_0 = 67.74 \text{ km s}^{-1} \text{ Mpc}^{-1}$.

2 SIMULATION METHODOLOGY

In this section, we introduce the simulation suites (FIREBOX and MASSIVEFIRE) from which we extract the galaxy sample used for this study.

2.1 Simulation set-up and galaxy catalogue

We adopt a sample that spans the wide redshift range $z = 0 - 8$, stellar mass (M_*) range $M_* \approx 10^7 - 5 \times 10^{11} M_{\odot}$ and SFR range $\text{SFR} \approx 0.1 - 10^3 M_{\odot} \text{yr}^{-1}$. The sample consists primarily of galaxies at $z = 0 - 8$ produced by FIREBOX (Feldmann et al. 2023), the new-generation simulation suite of FIRE run with full cosmological volume boxes. It is supplemented by a number of high- z ($z = 1 - 8$) massive galaxies ($M_* \gtrsim 10^{10} M_{\odot}$) extracted from the ‘zoom-in’ suite, MASSIVEFIRE (Feldmann et al. 2016, 2017), rerun with FIRE-2 physics (Anglés-Alcázar et al. 2017; Çatmabacak et al. 2022; Bassini et al. 2023). Many of the MASSIVEFIRE galaxies have the L_{IR} close to that of the SMGs (Liang et al. 2018; Cochrane et al. 2019) that are used by the observational studies on the $L_{[\text{CII}]}$ -SFR relation at high redshifts. All simulations used for this study are run with the same FIRE-2 physics and numerics (Hopkins et al. 2018).

FIREBOX simulations

FIREBOX (Feldmann et al. 2023) is a new-generation simulation suite using FIRE physics. Different from all previous simulations of FIRE, FIREBOX simulates full cosmological volumes instead of using ‘zoom-in’ set-up to study galaxy evolution. FIREBOX simulations are run in cubic boxes with periodic boundary conditions, and with initial

³ FIRE project website: <http://fire.northwestern.edu>

⁴ <https://cosmology.caltech.edu/projects/TIME>

⁵ <http://www.ccatobservatory.org>

⁶ <https://www.apex-telescope.org/ns/concerto/>

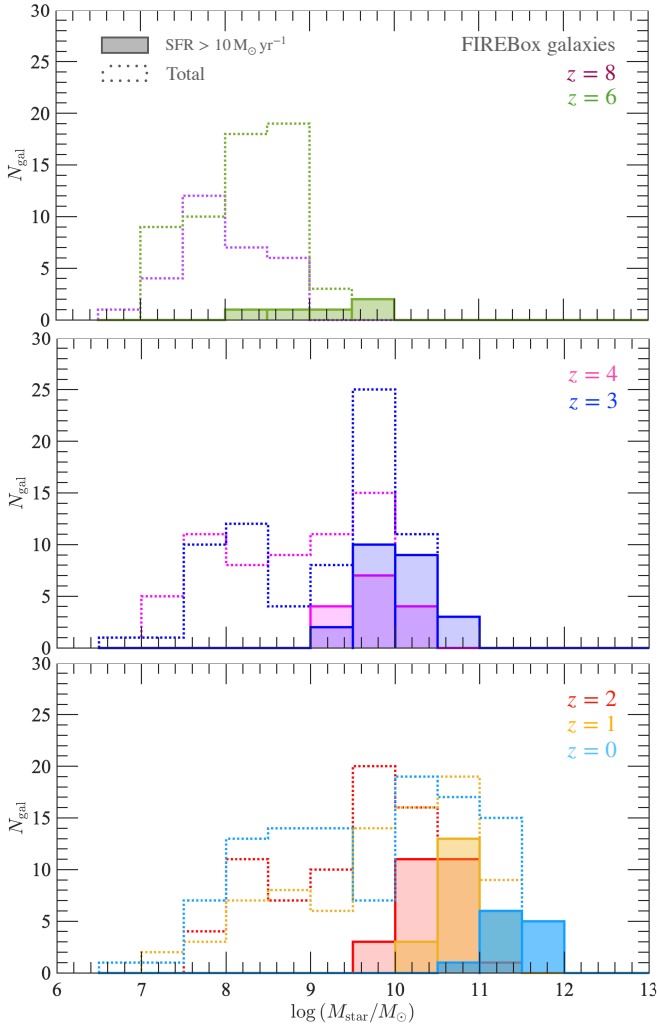


Figure 1. Histograms of the stellar mass distribution of the FIREbox sample at different redshifts. Violet, green, magenta, blue, red, yellow and cyan histograms correspond to $z = 8$, $z = 6$, $z = 4$, $z = 3$, $z = 2$, $z = 1$ and $z = 0$, respectively. For each redshift, the unfilled histograms indicate the result of the entire galaxy sample, whereas the filled histograms indicate specifically the result of the galaxies having $\text{SFR} \geq 10 M_{\odot} \text{ yr}^{-1}$ (corresponding to $L_{\text{IR}} \geq 10^{11} L_{\odot}$ based on the Kennicutt 1998 relation. Note: [C_{II}] deficit is observed at $L_{\text{IR}} \geq 10^{11} L_{\odot}$). For clarity of presentation, we separately show the result of the 7 snapshots in 3 separate panels (*top* panel for $z = 8$ and $z = 6$, *middle* panel for $z = 3$ and $z = 4$ and *bottom* panel for $z = 0$, $z = 1$ and $z = 2$).

conditions at redshift $z = 120$ generated using the MUSIC (Multi-Scale Initial Conditions) code (Hahn & Abel 2011). The simulations use the Planck 2015 Cosmology (Planck Collaboration et al. 2016).

All FIREbox simulations use the same initial conditions and cosmology but differ in numerical resolution. For this study, we extract galaxies from the fiducial FIREbox hydrodynamic simulation, which is run with a box length of $15 h^{-1} \text{ cMpc}$ and with the following number of dark matter (DM) and baryonic particles: $N_{\text{DM}} = 1024^3$ and $N_{\text{b}} = 1024^3$. The mass resolution of DM and baryon particles are $m_{\text{DM}} = 3.3 \times 10^5$ and $m_{\text{b}} = 6.3 \times 10^4 M_{\odot}$. The gravitational softening lengths are kept fixed in proper (comoving) coordinates at $z \leq 9$ ($z \geq 9$) and are set to $h_{\text{DM}} = 80 \text{ pc}$ for DM particles and $h_{\text{b}} = 12 \text{ pc}$ for star particles. The softening length for gas particles (h_{gas}) is fully adaptive and is set equal to their kernel smoothing

length down to a minimum of 1.5 proper pc, which is reached in the densest parts of the ISM. FIREbox is evolved down to $z = 0$.

We identify galaxies in different snapshots of the FIREbox simulation using the AMIGA HALO FINDER⁷ (AHF; Gill et al. 2004; Knollmann & Knebe 2009). We use the galaxies extracted from 7 snapshots corresponding to redshift $z = 0, 1, 2, 3, 4, 6$ and 8 . For each snapshot, we include the central galaxy of the 30 most massive halos identified by AHF. To enlarge our sample, we also include the central galaxy of a number of additional, randomly chosen halos having $\log(M_{\text{vir}}/M_{\odot}) > 10$. We show in Fig. 1 the histograms of the M_{star} distribution of the selected FIREbox galaxies at different redshifts.

The number of galaxies selected at $z = 0, 1, 2, 3, 4, 6$ and 8 are 113, 84, 80, 75, 64, 61 and 30, respectively. As is shown in Fig. 1, all but a few selected galaxies have stellar mass greater than $10^7 M_{\odot}$ (corresponding to ~ 160 times of the mass resolution). The most massive galaxy of the FIREbox sample has $M_{\text{star}} = 4.8 \times 10^{11} M_{\odot}$ (at $z = 0$).

In the same figure, we also show the M_{star} distribution of the galaxies having $\text{SFR} \geq 10 M_{\odot} \text{ yr}^{-1}$ (filled histograms). These galaxies have $L_{\text{IR}} \geq 10^{11} L_{\odot}$, the regime where a [C_{II}] deficit is observed (see Section 3). They apparently are more massive than the galaxies having $\text{SFR} < 10 M_{\odot} \text{ yr}^{-1}$. In our catalogue, we find most galaxies with $\text{SFR} \geq 10 M_{\odot} \text{ yr}^{-1}$ at $z = 2$ (red histogram, $N = 29$) and $z = 3$ (blue histogram, $N = 28$). These redshifts are at the ‘cosmic noon’, where massive galaxies start to form and they are more gas-rich and actively star-forming than galaxies at lower redshifts.

Since the FIREbox simulation is run with a volume of $(15 h^{-1} \text{ cMpc})^3$, it does not produce enough galaxies at high redshifts that are as massive and luminous as the galaxy samples selected by the observational studies. We therefore supplement our sample with a handful of more massive galaxies ($M_{\text{star}} \approx 10^9 - 5 \times 10^{11} M_{\odot}$) extracted from the MASSIVEFIRE ‘zoom-in’ simulations (see below).

MassiveFIRE simulations

MASSIVEFIRE (Feldmann et al. 2016, 2017) is a set of simulations of massive galaxies at high redshifts using the ‘zoom-in’ method. A number of low-resolution (LR) DM-only simulations were run with the initial conditions generated using the MUSIC code within periodic boxes. From the outputs of these LR DM-runs, we then select a number of model haloes to re-simulate at much higher resolution and with baryons included (HR runs). The selected haloes have a variety of masses, accretion history, and environmental over-densities.

For this study, we use the galaxies produced by 10 MASSIVEFIRE simulations, which are from the A (Anglés-Alcázar et al. 2017), D and E Series (Çatmabacak et al. 2022; Bassini et al. 2023). The A, D and E Series were run in the periodic boxes with size of $(100 h^{-1} \text{ Mpc})^3$, $(400 h^{-1} \text{ Mpc})^3$ and $(762 h^{-1} \text{ Mpc})^3$, respectively. The model haloes of the A Series are selected from the snapshot of $z_{\text{final}} = 1$, those of the D and E Series are selected from the snapshot of $z_{\text{final}} = 6$. All the HR runs were run down to z_{final} except D7, where the HR run is evolved to only $z = 7.2$. This is because part of the ISM in D7 became too compact so that the gas particles with the highest densities were evolved at extremely small time-steps and it became infeasible to run the simulation down to the target redshift.

Initial conditions for the HR runs are set up using a convex hull surrounding all particles within $3R_{\text{vir}}$ at z_{final} of the chosen halo defining the Lagrangian HR region following the method of Hahn & Abel (2011). The mass resolutions and force softening lengths of the HR runs are similar to those of the FIREbox simulation. Specifically,

⁷ Code available at: popia.ft.uam.es/AHF/Download.html

Table 1. List of MASSIVEFIRE simulations used for this work.

Sim ID †	Box Size (h^{-1} Mpc)	z_{final}	$M_{\text{vir}} \ddagger$ ($10^{12} M_{\odot}$)	M_* (M_{\odot})					
				$z = 1$	$z = 2$	$z = 3$	$z = 4$	$z = 6$	$z = 8$
A1	100	1	2.4	5.4×10^{11}	5.1×10^{10}	9.6×10^9	1.2×10^9	/	/
A2	100	1	3.0	4.1×10^{11}	2.9×10^{11}	1.3×10^{11}	2.7×10^{10}	/	/
A4	100	1	2.9	2.3×10^{11}	1.3×10^{11}	2.2×10^{10}	6.5×10^9	/	/
A8	100	1	3.6	2.8×10^{11}	1.8×10^{11}	9.8×10^{10}	5.1×10^{10}	/	/
D3	400	6	4.5	/	/	/	/	3.9×10^{11}	7.0×10^{10}
D7§	400	6	2.5	/	/	/	/	/	5.8×10^{10}
D9	400	6	1.0	/	/	/	/	3.9×10^{10}	1.3×10^9
E1	762	6	6.8	/	/	/	/	1.6×10^{10}	3.2×10^9
E2	762	6	6.5	/	/	/	/	7.2×10^9	5.3×10^9
E3	762	6	6.1	/	/	/	/	8.6×10^9	2.7×10^9

† The A (D and E) Series of MASSIVEFIRE were published in [Anglés-Alcázar et al. \(2017\)](#) ([Çatmabacak et al. 2022](#)) for the first time.

‡ Virial mass at z_{final} .

§ The HR simulation of D7 has been run only down to $z = 7.2$.

m_{DM} and m_{b} are set to $1.9 \times 10^5 M_{\odot}$, $3.6 \times 10^4 M_{\odot}$, respectively. Both h_{DM} and h_* are fixed in proper (comoving) coordinates at $z \leq 9$ ($z \geq 9$) and are set equal to 57 pc and 7 pc, respectively. h_{gas} is set equal to the smoothing length of the gas particles down to a minimum of 0.7 proper pc.

We include the central galaxy of the chosen haloes at z_{final} except for that of the D7 run. In addition, we also include the most massive progenitors (MMPs) of the central galaxies at higher redshifts. Specifically, for the 4 A Series runs, we include the MMPs at $z = 2$, $z = 3$ and $z = 4$, while for the D and E Series, we include the MMPs at $z = 8$. The galaxies are identified in the simulation snapshots using AHF ([Gill et al. 2004](#); [Knollmann & Knebe 2009](#)). In Table 1, we summarize the information⁸ of the 10 MASSIVEFIRE simulations used for this study.

Both the MASSIVEFIRE and FIREBOX simulations used in this work are run using the N-body+hydrodynamics code GIZMO (FIRE-2 version) in the Meshless-Finite-Mass (MFM) mode ([Hopkins et al. 2018](#)). The simulations incorporate various gas cooling processes (free-free, photoionization/recombination, Compton, photoelectric, metal-line, molecular and fine structure processes) and a uniform UV background following the FG09 prescription ([Faucher-Giguère et al. 2009](#)). Star formation occurs in dense, self-gravitating and self-shielding molecular gas based on a sink-particle prescription. The simulations explicitly incorporate several different stellar feedback channels (but not feedback from supermassive black holes) including 1) local and long-range momentum flux from radiative pressure, 2) energy, momentum, mass and metal injection from supernovae (Types Ia and II), 3) stellar mass loss (both OB and AGB stars) and 4) photo-ionization and photo-electric heating processes. We refer the reader to [Hopkins et al. \(2014, 2018\)](#) for details of the star formation and feedback prescriptions of FIRE.

FIRE has demonstrated success at reproducing a variety of key galaxy properties that are relevant to this work, such as the stellar-to-halo mass relation ([Hopkins et al. 2014](#); [Feldmann et al. 2017](#)), the specific SFR (sSFR) of galaxies at the cosmic noon ($z \sim 2$) ([Hopkins et al. 2014](#); [Feldmann et al. 2016](#); [Sparre et al. 2017](#); [Feldmann et al. 2023](#)), the galaxy molecular (atomic) hydrogen gas mass and

stellar mass relations at $z = 0$ ([Feldmann et al. 2023](#)), the gas-phase and stellar mass-metallicity relation at $z = 0 - 2$ ([Ma et al. 2016](#); [Feldmann et al. 2023](#)), the observational effective dust temperatures at $z = 2 - 4$ ([Liang et al. 2019](#)) as well as the UV luminosity functions and UV-based cosmic star formation rate density (CSFRD) at $z > 5$ ([Ma et al. 2019](#)).

3 SIMULATING OBSERVATIONAL PROPERTIES

In this section, we describe the method used to predict the observational properties for the FIRE galaxy sample, which we compare to the observational data. In Section 3.1, we describe our $[\text{C II}]$ emission model. In Section 3.2, we describe the prescription for the dust RT modelling of the FIRE galaxies using SKIRT code, based on which we derive the multi-wavelength SED and the distribution of the interstellar radiation field (ISRF) for the galaxies. The ISRF distribution is essential for predicting the $[\text{C II}]$ emission properties of the galaxies.

3.1 Predicting $[\text{C II}]$ emission using CLOUDY

We predict the $[\text{C II}]$ line luminosity for the FIRE sample using the spectral synthesis code CLOUDY version 17.01 ([Ferland et al. 2017](#)). CLOUDY is a plasma simulation code designed to simulate the ionization, level populations, molecular state and thermal state of gas over a wide range of density and temperature in different astrophysical environments (*e.g.* black hole accretion disks, PDRs, molecular clouds, etc). It solves for the ionization structure for all stages of ionization for the lightest 30 elements ([Abel et al. 2008](#)).

We treat each gas particle of the galaxies as an idealized spherical uniform ‘gas cloud’. The $[\text{C II}]$ luminosity of each ‘cloud’ is calculated based on its physical conditions, including ‘cloud’ (or gas particle) mass (M_{cl}), gas density⁹ (n_{H}), gas metallicity (Z_{gas}), gas turbulent velocity dispersion (σ) and local UV ISRF strength (G^{10}). M_{cl} , n_{H} , Z_{gas} of each ‘cloud’ are known directly from the FIRE simulations. σ is the mass-weighted standard deviation of the

⁹ In this paper, ‘gas density’ consistently refers to the number density of hydrogen nuclei (n_{H}) in the gas, rather than mass density. CLOUDY takes n_{H} as an input.

¹⁰ Conventionally, G is used to denote the mean ISRF in the Habing band (6.0 – 13.6 eV). It is indicated in units of $G_0 = 1.6 \times 10^{-3} \text{ erg s}^{-1} \text{ cm}^{-2}$, the observed value in the solar neighbourhood ([Habing 1968](#)).

⁸ Physical properties, including *e.g.* M_* , SFR, L_{IR} and $L_{[\text{C II}]}$, of the FIRE galaxies reported in this paper are estimated using a radial kernel of $0.1R_{\text{vir}}$ around the DM halo centre, *i.e.* the maximum density centre provided by AHF.

velocities in gas at the location of the ‘cloud’, which is calculated in post-processing. Finally, G at the location of each ‘cloud’ in the galaxy is calculated using the dust RT code SKIRT (Baes et al. 2011; Baes & Camps 2015; Camps & Baes 2015) in post-processing (see Section 3.2 for the details).

We calculate the [C_{II}] luminosity for each ‘cloud’ ($L_{[\text{C}_{\text{II}}], \text{cl}}$) by integrating the [C_{II}] line cooling rate, $\Lambda_{[\text{C}_{\text{II}}]}$ (erg s⁻¹ cm⁻³; see Appendix A for its analytic expression), obtained from the output of the CLOUDY simulations, over the volume of the ‘cloud’¹¹:

$$L_{[\text{C}_{\text{II}}], \text{cl}} = 4\pi \int_0^{R_{\text{cl}}} \Lambda_{[\text{C}_{\text{II}}]}(x) x^2 dx, \quad (1)$$

where R_{cl} indicates the ‘radius’ of the ‘cloud’, approximated by a Sobolev-like length scale (L_{sob}) defined using local density gradients (Sobolev 1957; Gnedin et al. 2009), *i.e.*

$$R_{\text{cl}} \sim L_{\text{sob}} \equiv \frac{\rho}{2|\nabla\rho|}. \quad (2)$$

This length scale was introduced by Gnedin & Kravtsov (2011) to derive the *effective* column densities of the ‘clouds’ for determining their H₂ abundances, knowing that small-scale star-forming molecular clumps are typically unresolved by galaxy-scale simulations. We then calculate the [C_{II}] luminosity of the galaxy ($L_{[\text{C}_{\text{II}}]}$) by summing over $L_{[\text{C}_{\text{II}}], \text{cl}}$ of all gas ‘clouds’ calculated using equation (1). We treat the [C_{II}] emission of our galaxy sample as being optically thin.

In practice, to run CLOUDY simulations for every gas particle for the whole FIRE sample (> 400 galaxies in total) is computationally formidable: a CLOUDY simulation is typically completed (*i.e.* when iterative convergence is reached) in 0.1 – 0.5 CPU hour, depending on the gas column density, and hence to analyze one single galaxy snapshot that contains ~ 1 million gas particles would cost 100 – 500 K CPU hours in total. We therefore use a lookup-table method similar to the previous studies (*e.g.* Vallini et al. 2015, 2018, 2021; Katz et al. 2017, 2019; Olsen et al. 2017; Lagache et al. 2018; Li et al. 2018; Pallottini et al. 2019; Keating et al. 2020; Leung et al. 2020; Lupi et al. 2020; Yang et al. 2021; Lupi & Bovino 2020). Specifically, for each of the 7 snapshots, we build a grid of CLOUDY models that covers a gas density range $-1 < \log(n_{\text{H}}/\text{cm}^{-3}) < 5$, a gas metallicity range $-2 < \log(Z_{\text{gas}}/Z_{\odot}) < 0.8$, a turbulent velocity dispersion range $0 < \log(\sigma/\text{km s}^{-1}) < 2.4$ and a UV ISRF range $-1 < \log(G/G_{\odot}) < 4$. The grid spacing is set 0.5 dex for n_{H} and G , and 0.4 dex for Z_{gas} and σ . In total, the default look-up table that we use for calculating the [C_{II}] luminosity of our galaxy sample consists of 8,008 ($13 \times 8 \times 7 \times 11$) models for each redshift. We include the CMB background in the CLOUDY simulations for each redshift and the predicted [C_{II}] luminosity is corrected for the CMB attenuation effect (da Cunha et al. 2013). Cosmic-ray (CR) hydrogen ionization rate in these models is fixed to the fiducial value of $2 \times 10^{-16} \text{ s}^{-1}$, the observed value in the Milky Way (Indriolo et al. 2007; Indriolo & McCall 2012; Neufeld & Wolfire 2017). We assume a constant dust-to-metal mass ratio $\delta_{\text{dZr}} = 0.4$ (Dwek 1998; Draine et al. 2007; Watson 2011; Li et al. 2019) and adopt the default interstellar medium metal abundances ($\text{ABUNDANCE}_{\text{ISM}}$) stored in CLOUDY. The simulations are run till sufficiently large

distance from the surface of the slab is reached¹². Given n_{H} ¹³, Z_{gas} , G and N_{H} of each ‘cloud’, we interpolate [C_{II}] luminosity of the ‘cloud’ from the values found in the computed grid.

The treatment of the ISM as an aggregate of spherical gas ‘clouds’ in our model (and in the models of the previous theoretical studies mentioned above) is undoubtedly an idealization, since the ISM in real galaxies is a continuous medium with complex spatial configurations at and below the scale of these idealized ‘clouds’. Nevertheless, this approach allows us to crudely sample the surface densities of gas within the ISM, thereby enabling us to capture the essential physics responsible for the observed [C_{II}] deficit in galaxies.

CLOUDY simulation: an example

Here we show the conditions of a plane-parallel gas slab calculated by CLOUDY (Fig. 2). The slab has a uniform gas density $n_{\text{H}} = 50 \text{ cm}^{-3}$ and is illuminated by an external radiation field having $G = 200 G_{\odot}$. We present CLOUDY simulations for two different models, where Z_{gas} is set to Z_{\odot} and $1/10 Z_{\odot}$. We include the $z = 0$ CMB background and the CR hydrogen ionization rate is set to the default value. We show the results of the dust-rich and dust-poor models in the *left* and *right* panels of Fig. 2, respectively.

The slab is characterized by three distinct zones based on the ionization state of hydrogen gas. In the *upper* panels, we show the abundance profiles for ionized hydrogen (H⁺; dashed red line), atomic hydrogen (H_I; solid green line) and molecular hydrogen (H₂; dotted blue line), as well as the profile for gas temperature (solid black line). We can see that a H⁺ region (Zone I) is created near the surface of the slab by the ionizing photons ($E_{\gamma} > 13.6 \text{ eV}$) of the incident radiation field. Gas in this region is heated to high temperature ($T \approx 10^4 \text{ K}$). The slab then transits to a H_I-dominated region (Zone II) at a distance where ionizing radiation gets fully absorbed. The photons in the Lyman-Werner (LW) band ($11.2 < E_{\gamma} < 13.6 \text{ eV}$) dissociate H₂ in this region, while maintaining gas temperature at about 10^2 K . Finally, the slab transits to a H₂-dominated region (Zone III) at some larger distance, beyond which the LW radiation becomes sufficiently absorbed and the majority of hydrogen turns into H₂.

Like hydrogen, carbon has a very different ionization state in the three zones. This can be seen from the *middle* panels of Fig. 2, where we explicitly show the abundance profiles for atomic carbon (C_I; dotted blue line), singly ionized carbon (C⁺; solid green line) and doubly ionized carbon (C²⁺; dashed red line) for the two models. Carbon is mostly ionized in Zone I and II. Specifically, in Zone I, it gets excited to C⁺ level as well as higher ionization levels (*e.g.* C²⁺). In Zone II, on the contrary, carbon is singly ionized by LW photons but not excited to higher levels since ionizing photons are shielded

¹¹ Note that we do not derive $L_{[\text{C}_{\text{II}}], \text{cl}}$ using the ‘emergent intensity’ (I_{em} , with physical unit erg s⁻¹ cm⁻²) output by CLOUDY because I_{em} is calculated for a plane-parallel geometry instead of a spherical geometry. The conversion factor between the two geometries is not simply a constant but depends on the profile of [C_{II}] emissivity (Olsen et al. 2017, 2018).

¹² The THICKNESS of the slab is specified as a stopping criterion and is set at 400 pc in all our models, which is typically much larger than R_{cl} of the gas ‘clouds’ (defined using equation 2).

¹³ We calculate n_{H} for each individual ‘cloud’ using the values of M_{cl} (cloud mass) and R_{cl} as defined in equation (2): $n_{\text{H}} = (3M_{\text{cl}})/(4\pi R_{\text{cl}}^3 \mu_{\text{H}} m_{\text{H}})$, where m_{H} represents the proton mass, and μ_{H} represents the mean molecular weight of the gas.

from the region¹⁴. Finally, in Zone III, carbon turns into C_I and CO since the region is UV-dark¹⁵.

[C_{II}] emission originates mostly from the ionized (Zone I) and atomic hydrogen (Zone II) phases in our models. We show in the *middle* panels the profile for [C_{II}] cooling rate ($\text{erg s}^{-1} \text{cm}^{-3}$), $\Lambda_{[\text{C}_{\text{II}}]}$, for the two models (solid magenta line). It is clear that $\Lambda_{[\text{C}_{\text{II}}]}$ drops sharply in Zone III, which is due to the low abundance of C⁺ ions (solid green line) in this region (note: most carbon is in neutral state in Zone III). For the chosen models, $\Lambda_{[\text{C}_{\text{II}}]}$ appears to be similar in the ionized and atomic hydrogen phases, varying by less than a factor of few. Comparing the metal-rich (*left* panel) and metal-poor (*right* panel) models, it can be seen that $\Lambda_{[\text{C}_{\text{II}}]}$ of the metal-rich model is about a factor of ten higher. This is due to the fact that $\Lambda_{[\text{C}_{\text{II}}]}$ is linearly scaled to Z_{gas} and Z_{gas} of the metal-rich model is set as ten times that of the metal-poor model.

Using the $\Lambda_{[\text{C}_{\text{II}}]}$ profile output by CLOUDY, we subsequently derive the [C_{II}] luminosity profile (cumulative [C_{II}] luminosity as a function of column depth from the surface) for a uniform spherical cloud having $n_{\text{H}} = 50 \text{ cm}^{-3}$ (same as the gas slab) and $M_{\text{cl}} = 10^5 M_{\odot}$ that is irradiated by an external field having $G = 200 G_0$ (same as the gas slab) following equation (1). We calculate the result for the metal-rich ($Z_{\text{gas}} = Z_{\odot}$) and metal-poor ($Z_{\text{gas}} = 0.1 Z_{\odot}$) models, which are shown in the *lower left* and *lower right* panels of the figure, respectively. It can be seen that about 30% (10%) of the total [C_{II}] luminosity of the cloud is produced by the H⁺ region for the metal-rich (poor) model, while the remainder originates almost totally from the H_I region. The H₂ region contributes very limited fraction of the [C_{II}] luminosity. Note that the $\Lambda_{[\text{C}_{\text{II}}]}$ profile, the size of the different zones, and their relatively contribution to the total [C_{II}] luminosity of the cloud depends on G , n_{H} and Z_{gas} (see Section 5.1 for a detailed discussion).

One major difference between the two models (metal-rich vs. metal-poor) is whether or not the gas cloud has an H₂ region in the core, as can be seen from the *bottom* panels. For the metal-poor model (*bottom right* panel), because dust column density is small, LW photons are able to penetrate the entire cloud, making it H₂-free. The metal-rich model (*bottom left* panel), in contrast, has an H₂ core owing to the high dust column density, which accounts for roughly half of M_{cl} . The two cloud models correspond to the two distinct regimes where $L_{[\text{C}_{\text{II}}], \text{cl}}$ has different scaling with Z_{gas} . When the cloud has no H₂ core, $L_{[\text{C}_{\text{II}}], \text{cl}}$ scales linearly with Z_{gas} . As Z_{gas} (and hence the dust-to-gas mass ratio, δ_{dgr}) increases, the depth of Zone

I+Zone II decreases (Ferrara et al. 2019). When Z_{gas} is high enough that H₂ becomes abundant (*i.e.*, Zone III forms) in the core, $L_{[\text{C}_{\text{II}}], \text{cl}}$ saturates and no longer depends sensitively on Z_{gas} . In Section 5, we will discuss in detail how the $L_{[\text{C}_{\text{II}}]}/\text{SFR}$ ratio of the FIRE galaxies depends on gas metallicity, and interpret the results using the insights obtained from the toy models presented here.

3.2 Calculating ISRF distribution and multi-wavelength SEDs of galaxies using SKIRT

To predict the [C_{II}] luminosity of the ISM, it is essential to know the local UV ISRF strength. We calculate the ISRF distribution for the FIRE galaxies using the open-source¹⁶ 3D Monte Carlo dust RT code SKIRT (Baes et al. 2011; Baes & Camps 2015; Camps & Baes 2015) (version 8). SKIRT provides full treatment of absorption and anisotropic scattering by dust, and self-consistently computes dust thermal re-emission and dust temperature distribution for various astrophysical systems.

To prepare the galaxy snapshots as RT input models for SKIRT, we follow the prescription of Camps et al. (2016) (see also Trayford et al. 2017; Camps et al. 2018). We summarize the key points of the prescription here, and refer interested readers to the above-mentioned papers for the details.

For the analysis, each star particle of the galaxy is treated as a ‘single stellar population’ (SSP), and a spectrum of stellar emission is assigned to each particle using the STARBURST99 (Leitherer et al. 1999; Vazquez & Leitherer 2005) SED libraries according to the age, metallicity and initial mass of the particle. The RT calculations are performed on an equally spaced logarithmic wavelength grid consisting of 250 wavelength points spanning the wavelength range $\lambda = 0.01 - 1000 \mu\text{m}$. We launch 10^6 photon packages for each of the 250 point in the wavelength grid and for each of the stellar emission and following dust emission stages. The calculation iterates until convergence. To produce mock images and SEDs for the galaxies, we place mock detectors at an arbitrary ‘local’ distance of 10 Mpc from galaxy along multiple viewing angles to accumulate both spatially resolved as well as integrated fluxes at each wavelength grid point.

We assume that dust mass traces metal mass in galaxies (Hayward et al. 2011; Narayanan et al. 2015; Camps et al. 2016; Trayford et al. 2017; Liang et al. 2018, 2019, 2021; Ma et al. 2019; Cochrane et al. 2019, 2022; Vogelsberger et al. 2020; Shen et al. 2022) and adopt a constant dust-to-metal mass ratio $\delta_{\text{dzt}} = 0.4$ in gas cooler than 10^6 K. Hotter gas is assumed to be dust-free due to thermal sputtering (Draine & Salpeter 1979; Tielens et al. 1994). We adopt the Weingartner & Draine (2001b) dust model with Milky-Way size distribution for the case of $R_{\text{V}} = 3.1$. We discretize the spatial domain using an octree grid and keep subdividing grid cells until the cell contains less than $f = 3 \times 10^{-6}$ of the total dust mass and the V-band (0.55 μm) optical depth in each cell is less than unity. The highest grid level corresponds to a cell width of ~ 20 pc, *i.e.* about twice the minimal SPH smoothing length. We self-consistently calculate the self-absorption of dust emission and include the transient heating function to calculate non-local thermal equilibrium dust emission by transiently heated small grains and PAH molecules (Baes et al. 2011; Camps & Baes 2015). To account for the heating of dust by the cosmic microwave background, we adopt a correction to the dust temperature using equation (12) of da Cunha et al. (2013).

The final output of the SKIRT simulations includes the ISRF, J_{λ} ($\text{W cm}^{-3} \text{sr}^{-1}$), of each adaptive grid cell. We calculate the UV

¹⁴ The ionization energy of C²⁺ is 24.39 eV, which is greater than the ionization energy of hydrogen atom (13.6 eV).

¹⁵ The first ionization energy of carbon is 11.26 eV, which coincides with the lower frequency limit of the LW band (11.2 eV). Consequently, the transition from the H_I to the H₂ regions should align with the shift from C⁺-rich to C_I-rich regions when neglecting self-shielding of H₂ from LW radiation (Stecher & Williams 1967; Black & Dalgarno 1977; Federman et al. 1979; van Dishoeck & Black 1986). It is worth noting that H₂ self-shielding can be significant in high column density and low-metallicity environments (Draine & Bertoldi 1996; Madden et al. 1997, 2020; Wolfire et al. 2010; Gnedin & Draine 2014). In these environments, a substantial amount of C⁺ can be found within the envelope of the H₂ regions (Zone III). This has motivated some studies that suggest using [C_{II}] as a tracer for CO-dark H₂ gas (*e.g.* Madden et al. 1997, 2020; Langer et al. 2010, 2014; Velusamy et al. 2010; Pineda et al. 2013, 2014; Requena-Torres et al. 2016; Li et al. 2018; Dessauges-Zavadsky et al. 2020; Vizgan et al. 2022). However, in our simulations, we find that only a small fraction ($< 10\%$) of the [C_{II}] emission from our galaxies originates from the H₂-dominated regions (see Section 5.2). Therefore, we have not explicitly incorporated an additional zone in our model that is both H₂ and C⁺-rich, which would be situated between the current Zone II and Zone III.

¹⁶ Code repository: <https://skirt.ugent.be/version8/>

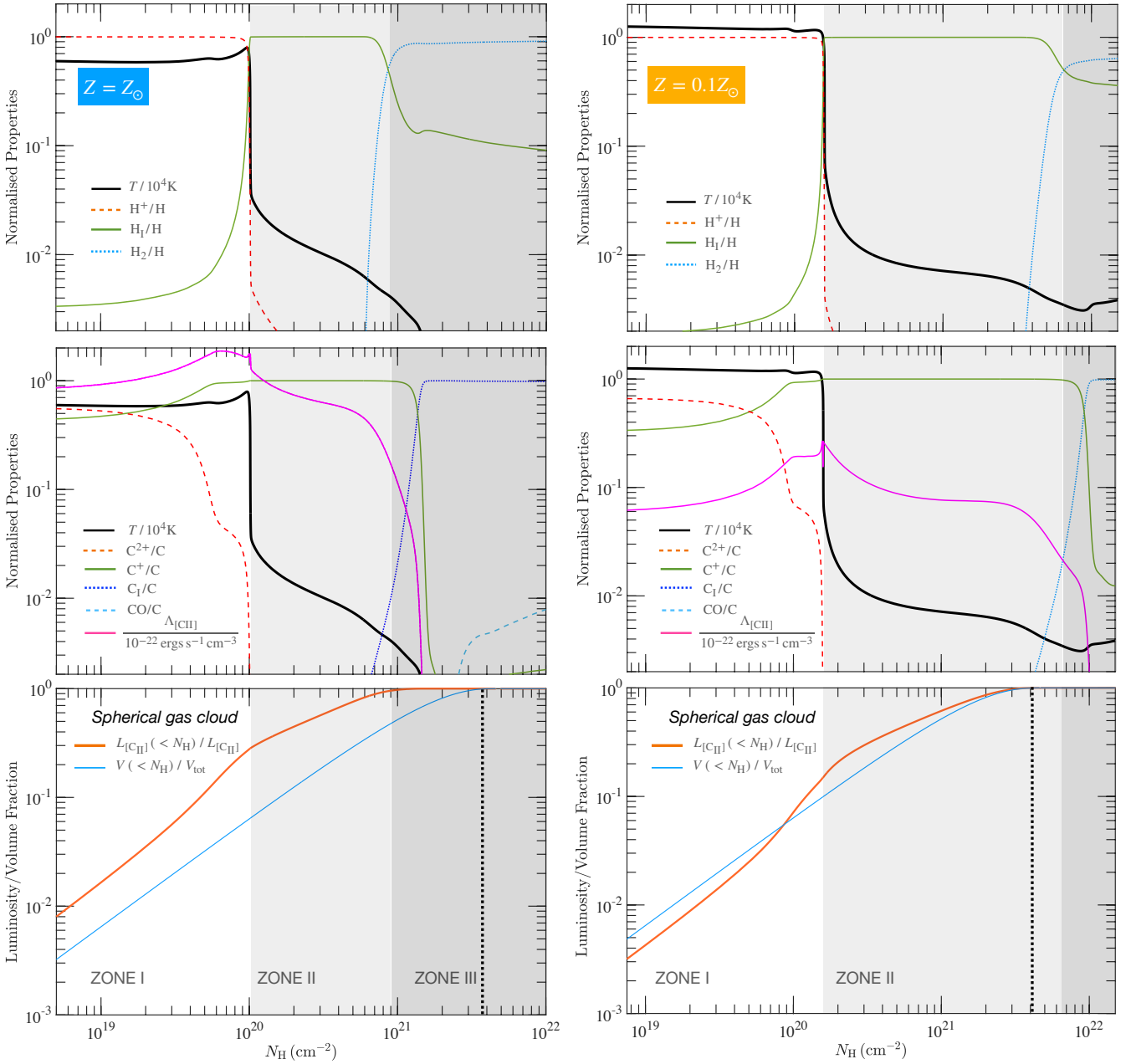


Figure 2. *Top and middle panels:* Ionization structures of a plane-parallel gas slab ($n_{\text{H}} = 50 \text{ cm}^{-3}$) irradiated by an external radiation field ($G = 200 G_0$) incident from the left in the figure predicted by the CLOUDY code. Dashed red, solid green and dotted blue lines in the *top (middle)* panels represent the abundance profiles for H^+ (C^{2+}), H_1 (C^+) and H_2 (C_1), respectively. Dashed cyan line in the *middle* panels represents the abundance profile for CO. Solid black line in the *top and middle* panels shows the profile of gas kinetic temperature (normalized by 10^4 K). Solid magenta line in the *middle* panels indicates the profile of $[\text{C}_{\text{II}}]$ cooling rate (normalized by $10^{-22} \text{ erg s}^{-1} \text{ cm}^{-3}$). *Bottom panels:* Cumulative fraction of $[\text{C}_{\text{II}}]$ luminosity (thick orange line) and volume (thin blue) as a function of gas column density (from the surface) of a spherical gas cloud ($M_{\text{cl}} = 10^5 M_{\odot}$, $n_{\text{H}} = 50 \text{ cm}^{-3}$) irradiated by an external radiation field ($G = 200 G_0$). Black dotted line marks the surface-to-centre column density of the cloud ($N_{\text{H}} = 4 \times 10^{21} \text{ cm}^{-2}$). The *left and right* columns correspond to the metal-rich and metal-poor models where gas metallicity of the slab (cloud) is set to Z_{\odot} and $1/10 Z_{\odot}$. For the metal-poor model, the dust-to-gas mass ratio (δ_{dgr}) becomes lower and therefore Lyman-Werner photons can penetrate deeper into the slab (cloud), resulting in larger $[\text{C}_{\text{II}}]$ -emitting region (Zone I + Zone II).

ISRF strength (G) for each cell by integrating J_{λ} over the Habing band (6 – 13.6 eV) and solid angle (Ω). G is assigned to every gas particle (‘cloud’) inside the cell for predicting its $[\text{C}_{\text{II}}]$ luminosity.

In Fig. 3, we show the UVJ composite image (*left panels*), $[\text{C}_{\text{II}}]$ surface brightness (*middle panels*), and G distribution (*right panels*) for the two selected FIRE galaxies calculated using CLOUDY and SKIRT. The *upper* panels show the results of a disc galaxy at $z = 0$

extracted from FIRE_{BOX}, whilst the *lower* panels show the results of a galaxy undergoing multiple mergers at $z = 6$ extracted from the MASSIVEFIRE simulation (Sim ID: D9). The $z = 6$ galaxy system has much stronger strength of ISRF (*right panels*) due to its higher SFR ($220 M_{\odot} \text{ yr}^{-1}$ vs. $4.5 M_{\odot} \text{ yr}^{-1}$) and shows higher $[\text{C}_{\text{II}}]$ surface brightness. $L_{[\text{C}_{\text{II}}]}$ of the $z = 6$ system and the $z = 0$ galaxy are $5.5 \times 10^8 L_{\odot}$ and $1.0 \times 10^8 L_{\odot}$, respectively.

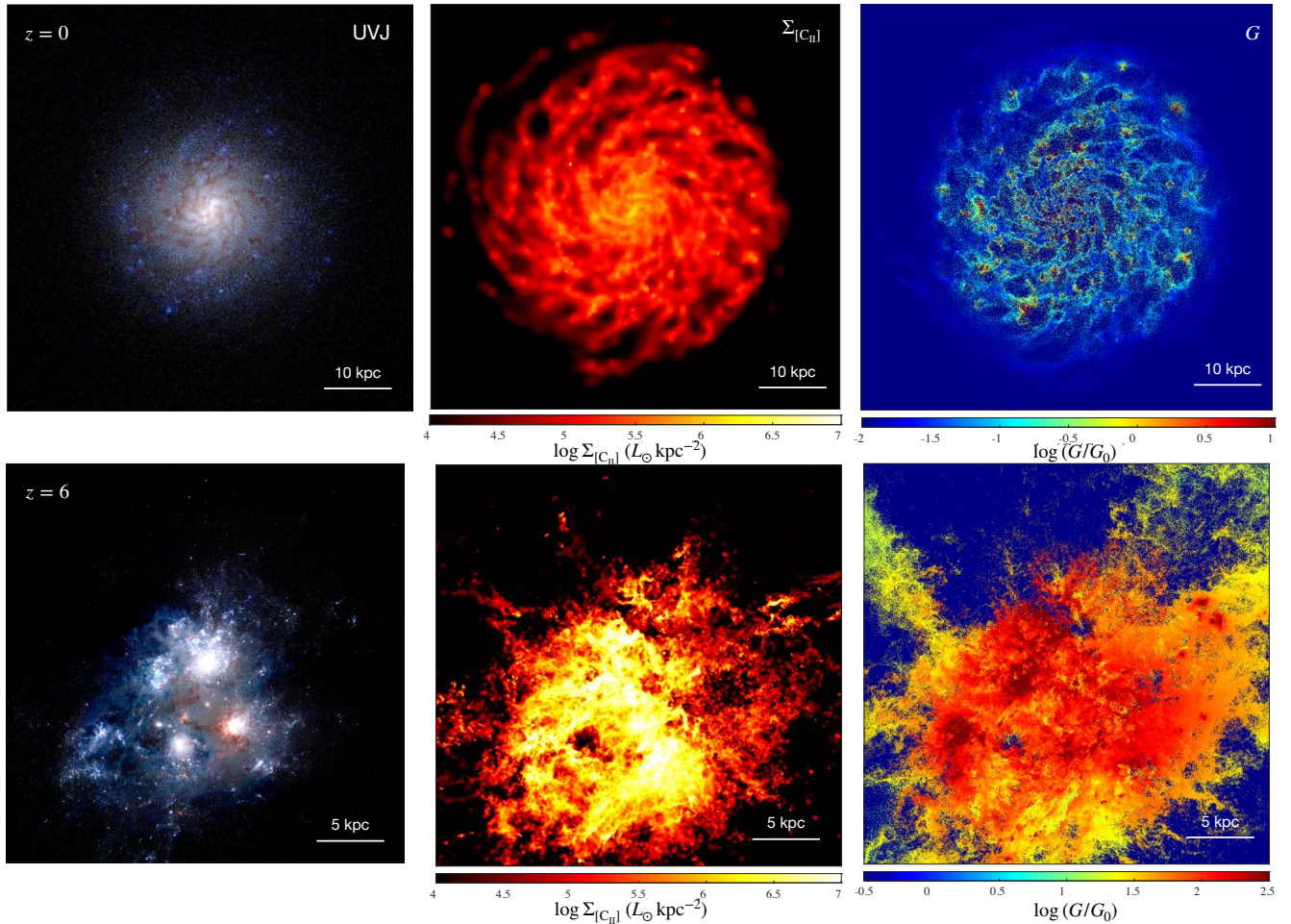


Figure 3. The UVJ false-colour image (*left*), $[C_{II}]$ surface brightness (*middle*) and the distribution of UV ISRF strength (G) (*right*) of selected FIRE galaxies. The *upper* panels show the results of a $z = 0$ disc galaxy from FIREbox (*c.f.* Fig.3 of Feldmann et al. 2023), while the *lower* panels correspond to a galaxy undergoing multiple mergers at $z = 6$ extracted from the MASSIVEFIRE ‘zoom-in’ suite.

4 COMPARISON WITH OBSERVATIONS

In this section, we compare the $L_{[C_{II}]}$ -SFR relation of the FIRE galaxies predicted by our model with the observational data at various redshifts. We separately discuss the results for three redshift regimes, $z = 0$ (Section 4.1), $1 \lesssim z \lesssim 5$ (Section 4.2) and $z \gtrsim 5$ (Section 4.3). We make this distinction because observations use different sample selection methods and the SFR of galaxies is estimated by different means of calibration in the three different regimes.

4.1 Local Universe (redshift $z = 0$)

Observations of the $L_{[C_{II}]}$ -SFR relation at $z = 0$ probe a very wide SFR range across several orders of magnitude. The selected samples include low-SFR systems such as dwarf galaxies as well as the extreme IR-luminous starbursts.

Three primary samples of nearby galaxies have been employed to calibrate the relation between $L_{[C_{II}]}$ and the SFR in normal star-forming galaxies (SFR $\approx 10^{-5} - 10 M_{\odot} \text{yr}^{-1}$): De Looze et al. (2011, hereafter referred to as L11), De Looze et al. (2014, hereafter referred to as L14), and Herrera-Camus et al. (2015, hereafter referred to as H15). These studies have consistently found a linear correlation between $L_{[C_{II}]}$ and SFR, and their calibrations are often used as benchmarks for high-redshift observations (galaxies below their

$L_{[C_{II}]}$ -SFR relation are considered to have a ‘ $[C_{II}]$ deficit’). However, it’s important to note that other evidence suggests this linear correlation can break down at high SFR at $z = 0$ (*e.g.* Díaz-Santos et al. 2013, 2017; Herrera-Camus et al. 2018), and whether we should use these relations as a ‘standard ruler’ is highly doubtful.

The L11 sample consists of 24 star-forming galaxies selected from the early compilation by Braucher et al. (2008) that have measurements at both the *Galaxy Evolution Explorer* (GALEX) FUV and the *Multi-band Imaging Photometer for Spitzer* (MIPS) $24 \mu\text{m}$ bands. The sample of L14 includes 48 nearby low-metallicity ($Z_{\text{gas}} \approx 0.03 - 0.55 Z_{\odot}$) dwarf galaxies extracted from the Dwarf Galaxy Survey (DGS, Madden et al. 2013) catalogue. Lastly, H15 study a sample consisting of 46 local star-forming galaxies chosen from the KINGFISH catalogue (Kennicutt et al. 2011), having very diverse integrated galaxy properties and ISM environments. All these studies have excluded the sources with AGN features.

Both L11 and L14 derive the SFR of their sample using GALEX FUV and MIPS $24 \mu\text{m}$ fluxes (*i.e.* SFR = $\beta (L_{\text{FUV, obs}} + \alpha \times L_{24 \mu\text{m}})$) but with different calibration. Specifically, L11 and L14 use the calibration by Zhu et al. (2008) ($\alpha = 6.31$) and Hao et al. (2011) ($\alpha = 3.89$), respectively. H15, on the other hand, derive the SFR of their sample using a hybrid of different methods: for 27 galaxies in their sample, SFR is derived using the $H_{\alpha} + 24 \mu\text{m}$ calibration by Calzetti et al. (2007) (equation 7). For the other 8 galaxies, they

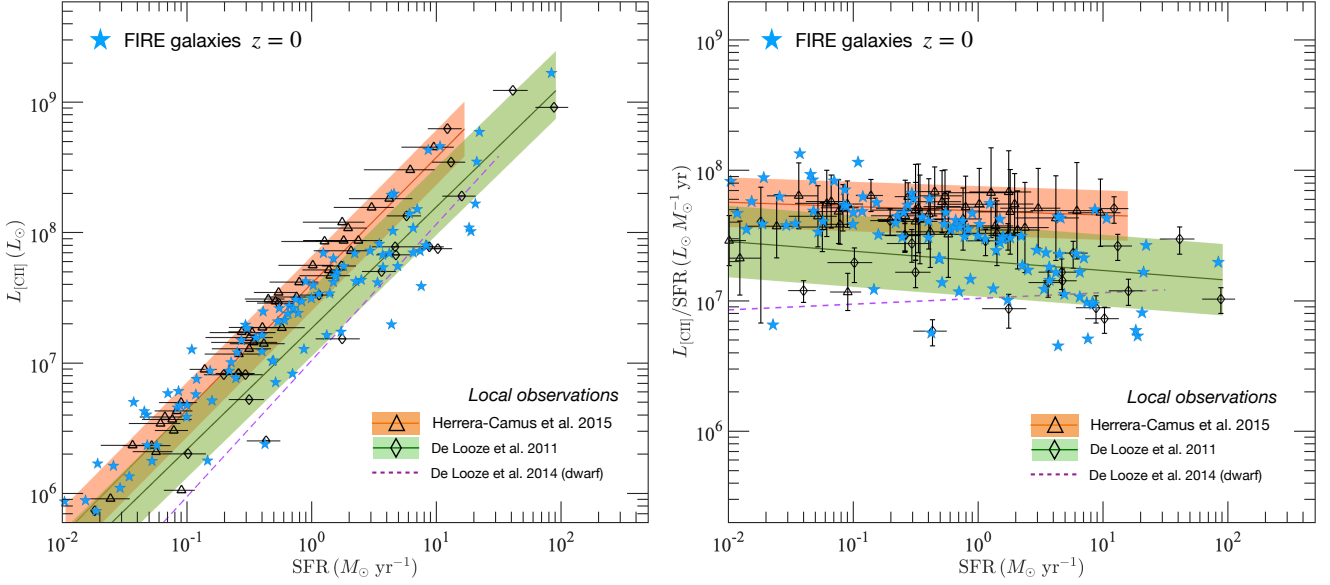


Figure 4. The L_{CII} vs. SFR (*left* panel) and $L_{\text{CII}}/\text{SFR}$ vs. SFR (*right* panel) relations of the $z = 0$ galaxies. The filled cyan stars in the two panels show the result of the FIRE galaxies. Black triangles and diamonds show the observational data of [Herrera-Camus et al. \(2015\)](#) (H15) and [De Looze et al. \(2011\)](#) (L11), and the orange and green lines indicate the best-fit linear relation of the H15 and L11 samples, respectively. The coloured shaded regions indicate the 1σ scatter of the data around the best-fit linear relation of the observed samples. Purple dashed line in the two panels represents the best-fit linear relation to the low-metallicity dwarf galaxy sample of [De Looze et al. \(2014\)](#) (L14). The result of the FIRE galaxies at $z = 0$ is in good agreement with the observational data.

Table 2. Observed and simulated scaling relations between SFR and L_{CII} of local galaxies, *i.e.* $L_{\text{CII}}/L_{\odot} = A(\text{SFR}/M_{\odot} \text{yr}^{-1})^B$.

Galaxy sample	SFR range ($M_{\odot} \text{yr}^{-1}$)	Median SFR ($M_{\odot} \text{yr}^{-1}$)	A	B	1σ scatter
De Looze et al. (2011)	0.02 – 88	1.75	7.31 ± 0.06	0.93 ± 0.06	0.26 dex
De Looze et al. (2014)	6×10^{-4} – 56	0.12	7.10 ± 0.11	1.05 ± 0.07	0.43 dex
Herrera-Camus et al. (2015)	10^{-3} – 9.6	0.34	7.63 ± 0.03	0.97 ± 0.03	0.21 dex
FIRE (this work)	0.01 – 1 [†]	0.19	7.48 ± 0.06	0.87 ± 0.06	0.27 dex

[†] Here we do not include the galaxies in the sample having $\text{SFR} > 1 M_{\odot} \text{yr}^{-1}$ for the fitting because they exhibit a reduced $L_{\text{CII}}/\text{SFR}$ ratio (a [CII] deficit).

use the FUV+24 μm calibration by [Leroy et al. \(2008\)](#) (equations D10 and D11). And lastly, for the remaining 11 galaxies having no measurement of either $\text{H}\alpha$ nor FUV flux, SFR is derived based solely on their 24 μm flux using the calibration by [Calzetti et al. \(2007\)](#) (equation 6). In Table 2, we show the SFR range as well as the median SFR of the three samples (L11, L14 and H15). We also show in the table the best-fit parameter values for the scaling relation

$$\log(L_{\text{CII}}/L_{\odot}) = A + B \log(\text{SFR}/M_{\odot} \text{yr}^{-1}) \quad (3)$$

for the three samples as well as the 1σ scatter (in dex) of the data around the best-fit relation. Note that for the galaxies of the L11 and H15 samples whose SFR is derived using the FUV+24 μm fluxes, we have re-calibrated their SFR following [Hao et al. \(2011\)](#) as has been done by L14 for a fair comparison. All the SFR calibrations are based on the [Kroupa \(2002\)](#) initial mass function (IMF).

From Table 2, we can see that the three samples all exhibit an almost linear correlation between L_{CII} and SFR, though having noticeable difference in the normalization. The H15 sample has the highest normalization among the three samples. It is higher than that of the L11 sample by 0.32 dex. This offset may partly be due to the

difference in sample selection. Another potential cause is that H15 adopt different SFR indicators and calibration methods compared with L11 for a large fraction of the galaxies in their sample. The offset between the L11 and L14 samples (0.21 dex), on the other hand, is mainly due to the difference in *sample selection* since L11 and L14 adopt the same SFR indicators (FUV+24 μm fluxes) for their entire samples and we have re-calibrated their results following the same method of [Hao et al. \(2011\)](#). The lower normalization of the L14 relation is very likely due to the relatively lower Z_{gas} of the dwarf galaxies they use for the study, as has been explicitly stated in L14.

In Fig. 4, we show the L_{CII} -SFR relation of the three samples (L11, L14 and H15) in the *left* panel. To more clearly show the difference in the normalization of these scaling relations, we present the $L_{\text{CII}}/\text{SFR}$ vs. SFR relation of the same samples in the *right* panel. In both panels, we also present the results for the FIRE sample¹⁷ $z = 0$ (filled cyan stars) for comparison with the observational data.

¹⁷ We calculate the SFR of the FIRE galaxies by averaging over a timescale of the last 100 Myrs.

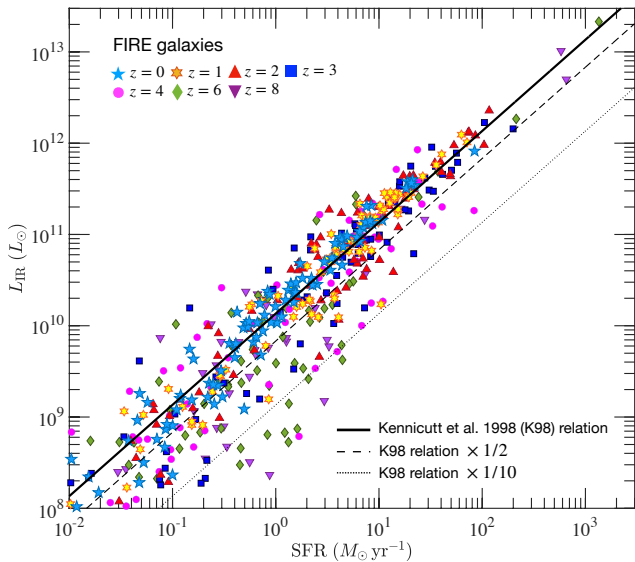


Figure 5. The L_{IR} vs. SFR relation of FIRE galaxies at different redshifts (cyan stars for $z = 0$, yellow hexagons for $z = 1$, red triangles for $z = 2$, blue squares for $z = 3$, magenta circles for $z = 4$, green diamonds for $z = 6$ and purple downward diamonds for $z = 8$). The diagonal solid black line indicates the K98 relation, *i.e.* $L_{\text{IR}} (L_{\odot}) = 1.36 \times 10^{10} \text{SFR} (M_{\odot} \text{yr}^{-1})$. The dashed and dotted lines indicate the modified K98 relations where the normalization is lower than the solid black line by a factor of 2 and 10, respectively. The K98 relation (solid black line) fits well to the galaxies at high SFR.

Note that for the L11 and H15 samples, we show both the data of the individual sources as well as the best-fit scaling relation for each sample, whereas for the L14 sample, we only present the best-fit scaling relation (purple dashed line) for reference. The L14 sample has systematically lower gas metallicity than the other two observational samples as well as the FIRE galaxy sample at $z = 0$.

The FIRE simulations, combined with our line model, produce the $L_{[\text{CII}]}$ -SFR relation at $z = 0$ (cyan stars) that is in good agreement with the local star-forming samples of L11 (black diamonds) and H15 (black triangles). The best-fit parameter values for the FIRE galaxies over the SFR range of $0.01 - 1 M_{\odot} \text{yr}^{-1}$ are $A = 7.48 \pm 0.06$ and $B = 0.87 \pm 0.06$, and the 1σ scatter of the data points around the best-fit relation is 0.27 dex, similar to the L11 and H15 samples (see Table 2). When including galaxies with $\text{SFR} > 1 M_{\odot} \text{yr}^{-1}$, the best-fit parameters become $A = 7.42 \pm 0.03$ and $B = 0.78 \pm 0.03$. Note that we have excluded galaxies with $\text{SFR} < 0.01 M_{\odot} \text{yr}^{-1}$ from the fitting to avoid the regime where galaxy statistics can be contaminated by shot noise due to the resolution limit of the simulation (Feldmann 2017).

The reduced linearity in the $L_{[\text{CII}]}$ -SFR relation at high SFR is driven by galaxies with $\text{SFR} \gtrsim 1 M_{\odot} \text{yr}^{-1}$, showing a reduced $L_{[\text{CII}]} / \text{SFR}$ ratio compared to those with lower SFR (see the right panel of Fig. 4). Such a trend is not clearly present in any of the three (L11, L14, and H15) observational samples. However, it's important to note that these samples do not contain a statistically large number of galaxies at $\text{SFR} \gtrsim 1 M_{\odot} \text{yr}^{-1}$. Other studies examining local LIRGs and ULIRGs have found clear evidence of a [CII] deficit at high L_{IR} ($\sim \text{SFR}$) (see below).

The $L_{[\text{CII}]} - L_{\text{IR}}$ relation of $z = 0$ galaxies

A number of observational studies have probed the relation between $L_{[\text{CII}]}$ and L_{IR} (or L_{FIR} ¹⁸) of local galaxies.

L_{IR} (or L_{FIR}) can be a good proxy for galaxy SFR when the stellar light of a galaxy is heavily absorbed by dust (*e.g.* Kennicutt 1998; Salim & Narayanan 2020). Galaxies having higher SFR tend to be more gas/dust-rich and have higher gas density. Therefore, they tend to have higher dust opacity (*e.g.* Whitaker et al. 2017). We show in Fig. 5 the L_{IR} vs. SFR relation of the FIRE galaxies at different redshifts, where L_{IR} is calculated using their SEDs produced by SKIRT. It can be seen that at $z = 0$, the FIRE galaxies (cyan stars) well follow the Kennicutt (1998, hereafter K98) relation¹⁹, *i.e.*

$$L_{\text{IR}} (L_{\odot}) = 1.36 \times 10^{10} \text{SFR} (M_{\odot} \text{yr}^{-1}) \quad (4)$$

at $\text{SFR} \gtrsim 1 M_{\odot} \text{yr}^{-1}$ (or $L_{\text{IR}} \gtrsim 10^{10} L_{\odot}$). The K98 relation is derived assuming that all radiative energy of the young stars is absorbed and re-emitted by dust and AGN radiation does not contribute to dust heating. At $\text{SFR} < 1 M_{\odot} \text{yr}^{-1}$, however, the $z = 0$ FIRE galaxies show larger scatter. Some of these galaxies are below the K98 relation by over 0.3 dex (indicating that less than half of the radiative energy of the young stars gets re-emitted at FIR by dust). These are the galaxies having relatively low dust opacity²⁰. Nonetheless, L_{IR} appears to be a good SFR tracer for the $z = 0$ galaxies at $\text{SFR} \gtrsim 1 M_{\odot} \text{yr}^{-1}$ in the FIRE simulations.

In Fig. 6, we present the observed $L_{[\text{CII}]}$ vs. L_{IR} (left panel) and the $L_{[\text{CII}]} / L_{\text{IR}}$ vs. L_{IR} (right panel) relations for local galaxy samples sourced from various studies. These samples include the GOALS (“Great Observatories All-sky LIRG Survey”; Armus et al. 2009) sample, consisting of 241 galaxies studied by Díaz-Santos et al. (2013, 2017), the SHINING (“Survey with Herschel of the ISM in Nearby Infrared Galaxies”; PI: Sturm) sample of 52 galaxies analyzed by Herrera-Camus et al. (2018), as well as those studied by Malhotra et al. (2001), Brauher et al. (2008), Sargsyan et al. (2012), Farrah et al. (2013), Magdis et al. (2014), Cormier et al. (2015) (note: the same DGS sample as in L14), Hughes et al. (2017) and Contursi et al. (2017). For those studies that use L_{FIR} as an SFR indicator, we convert the reported L_{FIR} of the galaxies to L_{IR} by multiplying it by 1.6, following Sanders et al. (2003). Additionally, in the same figure, we include the data of the $z = 0$ FIRE galaxies, where L_{IR} is determined by integrating the SED produced by SKIRT over the wavelength range of $8 - 1000 \mu\text{m}$.

The observed samples contain a large number of galaxies that are IR-luminous ($L_{\text{IR}} \gtrsim 10^{11} L_{\odot}$, corresponding to $\text{SFR} \gtrsim 10 M_{\odot} \text{yr}^{-1}$ following equation 4). With these statistically large samples, the $L_{[\text{CII}]} / L_{\text{IR}}$ ($\sim L_{[\text{CII}]} / \text{SFR}$) ratio of the $z = 0$ galaxies appear to

¹⁸ In the literature, ‘ L_{IR} ’ is used to denote the bolometric IR luminosity of galaxy that is integrated over the wavelength range $8 - 1000 \mu\text{m}$, whereas ‘ L_{FIR} ’ represents the FIR luminosity of galaxy ($42.5 - 122.5 \mu\text{m}$). Both L_{IR} and L_{FIR} are commonly adopted as SFR indicators for heavily dust-obscured galaxies.

¹⁹ We adopt the K98 relation for the Kroupa (2002) IMF using the stellar population synthesis (SPS) model STARBURST99, assuming a constant star formation history lasting for 1 Gyr (see Hao et al. 2011 for the details). The original relation (*i.e.*, $L_{\text{IR}} / L_{\odot} = 5.8 \times 10^9 \text{SFR} / (M_{\odot} \text{yr}^{-1})$) was derived for the Salpeter IMF based on the older SPS model of Leitherer & Heckman (1995), and for a shorter starburst period ($t_{\text{age}} = 10 - 100 \text{Myrs}$).

²⁰ It can be seen from Fig. 5 that some of the simulated galaxies (particularly those having low SFR) lie above the K98 relation, which seem to break the energy conservation law. These are in fact the galaxies that are recently quenched after a strong starburst whose dust is heated mainly by the stars older than 100 Myrs (see *e.g.* Hayward et al. 2014).

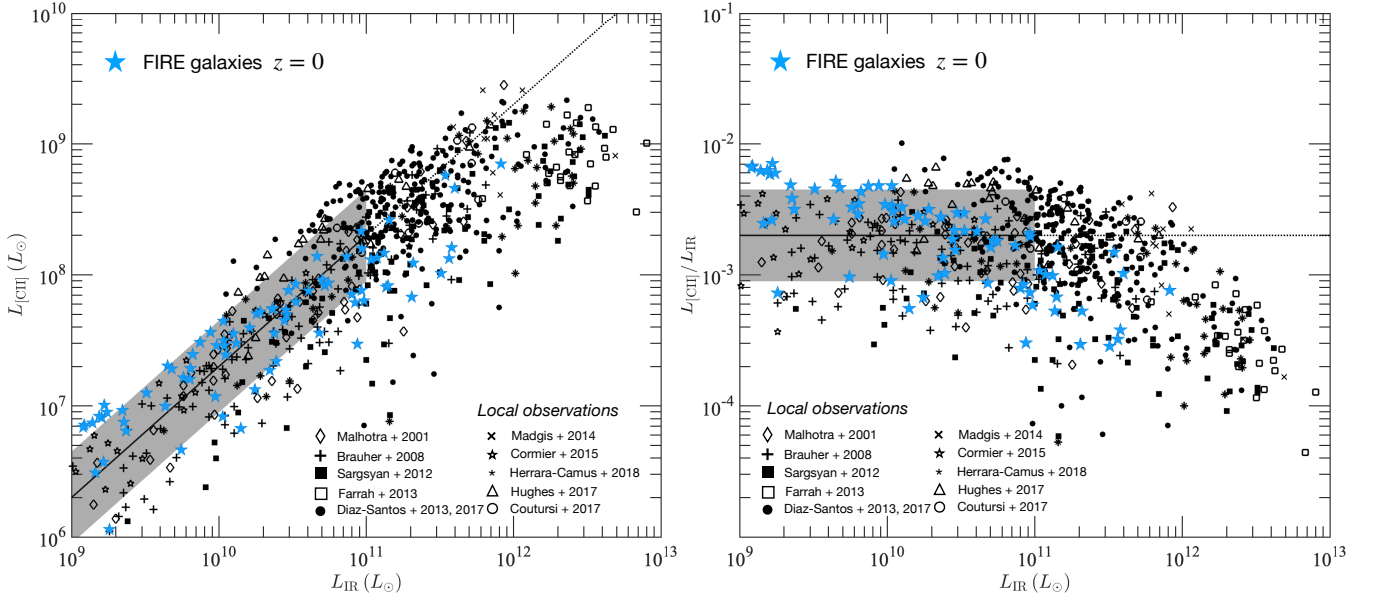


Figure 6. The L_{CII} vs. L_{IR} (left panel) and the $L_{\text{CII}}/L_{\text{IR}}$ vs. L_{IR} (right panel) relations of $z = 0$ galaxies. In the two panels, cyan stars show the result of the FIRE galaxies, whereas black symbols indicate the observational data from different studies, including Malhotra et al. (2001) (diamond), Brauher et al. (2008) (crosses), Sargsyan et al. (2012) (filled squares), Farrah et al. (2013) (empty squares), Díaz-Santos et al. (2013, 2017) (filled circles), Magdis et al. (2014) (‘X’s), Cormier et al. (2015) (empty stars), Herrera-Camus et al. (2018) (asterisks), Hughes et al. (2017) (triangles) and Contursi et al. (2017) (empty circles). Observations show that $L_{\text{CII}}/L_{\text{IR}}$ ratio of galaxies is nearly a constant at $10^9 \lesssim L_{\text{IR}} \lesssim 10^{11} L_{\odot}$, but declines with L_{IR} at $L_{\text{IR}} \gtrsim 10^{11} L_{\odot}$. In the two panels, black line (solid at $L_{\text{IR}} < 10^{11} L_{\odot}$ and dotted at $L_{\text{IR}} \geq 10^{11} L_{\odot}$) indicates the median $L_{\text{CII}}/L_{\text{IR}}$ ratio ($\approx 2 \times 10^{-3}$) of the galaxies having $L_{\text{IR}} < 10^{11} L_{\odot}$ and grey shaded bar indicates the 1σ scatter of the $L_{\text{CII}}/L_{\text{IR}}$ ratio of these galaxies. FIREBOX successfully reproduces the observed L_{CII} vs. L_{IR} relation at $z = 0$.

show a clear decline with L_{IR} at $L_{\text{IR}} \gtrsim 10^{11} L_{\odot}$ ([CII] deficit), albeit with a large scatter ($1\sigma = 0.3$ dex) at given L_{IR} . From $L_{\text{IR}} = 10^{11}$ to $10^{13} L_{\odot}$, $L_{\text{CII}}/L_{\text{IR}}$ decreases from 2×10^{-3} to 10^{-4} , over a factor of ten. At $L_{\text{IR}} \lesssim 10^{11} L_{\odot}$, on the other hand, $L_{\text{CII}}/L_{\text{IR}}$ of the observed galaxies is a constant. Overall, the observational and the simulated data agree well with each other (on both the mean value and level of scatter). In particular, the FIRE sample exhibits a mild [CII] deficit at $L_{\text{IR}} \gtrsim 10^{11} L_{\odot}$ at $z = 0$, which is in agreement with the observational data. Note, however, that our FIRE sample at $z = 0$ does not include any ULIRGs (*i.e.* $L_{\text{IR}} \gtrsim 10^{12} L_{\odot}$) at $z = 0$.

4.2 High redshifts ($1 \lesssim z \lesssim 5$)

Observational studies have investigated the L_{CII} -SFR relation of galaxies at $1 \lesssim z \lesssim 5$, including *e.g.* Ivison et al. (2010); Stacey et al. (2010); Valtchanov et al. (2011); Brisbin et al. (2015); Gullberg et al. (2015, 2018); Schaerer et al. (2015b); Umehata et al. (2017); Zanella et al. (2018); Hashimoto et al. (2019b); McKinney et al. (2020). Their samples consist of roughly 80 galaxies in total (see Table 3 for the details). Most of these galaxies have substantial SFR ($\text{SFR} \gtrsim 100 M_{\odot} \text{yr}^{-1}$) and are IR-luminous ($L_{\text{IR}} \gtrsim 10^{12} L_{\odot}$). This is in stark contrast with the local observations (see Section 4.1), which probe the galaxies having much lower SFR (see Table 2). Note that a large fraction of the selected galaxies in this redshift regime are uncovered by wide-field sub-mm galaxy surveys, *e.g.* the South Pole Telescope (SPT; Vieira et al. 2010; Carlstrom et al. 2011) survey (Weiß et al. 2013; Gullberg et al. 2015).

We derive the SFR of the selected galaxies from their measured L_{IR} (see Table 3) using the K98 relation (equation 4) assuming that the galaxies are heavily dust-obscured. Note that at high redshifts,

the K98 relation may only apply to the more massive and starburst galaxies. High- z galaxies are metal and dust-poorer than the $z = 0$ galaxies at given mass (or SFR), and therefore only the more massive and gas-rich systems have high enough dust opacity leading to total obscuration of stellar light. We can see from Fig. 5 that the K98 relation (solid black line) fits well the high- z FIRE galaxies at $\text{SFR} \gtrsim 100 M_{\odot} \text{yr}^{-1}$ (or $L_{\text{IR}} \gtrsim 10^{12} L_{\odot}$. Note: For the $z = 1$ galaxies, the K98 relation fits well to the data down to $L_{\text{IR}} \approx 10^{11} L_{\odot}$). At lower SFR, the high- z galaxies exhibit larger scatter and they, on the average, have lower L_{IR} at given SFR than the $z = 0$ galaxies due to their reduced dust opacity.

The galaxies selected at $1 \lesssim z \lesssim 5$ typically have a good sampling of photometric data points in the dust continuum, which are obtained by observations with multiple IR and millimetre instruments (*Spitzer*, *Herschel*, ALMA and etc). The shape of the dust SED of these galaxies is therefore well constrained. This results in relatively small uncertainty in the estimate of their L_{IR} .

The [CII] line of these galaxies is measured with different instruments (see Table 3). For instance, Stacey et al. (2010) and Brisbin et al. (2015) measure the [CII] line of the 20 galaxies at $z \approx 1 - 2$ of their samples using the redshift (z) and Early Universe Spectrometer (ZEUS; Stacey et al. 2007; Hailey-Dunsheath 2009) on the 10.4 m Caltech Submillimeter Observatory (CSO). Gullberg et al. (2015) measure the [CII] line of the 16 SMGs selected from the SPT catalogue (Weiß et al. 2013) using the SPIRE Fourier Transform Spectrometer (FTS; Griffin et al. 2010) onboard *Herschel* (for the galaxies at $z < 3$) and the First Light APEX Sub-millimetre Heterodyne receiver (FLASH; Heyminck et al. 2006) (for the galaxies at $z > 3$). For the remaining galaxies (~ 40), their [CII] line is measured with ALMA (at Band 7, 8 and 9 for the galaxies at $z \sim 4$,

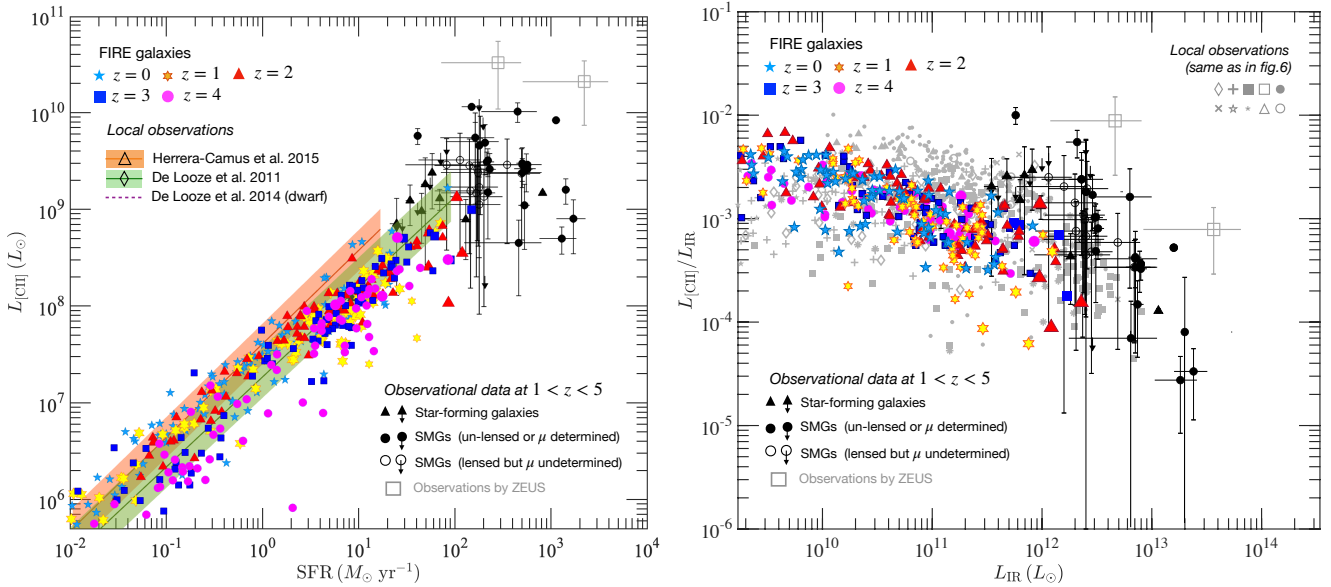


Figure 7. The $L_{[\text{CII}]}$ vs. SFR (*left* panel) and the $L_{[\text{CII}]} / L_{\text{IR}}$ vs. L_{IR} (*right* panel) relations of galaxies at $z = 0$ and high redshifts. In both panels, filled coloured symbols represent the FIRE galaxies (cyan stars for $z = 0$, yellow hexagons for $z = 1$, red triangles for $z = 2$, blue squares for $z = 3$ and magenta circles for $z = 4$). Black symbols (filled and empty) show the observational data of galaxies at $1 \lesssim z \lesssim 5$ (see Table 3 for the details). Specifically, black circles and black triangles correspond to SMGs and other star-forming galaxies, respectively. For the gravitationally-lensed galaxies, their $[\text{CII}]$ and IR luminosities have been corrected by the lensing magnification factor μ reported in the literature. Those having direct measurement of μ as well as the un-lensed galaxies are marked by filled symbols (triangles and circles), whereas the 16 lensed SPT galaxies whose μ is extrapolated (μ has been assumed to be 14.1 by Gullberg et al. 2015) are shown by empty circles. The two grey empty squares represent the stacked result of the galaxy samples of Stacey et al. (2010) and Brisbin et al. (2015). The $[\text{CII}]$ line of the two samples is measured with the redshift and Early Universe Spectrometer (ZEUS) and their data systematically offsets from that of the other galaxy samples. For reference, we also show in the *left* (*right*) panel the observational results of the local galaxy samples as shown in Fig. 4 (Fig. 6). Both observations and FIRE simulations show that high- z ($1 \lesssim z \lesssim 5$) galaxies exhibit a $[\text{CII}]$ deficit at high L_{IR} similar to local galaxies.

$z \sim 3$ and $z \sim 2$, respectively). ALMA observations often marginally resolve a galaxy spatially in $[\text{CII}]$, whereas observations with ZEUS, APEX/FLASH and SPIRE FTS do not.

It should be particularly noted that a large number (26) of the selected galaxies (mostly SMGs) in this regime are gravitationally-lensed systems (see Table 3). Hence, one important source of uncertainty in the estimates of their *intrinsic* $L_{[\text{CII}]}$ and L_{IR} (\sim SFR) is the lensing magnification factor μ . To observationally determine μ of a lensed source requires spatially resolved imaging. Note that 16 of the selected SPT galaxies in this regime, however, are not spatially resolved by the observations and their μ is unknown. Gullberg et al. (2015) adopt a constant $\mu = 14.1$ to de-magnify the luminosities of all the 16 galaxies. This is the mean of the μ of the only 4 galaxies in their selected SPT sample, which is determined using the spatially resolved ALMA 860 μm broadband imaging of dust continuum by Hezaveh et al. (2013).

In Fig. 7, we show the $L_{[\text{CII}]}$ -SFR relation (*left* panel) of the observed samples at $1 \lesssim z \lesssim 5$, where we have converted the SFR of all galaxies from their L_{IR} using the K98 relation following the observational studies. We show the stacked result for the samples of Stacey et al. (2010) and Brisbin et al. (2015) by grey empty squares. Both studies measure $[\text{CII}]$ line with ZEUS, and both obtain systematically higher $L_{[\text{CII}]} / \text{SFR}$ ratio of galaxies than the other studies using different instruments (by about one dex) at similar SFR. For the other studies, we explicitly show the data of each individual source in their samples. Specifically, we show the result of the SMGs by black circles (empty and filled), whilst the other star-forming galaxies are denoted by black triangles. For all the lensed galaxies, both $L_{[\text{CII}]}$ and L_{IR} are de-magnified by the observationally determined μ when available. For the 16 SPT galaxies having no

determined μ (indicated by empty black circles in Fig. 7), we correct their luminosities by an assumed $\mu = 14.1$ following Gullberg et al. (2015). For reference, we also show the $L_{[\text{CII}]}$ -SFR relation of local galaxies by L11, L14 and H15 in the same (*left*) panel.

The bulk of the selected samples at $1 \lesssim z \lesssim 5$ have higher SFR than the local samples of L11, L14 and H15. Only the few galaxies at $z \approx 1 - 2$ of the Zanella et al. (2018) sample overlap with the SFR range of the most actively star-forming galaxies of the L11 sample, and they appear to follow the same $L_{[\text{CII}]}$ -SFR relation. At higher SFR (*i.e.* $\text{SFR} \gtrsim 100 M_{\odot} \text{yr}^{-1}$), the high- z galaxy samples show a larger scatter in the $L_{[\text{CII}]}$ -SFR relation compared to the local samples (L11, L14 and H15). Apart from that, the high- z samples show a decline of $L_{[\text{CII}]} / \text{SFR}$ ratio with increasing SFR at above $100 M_{\odot} \text{yr}^{-1}$ (corresponding to $L_{\text{IR}} \gtrsim 10^{12} L_{\odot}$). This trend can be more clearly seen in the *right* panel, where we show the $L_{[\text{CII}]} / L_{\text{IR}}$ ($\approx L_{[\text{CII}]} / \text{SFR}$ at high SFR) ratio of the same high- z galaxy samples as a function of their L_{IR} (\sim SFR). From $L_{\text{IR}} = 10^{12} L_{\odot}$ to $10^{13} L_{\odot}$, the $L_{[\text{CII}]} / L_{\text{IR}}$ (or $L_{[\text{CII}]} / \text{SFR}$) ratio of the high- z samples decreases by roughly a factor of 50 (excluding the Stacey et al. 2010 and Brisbin et al. 2015 samples). This $[\text{CII}]$ deficit at high L_{IR} is similar to what has been found with the local galaxy samples (indicated by the filled grey symbols in Fig. 7).

In the same figure, we also show the results of the FIRE galaxies at high redshifts. Specifically, we show the $L_{[\text{CII}]}$ -SFR (*left* panel) and the $L_{[\text{CII}]} / L_{\text{IR}}$ - L_{IR} (*right* panel) relations of the FIRE galaxies at $z = 1$ (yellow hexagons), $z = 2$ (red triangles), $z = 3$ (blue squares) and $z = 4$ (magenta circles). For reference, we also show in the two panels the results of the FIRE sample at $z = 0$ (cyan stars).

The FIRE galaxies follow a roughly linear $L_{[\text{CII}]}$ -SFR scaling rela-

Table 3. The observed $L_{[\text{CII}]}$ -SFR relation of galaxies at high redshifts.

Name [†]	z	$\log(L_{\text{IR}}/L_{\odot})^{\S}$	$\log(L_{[\text{CII}]} / L_{\odot})^{\ddagger, \S, \parallel}$	Galaxy type [#]	AGN	μ	References*
ID 7118	1.7290	12.06±0.01	< 9.70 (ALMA 9)	MS	No	–	[1, 2]
GS IRS61	1.759	12.46±0.13	< 8.31 (ALMA 9)	SB	No	–	[3, 4]
ID 9834	1.7644	11.99±0.02	9.11 ± 0.07 (ALMA 9)	MS	No	–	[1, 2]
ID 2910	1.7686	11.76±0.08	< 9.08 (ALMA 9)	MS	No	–	[1, 2]
ID 2861	1.8102	12.00±0.03	< 9.58 (ALMA 9)	MS	No	–	[1, 2]
ID 6515	1.8438	11.68±0.04	9.09 ± 0.12 (ALMA 9)	MS	No	–	[1, 2]
ID 9347	1.8505	11.80±0.05	8.98 ± 0.14 (ALMA 9)	MS	No	–	[1, 2]
ID 9681	1.8852	11.84±0.04	9.26 ± 0.20 (ALMA 9)	MS	No	–	[1, 2]
ID 8490	1.9056	11.54±0.06	8.85 ± 0.20 (ALMA 9)	MS	No	–	[1, 2]
ID 10049	1.9200	11.60±0.06	< 8.78 (ALMA 9)	MS	Yes	–	[1, 2]
GS IRS20	1.923	13.06±0.12	9.17 ± 0.01 (ALMA 9)	SB	Yes	–	[3, 4]
ID 10076	1.9462	11.91±0.03	9.38 ± 0.14 (ALMA 9)	MS	No	–	[1, 2]
MACS J0451+0006	2.013	11.08±0.04	8.08 ± 0.04 (ALMA 9)	MS	No	49 ± 5	[5, 6, 7]
GRB 080207	2.0865	12.26±0.05	8.89 ± 0.12 (ALMA 9)	MS	No	–	[8]
SPT 0551-50	2.123	11.89±0.05	< 9.33 (SPIRE FTS)	SMG	No	(14.1 ± 7.8)	[9, 10]
SPT 0512-59	2.234	12.29±0.04	9.45 ± 0.09 (SPIRE FTS)	SMG	No	(14.1 ± 7.8)	[9, 10]
SMM J2135	2.3259	12.08±0.07	8.25 ± 0.11 (SPIRE FTS)	SMG	No	32.5 ± 4.5	[12, 13]
SDP.130	2.625	12.40±0.02	< 10.14 (SPIRE FTS)	SMG	No	6 ± 1	[14, 15]
SPT 0538-50	2.782	12.44±0.03	< 9.95 (SPIRE FTS)	SMG	No	20.9 ± 4.2	[9, 10]
ALESS 49.1	2.943	12.85±0.06	9.48 ± 0.12 (ALMA 8)	SMG	No	–	[16, 17, 18]
ALESS 57.1	2.943	12.87±0.06	9.04 ± 0.17 (ALMA 8)	SMG	No	–	[16, 17, 18]
SDP.81	3.042	12.32±0.08	10.06 ± 0.01 (SPIRE FTS)	SMG	No	25 ± 7	[14, 15]
SPT 0103-45	3.090	12.38±0.02	9.41 ± 0.06 (APEX/FLASH)	SMG	No	(14.1 ± 7.8)	[9, 10]
LAB1-ALMA3	3.0993	11.76	9.41 ± 0.06 (ALMA 8)	MS	No	–	[19, 20]
LAB1-ALMA1	3.1	11.54	< 8.9 (ALMA 8)	MS	No	–	[19, 20]
LAB1-ALMA2	3.1	11.60	< 8.9 (ALMA 8)	MS	No	–	[19, 20]
SPT 0550-53	3.129	12.08±0.09	9.46 ± 0.09 (APEX/FLASH)	SMG	No	(14.1 ± 7.8)	[9, 10]
SPT 0529-54	3.369	12.36±0.04	9.74 ± 0.04 (APEX/FLASH)	SMG	No	9.4 ± 1.0	[9, 10]
SPT 0532-50	3.399	12.69±0.07	9.46 ± 0.08 (APEX/FLASH)	SMG	No	(14.1 ± 7.8)	[9, 10]
SPT 0300-46	3.596	12.40±0.11	9.05 ± 0.11 (APEX/FLASH)	SMG	No	(14.1 ± 7.8)	[9, 10]
SPT 2147-50	3.761	12.39±0.06	9.38 ± 0.06 (APEX/FLASH)	SMG	No	(14.1 ± 7.8)	[9, 10]
SPT 0418-47	4.224	12.48±0.03	9.49 ± 0.03 (APEX/FLASH)	SMG	No	21.0 ± 3.5	[9, 10]
SPT 0113-46	4.232	12.20±0.09	9.51 ± 0.10 (APEX/FLASH)	SMG	No	(14.1 ± 7.8)	[9, 10]
SDP.141	4.24	12.52±0.12	9.48 ± 0.07 (APEX/FLASH)	SMG	No	10 – 30	[11]
SPT 2311-54	4.281	12.40±0.04	9.23 ± 0.06 (APEX/FLASH)	SMG	No	(14.1 ± 7.8)	[9, 10]
SPT 0345-47	4.296	12.84±0.04	9.37 ± 0.04 (APEX/FLASH)	SMG	No	(14.1 ± 7.8)	[9, 10]
COSMOS-AzTEC-1	4.342	13.21±0.09	9.80 ± 0.04 (ALMA 7)	SMG	No	–	[21, 22]
AS2UDS.0568.0	4.404	13.30±0.08	9.20 ± 0.08 (ALMA 7)	SMG	No	–	[23, 24]
ALESS 61.1	4.4189	12.49±0.03	9.18 ± 0.17 (ALMA 7)	SMG	No	–	[24, 25, 26]
UDS 47.0	4.4201	12.50±0.06	9.42 ± 0.12 (ALMA 7)	SMG	No	–	[24, 26]
AS2UDS.0051.0	4.421	12.85±0.20	9.38 ± 0.05 (ALMA 7)	SMG	No	–	[23, 24]
AS2UDS.0104.0	4.423	12.85±0.20	9.46 ± 0.05 (ALMA 7)	SMG	No	–	[23, 24]
SGP 38326 (SMG1)	4.4237	13.20±0.09	9.92 ± 0.05 (ALMA 7)	SMG (SB)	No	–	[27]
SGP 38326 (SMG2)	4.4289	12.90±0.09	9.46 ± 0.05 (ALMA 7)	SMG (SB)	No	–	[27]
BRI 0952-0115	4.4337	12.40±0.25	9.66 ± 0.25 (APEX/FLASH)	SMG (SB)	No	4.5 ± 2.8	[28, 29, 30]
SPT 2103-60	4.435	12.41±0.03	9.70 ± 0.06 (APEX/FLASH)	SMG	No	(14.1 ± 7.8)	[9, 10]
AS2UDS.0232.0	4.443	13.26±0.15	8.70 ± 0.09 (ALMA 7)	SMG	No	–	[23, 24]
ALESS 65.1	4.4445	12.49±0.03	9.51 ± 0.09 (ALMA 7)	SMG	No	–	[24, 25, 26]
AS2UDS.0109.0	4.450	12.90±0.06	9.42 ± 0.03 (ALMA 7)	SMG	No	–	[23, 24]
AS2UDS.0002.1	4.4611	13.38±0.08	8.90 ± 0.11 (ALMA 7)	SMG	No	≤1.5 – 2	[23, 24]
AS2UDS.0643.0	4.4614	13.11±0.22	8.95 ± 0.15 (ALMA 7)	SMG	No	≤1.5 – 2	[23, 24]
AS2UDS.0208.0	4.4615	12.89±0.01	9.42 ± 0.06 (ALMA 7)	SMG	No	≤1.5 – 2	[23, 24]
SPT 0441-46	4.477	12.45±0.02	9.13 ± 0.11 (APEX/FLASH)	SMG	No	(14.1 ± 7.8)	[9, 10]
SPT 2146-55	4.567	12.31±0.05	9.19 ± 0.10 (APEX/FLASH)	SMG	No	(14.1 ± 7.8)	[9, 10]
W2246–0526	4.601	14.34±0.08	9.79 ± 0.03 (ALMA 7)	DOG	Yes	–	[31]
ALESS 73.1	4.7555	12.46±0.03	9.69 ± 0.14 (ALMA 7)	SMG (SB)	Yes	–	[24, 26, 32]
SPT 2132-58	4.768	12.37±0.04	9.17 ± 0.08 (APEX/FLASH)	SMG	No	(14.1 ± 7.8)	[9, 10]
HDF850.1	5.185	12.58±0.07	9.38 ± 0.05 (IRAM/PdBI)	SMG	No	1.5 – 1.7	[33, 34]
HLSJ091828.6+514223	5.24	13.04±0.10	9.98 ± 0.01 (SMA)	SMG	No	8.9 ± 1.9	[35]
SPT 2319-55	5.293	12.28±0.03	9.00 ± 0.06 (APEX/FLASH)	SMG	No	(14.1 ± 7.8)	[9, 10]
SPT 0346-52	5.656	13.39±0.02	9.97 ± 0.06 (APEX/FLASH)	SMG	No	5.4 ± 0.2	[9, 10]
SPT 0243-49	5.699	12.40±0.04	< 9.40 (APEX/FLASH)	SMG	No	(14.1 ± 7.8)	[9, 10]

(Continue on next page)

Table 3 – *continued* The observed $L_{[\text{CII}]}$ -SFR relation of galaxies at high redshifts.

Name [†]	z	$\log(L_{\text{IR}}/L_{\odot})^{\S}$	$\log(L_{[\text{CII}]} / L_{\odot})^{\ddagger, \parallel}$	Galaxy type [#]	AGN	μ	References*
HerMESFLS3	6.3369	13.34 ± 0.05	9.83 ± 0.10 (CARMA)	SMG	No	2.2 ± 0.3	[36, 37]
SPT 0311-58-E	6.900	12.66 ± 0.12	9.62 ± 0.06 (ALMA 6)	SMG	No	1.3	[38]
SPT 0311-58-W	6.900	13.52 ± 0.09	9.66 ± 0.06 (ALMA 6)	SMG	No	2.2	[38]

[†] The table does not include the 20 galaxies ($z \approx 2$) in the samples of [Stacey et al. \(2010\)](#) and [Brisbin et al. \(2015\)](#), of which the $[\text{CII}]$ line is measured by ZEUS. The $L_{[\text{CII}]} / L_{\text{IR}}$ vs L_{IR} relation of these two samples systematically offsets from the others that use different instrument to measure $[\text{CII}]$ line (see Fig. 7).

[§] For the gravitationally-lensed galaxies, $L_{[\text{CII}]}$ and L_{IR} have been de-magnified by the reported lensing magnification factor μ . For those SPT galaxies having no direct measurement of μ (galaxies are not spatially resolved by any observation), we adopt a constant $\mu = 14.1$ as is done by [Gullberg et al. \(2015\)](#), which is the mean of the four galaxies (SPT 0538-50, SPT 0529-54, SPT 0418-47 and SPT 0346-52) in the same sample that is observationally determined via lensing modelling.

[‡] For the $[\text{CII}]$ -undetected galaxies, we show the 3σ upper confidence limit.

^{||} IRAM/PdBI: the IRAM Plateau de Bure Interferometer ([Guilloteau et al. 1992](#)); SMA: the Submillimeter Array ([Ho et al. 2004](#)); CARMA: the Combined Array for Research in Millimeter-wave Astronomy ([Woody et al. 2004](#)). Note that the three telescopes have produced spatially resolved line emission maps of $[\text{CII}]$ for high- z SMGs (HDF850.1, HLSJ091828.6+514223 and HerMESFLS3) as ALMA does.

[#] SMG: sub-mm galaxies; MS: ‘main-sequence’ galaxies; SB: starburst galaxies; DOG: hot dust-obscured galaxies (galaxies uncovered by surveys at near-infrared wavelengths, which have strong IR emission from warm dust, *e.g.* [Dey et al. 2008](#); [Eisenhardt et al. 2012](#)).

* References: [1]: [Zanella et al. \(2018\)](#), [2]: [Elbaz et al. \(2011\)](#), [3]: [McKinney et al. \(2020\)](#), [4]: [Kirkpatrick et al. \(2015\)](#), [5]: [Schaerer et al. \(2015b\)](#), [6]: [Sklias et al. \(2014\)](#), [7]: [Jones et al. \(2010\)](#), [8]: [Hashimoto et al. \(2019b\)](#), [9]: [Gullberg et al. \(2015\)](#), [10]: [Weiß et al. \(2013\)](#), [11]: [Cox et al. \(2011\)](#), [12]: [Iverson et al. \(2010\)](#), [13]: [Swinbank et al. \(2010\)](#), [14]: [Valtchanov et al. \(2011\)](#), [15]: [Hopwood et al. \(2011\)](#), [16]: [Rybak et al. \(2019\)](#), [17]: [Wardlow et al. \(2018\)](#), [18]: [da Cunha et al. \(2021\)](#), [19]: [Umehata et al. \(2017\)](#), [20]: [Geach et al. \(2016\)](#), [21]: [Tadaki et al. \(2018\)](#), [22]: [Tadaki et al. \(2020\)](#), [23]: [Cooke et al. \(2018\)](#), [24]: [Swinbank et al. \(2014\)](#), [25]: [Swinbank et al. \(2012\)](#), [26]: [Gullberg et al. \(2018\)](#), [27]: [Oteo et al. \(2016\)](#), [28]: [Maiolino et al. \(2009\)](#), [29]: [Priddey & McMahon \(2001\)](#), [30]: [Lehar et al. \(2000\)](#), [31]: [Díaz-Santos et al. \(2015\)](#), [32]: [Breuck et al. \(2014\)](#), [33]: [Neri et al. \(2014\)](#), [34]: [Walter et al. \(2012\)](#), [35]: [Rawle et al. \(2014\)](#), [36]: [Riechers et al. \(2013\)](#), [37]: [Cooray et al. \(2014\)](#), [38]: [Marrone et al. \(2018\)](#).

tion over the SFR range of $\approx 0.01 - 100 M_{\odot} \text{ yr}^{-1}$ at each redshift (*left* panel), though having considerable scatter ($1\sigma \approx 0.2 - 0.35$ dex). The normalization of the relation, however, shows clear redshift evolution. From $z = 0$ to $z = 4$, the mean $L_{[\text{CII}]} / \text{SFR}$ ratio of the FIRE sample declines by about one dex (see the *left* panel of Fig. 7). This indicates that using the $L_{[\text{CII}]}$ -SFR relation derived by [L11](#) or [H15](#) will lead to a systematic underestimate of SFR of galaxies at high redshifts.

On the other hand, the $L_{[\text{CII}]} / L_{\text{IR}}$ ratio of the FIRE galaxies does not evolve as much with redshift between $z = 0 - 4$ (*right* panel). From $z = 0$ to $z = 4$, the mean $L_{[\text{CII}]} / L_{\text{IR}}$ ratio of the FIRE galaxies decreases by 0.5 dex, which is less than the decrease of the $L_{[\text{CII}]} / \text{SFR}$ ratio (~ 1 dex). Obviously, the reason for the discrepancy in the redshift evolution of the two ratios ($L_{[\text{CII}]} / \text{SFR}$ and $L_{[\text{CII}]} / L_{\text{IR}}$) is the redshift evolution of the L_{IR} -SFR relation of the galaxies (see Fig. 5 for the result of the FIRE galaxies, and also the observational data of *e.g.* [Whitaker et al. 2017](#)) — at fixed SFR, galaxies at higher redshift have on average lower dust opacity and thus a smaller fraction of stellar radiation is absorbed and re-emitted at far-IR. The mean $L_{\text{IR}} / \text{SFR}$ ratio of galaxies therefore decreases with redshift.

Apart from that, it is clear from the *right* panel that the FIRE galaxies at $z = 1 - 4$ show a similar decrease of $L_{[\text{CII}]} / L_{\text{IR}}$ ratio with L_{IR} like the local $z = 0$ FIRE galaxies (cyan stars), and the decrease appears to be more significant at $L_{\text{IR}} \gtrsim 5 \times 10^{11} L_{\odot}$. The sharp decrease of $L_{[\text{CII}]} / L_{\text{IR}}$ at the high L_{IR} end is in line with the trend in the observational data at similar redshifts. In Section 5, we will examine in detail the origin of this ‘ $[\text{CII}]$ deficit’ at high L_{IR} and we will show that it is mainly driven by the decrease of gas mass per unit SFR, or *depletion timescale* ($t_{\text{dep}} \equiv M_{\text{gas}} / \text{SFR}$), of galaxies with SFR.

Note that at $L_{\text{IR}} \approx 10^{12} L_{\odot}$, the observed $L_{[\text{CII}]} / L_{\text{IR}}$ ratio of the galaxies at high redshifts (black symbols) appears to be higher than that of the observed $z = 0$ galaxy samples (grey symbols) as well as the FIRE galaxies (coloured symbols). The mean $L_{[\text{CII}]} / L_{\text{IR}}$ ratio

is roughly in agreement with the upper bound of the FIRE galaxies at similar L_{IR} . This can possibly be due to selection effect. Those galaxies at $L_{\text{IR}} \approx 10^{12} L_{\odot}$ are mostly the ‘main-sequence’ (MS) galaxies at $z \approx 1.5 - 2$ selected by [Zanella et al. \(2018\)](#), which are expected to have longer t_{dep} (*i.e.* gas mass per unit SFR) than starburst galaxies at the same redshift (*e.g.* [Genzel et al. 2015](#); [Aravena et al. 2016](#); [Miettinen et al. 2017](#); [Tacconi et al. 2018](#); [Feldmann 2020](#)) and hence higher $L_{[\text{CII}]} / L_{\text{IR}}$ (note: $L_{[\text{CII}]} / \text{SFR} \propto t_{\text{dep}}^{0.7}$, equation 30). The FIRE sample as well as the local observed galaxy samples, on the contrary, consist of galaxies across the star-forming MS as well as starburst galaxies, exhibiting a wide range of t_{dep} .

Finally, we note that the observational data in this redshift regime has large uncertainties due to the large fraction of gravitationally-lensed galaxies included in the samples (see Table 3). First of all, as mentioned above, many of the lensed galaxies do not have determined magnification factor μ (marked by empty circles in Fig. 7). Even for those whose μ is derived from either the rest-UV (with *Hubble Space Telescope*) or dust continuum imaging (with ALMA), it is not yet certain whether their $[\text{CII}]$ luminosity is magnified by the same level, given that the $[\text{CII}]$ and stellar/dust emission of galaxies may have different spatial configuration (*e.g.* [Cochrane et al. 2019](#); [Fujimoto et al. 2019](#); [Matthee et al. 2019](#); [Novak et al. 2020](#); [Fudamoto et al. 2022](#)) and thus the different emission components may have different μ due to the effect of differential lensing (*e.g.* [Blain 1999](#); [Hezaveh et al. 2012](#); [Serjeant 2012](#); [Cañameras et al. 2018](#); [Yang et al. 2019a](#); [Harrington et al. 2021](#)). Hence, it is important to obtain spatially resolved imaging of both $[\text{CII}]$ and dust emission for lensed galaxies and re-examine the *intrinsic* $L_{[\text{CII}]} / L_{\text{IR}}$ ratio of these galaxies (note: most of the lensed SMGs do not have spatially resolved $[\text{CII}]$ imaging, see Table 3).

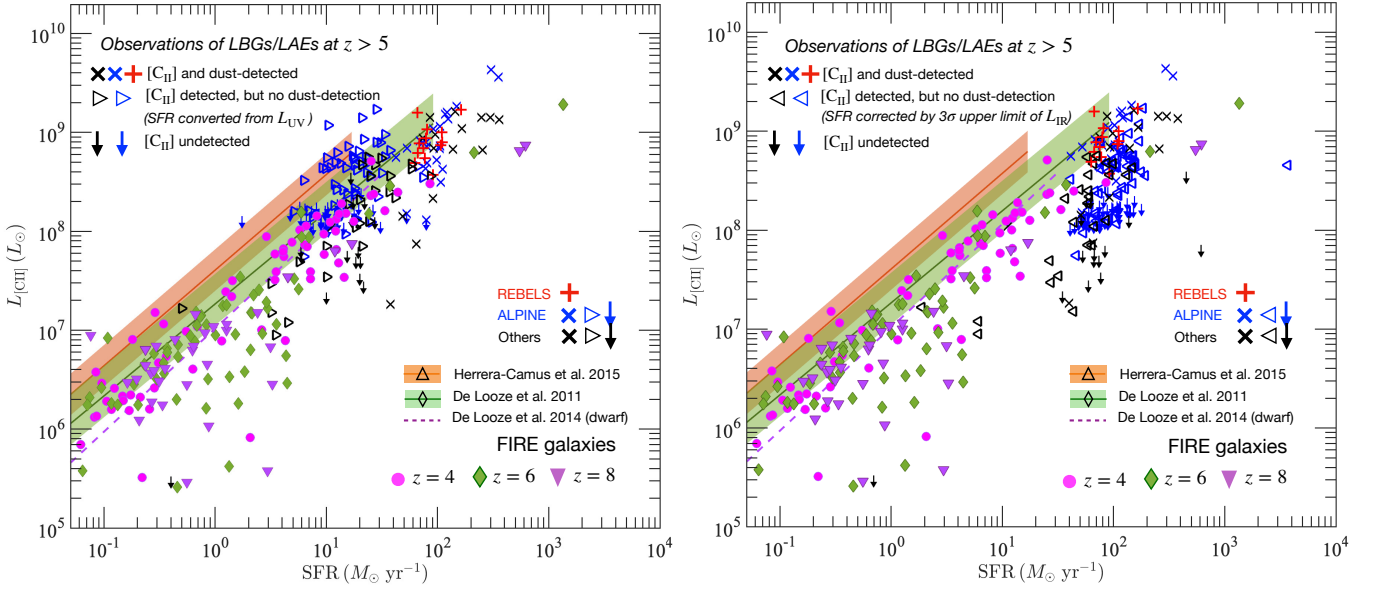


Figure 8. Comparison of the $L_{[\text{CII}]}$ -SFR relation of the FIRE galaxies with the observational data at high redshifts. In the two panels, we show the result of the FIRE galaxies at $z = 4$, $z = 6$ and $z = 8$ by magenta circles, green diamonds and purple downward triangles, respectively. We also show in the two panels the observational data of the rest-UV-selected star-forming galaxies at $z \geq 5$, including the ones targeted by the ALPINE (blue symbols) and REBELS (red symbols) ALMA surveys as well as the others targeted by the other observations (black symbols) (see Table 4 for the details). The galaxies having both confirmed $[\text{CII}]$ and dust continuum detection are indicated by crosses (REBELS) and ‘X’s (red for ALPINE and black for others). The galaxies having no $[\text{CII}]$ detection are shown by downward arrows in both panels. The location of the arrows indicate the 3σ upper limit of their $L_{[\text{CII}]}$. For the ones having $[\text{CII}]$ but without dust detection (meaning that their SFR_{IR} is uncertain), we show the relation between their $L_{[\text{CII}]}$ and the lower (upper) SFR limit in the left (right) panel by rightward (leftward) triangles. For reference, we also show the result of local ($z = 0$) observations of normal star-forming galaxies (SFGs) by L11, L14 and H15 in the two panels. The FIRE sample at $z = 4 - 8$ shows systematically lower $L_{[\text{CII}]}/\text{SFR}$ ratio than the local SFGs, in particular at low SFR. The observed galaxy samples at $z \geq 5$ show similar $[\text{CII}]$ deficit if T_{eqv} follows equation (7) (assuming $\delta_{\text{dtr}} = 0.4$).

4.3 Early galaxies (redshift $z \geq 5$)

Observational studies on the $L_{[\text{CII}]}$ -SFR relation at $z \geq 5$ depend mainly on the rest-frame UV-selected galaxies whose redshift has previously been confirmed either spectroscopically or via the Lyman break ‘drop-out’ technique (Hodge & da Cunha 2020). Their $[\text{CII}]$ and dust emission are constrained in follow-up observational campaigns with ALMA, which has the power to spatially resolve the distant galaxies down to the scale of ~ 1 physical kpc. The majority of the UV-selected galaxies at this epoch are unlensed.

There have been two major observational campaigns for searching for $[\text{CII}]$ line of galaxies at $z \geq 5$. The ALPINE ALMA Large Program (Le Fèvre et al. 2020; Béthermin et al. 2020) in cycle-5 targeted a sample of 118 UV-selected star-forming galaxies at $4.5 < z < 6$ with $M_{\text{UV, AB}} < -20.2$ and identified $[\text{CII}]$ emission (at $> 3.5\sigma$ level) in 75 galaxies of them (Schaerer et al. 2020). More recently, the REBELS Large Program (Bouwens et al. 2022) in Cycle-7 studied a sample of 40 UV-bright ($M_{\text{UV, AB}} < -21.4$) galaxies at $6.5 < z < 7.7$ and confirmed $[\text{CII}]$ detection (at $> 7\sigma$) in 18 galaxies in their sample (Ferrara et al. 2022). Other observations targeting the LBGs/LAEs at $z \geq 5$ have identified $[\text{CII}]$ emission in another > 35 sources in total. The most distant galaxy that has a $[\text{CII}]$ detection to date is MACS1149-JD1 (Hashimoto et al. 2018), a gravitationally-lensed ($\mu = 10$) galaxy at $z = 9.11$ (Carniani et al. 2020; see also Inoue et al. 2016 and Laporte et al. 2019). We provide a summary of the star-forming galaxies at $z \geq 5$ having confirmed $[\text{CII}]$ detection in Table 4 (excluding quasar host galaxies).

The SFR of these UV-selected galaxies has been derived based on their L_{UV} and L_{IR} . Because the galaxies at $z \geq 5$ typically do not have

good photometric sampling of the dust continuum (e.g. Casey et al. 2018b; Liang et al. 2019; Faisst et al. 2020b), L_{IR} has frequently been converted from the ALMA broad-band flux density (measured at band 6 or 7 for galaxies at $z \geq 5$) using the standard modified-blackbody (MBB) function of the form (e.g. Hildebrand 1983; Hayward et al. 2011)

$$S_{\nu_0} = \frac{(1+z)}{d_L^2} \kappa_\nu M_{\text{dust}} B_\nu(T), \quad (5)$$

where ν_0 is the observing frequency (note: $\nu_0 = 345$ GHz for ALMA band 7 and $\nu_0 = 230$ GHz for ALMA band 6), S_{ν_0} is the broad-band flux density at ν_0 , $\nu = (1+z)\nu_0$ is the rest-frame frequency, κ_ν is the dust opacity (per unit dust mass) at ν , M_{dust} is the dust mass of galaxy, T is the ‘dust temperature’, $B_\nu(T)$ is the Planck function and d_L is the luminosity distance. L_{IR} is then converted from S_{ν_0} using (see Section 3.1.3 of Liang et al. 2019 for the details)

$$L_{\text{IR}} = \frac{\mathcal{D} d_L^2 T^{4+\beta_{\text{dust}}}}{(1+z) \kappa_\nu B_\nu(T)} S_{\nu_0}, \quad (6)$$

where $\beta_{\text{dust}} \approx 2.0$ is the dust emissivity spectral index (e.g. Dunne et al. 2000; Draine et al. 2007) and \mathcal{D} is a parameter that depends on the shape of the dust opacity curve. The derived L_{IR} (and hence the obscured SFR) therefore depends mainly on the assumed ‘dust temperature’. It should be noted that recent cosmological simulations show that the true SED of high- z galaxies may significantly differ from the standard MBB function (e.g. Liang et al. 2019; Ma et al. 2019, and also Casey 2012, Casey et al. 2018b) and T does not faithfully reflect the *physical* temperature of dust in galaxies (e.g. Behrens et al. 2018; Liang et al. 2019). Liang et al. (2019) defines

the ‘dust temperature’ that one would need to obtain the correct L_{IR} and match the observed S_{ν_0} under the assumption that the SED has the shape of a standard MBB function (equation 5) to be the ‘equivalent dust temperature’ (T_{eqv}).

Using a sample of high- z galaxies produced by the MASSIVEFIRE suite (Feldmann et al. 2016, 2017), Liang et al. (2019) derived the best-fitting formula for T_{eqv} using redshift and dust-to-gas mass ratio (δ_{dzt}) as variables, *i.e.*

$$T_{\text{eqv}} = T_0 (1+z)^\alpha (\delta_{\text{dzt}}/0.4)^\gamma. \quad (\text{L19}) \quad (7)$$

For ALMA band 7 (6) fluxes, the best-fitting parameter values are $T_0 = 26.9$ (24.5) K, $\alpha = 0.31$ (0.36) and $\gamma = -0.13$ (-0.15). The increase of T_{eqv} with redshift is related to the enhanced level of star formation activity in galaxies (*i.e.* higher specific SFR) (Safarzadeh et al. 2016; Ma et al. 2019; Liang et al. 2019; Sommovigo et al. 2020). The anti-correlation with δ_{dzt} , on the other hand, is due to the fact that an increase of δ_{dzt} leads to a higher dust opacity, which in turn results in a ‘colder’ dust SED shape of galaxies (Scoville 2013; Faisst et al. 2017; Liang et al. 2019). Observationally, δ_{dzt} of high- z galaxies has not yet been constrained.

Often, it is easier to detect the $[\text{CII}]$ line than the dust continuum of galaxies at $z \geq 5$. For example, 75 out of the 118 (63.6%) galaxies in the ALPINE sample have confirmed detection of $[\text{CII}]$ emission, whilst only 21 (17.8%) of them have confirmed detection of dust continuum. Almost all dust-detected galaxies have detection of $[\text{CII}]$ line. The detection limit of $[\text{CII}]$ of the current ALMA observations is about $10^8 L_\odot$.

We convert the sub-mm broad-band flux density (S_{ν_0}) of the dust-detected galaxies (or the 3σ upper limit of S_{ν_0} for the dust-undetected galaxies) to L_{IR} (the upper limit of L_{IR}) consistently using T_{eqv} that follows equation (7) (assuming $\delta_{\text{dzt}} = 0.4$) to make a fair comparison between different observed samples and our theoretical predictions using FIRE galaxies. We compute the SFR of the observed galaxies using their measured L_{UV} and the derived L_{IR} following Hao et al. (2011), *i.e.* $\text{SFR} (M_\odot \text{ yr}^{-1}) = 1.58 \times 10^{-10} (L_{\text{UV}} + 0.46L_{\text{IR}}) (L_\odot)$, for the Kroupa (2002) IMF. For the dust-undetected galaxies, we estimate the lower and upper bounds of their SFR, where the former is converted from their L_{UV} assuming no dust emission (*i.e.* $L_{\text{IR}} = 0$), whilst the latter accounts for the upper limit of L_{IR} converted from the 3σ upper limit of S_{ν_0} .

In Fig. 8, we show the observed $L_{[\text{CII}]}$ -SFR relation of the rest-UV-selected galaxy samples at $z \geq 5$ (see Table 4 for the details) together with the result of the FIRE galaxies at $z = 4$, $z = 6$ and $z = 8$ in the two panels. For the observed galaxies having no detection of dust, we show the relation between their $L_{[\text{CII}]}$ (for the $[\text{CII}]$ -undetected galaxies, the 3σ upper limit of their $L_{[\text{CII}]}$) and the lower and upper bound of their SFR, respectively, in the *left* and *right* panels of the figure. For reference, we also show in Fig. 8 the observed $L_{[\text{CII}]}$ -SFR relation of the local star-forming galaxies by L11, L14 and H15.

It can be seen that the FIRE galaxies at $z = 4 - 8$ lie systematically below the observed local $L_{[\text{CII}]}$ -SFR relations (and thus also the FIRE galaxies at $z = 0$) over the broad SFR range of $\approx 0.1 - 10^3 M_\odot \text{ yr}^{-1}$, showing a $[\text{CII}]$ deficit. This appears to be in agreement with the observational data.

At $\text{SFR} \geq 100 M_\odot \text{ yr}^{-1}$, most of the observed galaxies at $z \geq 5$ have both $[\text{CII}]$ and dust detections and thus their (dust-obscured) SFR is more reliably constrained. The mean $L_{[\text{CII}]}/\text{SFR}$ ratio of these galaxies is lower than the L11 relation (solid green line) by 0.22 dex, which is close to the 1σ scatter of the L11 relation (see Table 2). The FIRE galaxies at $z \geq 4$ are about 2σ below the L11 relation in the same SFR range, which seem to show a slightly more prominent ‘deficit’ than the observed samples.

At $\text{SFR} \lesssim 100 M_\odot \text{ yr}^{-1}$, most of the $z \geq 5$ galaxies do not have confirmed dust detection with the current ALMA observations, and a large fraction of them do not have confirmed $[\text{CII}]$ detections neither (marked by downward arrows). The uncertainty in the SFR estimate of these dust-undetected galaxies can be as large as a factor of ~ 5 ($\approx 20 - 100 M_\odot \text{ yr}^{-1}$, see Fig. 8). Such a large uncertainty is due to the high T_{eqv} of galaxies at $z \geq 5$ ($T_{\text{eqv}} \gtrsim 45$ K for $\delta_{\text{dzt}} = 0.4$, see equation (7)), so that even a low noise level (typically $\sigma \sim 10 \mu\text{Jy}$, see Table 4) of the ALMA observations is converted to a relatively high upper bound of L_{IR} (and hence SFR_{IR}). From Fig. 8, it can be seen that the predicted $L_{[\text{CII}]}$ -SFR relation of the FIRE galaxies does not conflict with the observational constraints over $\text{SFR} \approx 10 - 100 M_\odot \text{ yr}^{-1}$. In particular, for the $[\text{CII}]$ -undetected galaxies, the 3σ upper limit of their $L_{[\text{CII}]}$ (marked by downward arrows) appears to be above the data points of the FIRE galaxies at similar SFR when their dust emission is insignificant, namely, $\text{SFR} \approx \text{SFR}_{\text{UV}}$ (see the *left* panel of Fig. 8).

At $\text{SFR} \lesssim 10 M_\odot \text{ yr}^{-1}$, we lack enough observational data for a reliable constraint on the $L_{[\text{CII}]}$ -SFR relation at $z \geq 5$ because galaxies having such low SFR are intrinsically faint. The galaxy having the lowest SFR ($\text{SFR} \approx 1 M_\odot \text{ yr}^{-1}$) that has had $[\text{CII}]$ measurement to date at $z \geq 5$ is MS0451-H (Knudsen et al. 2016), a strongly lensed galaxy at $z = 6.7$ with an estimated magnification factor of $\mu = 100 \pm 20$. MS0451-H has no confirmed $[\text{CII}]$ detection yet. The upper bound of its $L_{[\text{CII}]}/\text{SFR}$ ratio is more than 1.5 dex below the L11 relation (even with the most conservative, UV-based SFR, see the *left* panel of Fig. 8), showing a strong $[\text{CII}]$ deficit. This appears to be in agreement with the FIRE sample. It can be seen from the figure that the $[\text{CII}]$ deficit of the FIRE galaxies extends to $\text{SFR} \lesssim 10 M_\odot \text{ yr}^{-1}$ at $z \geq 5$, which is even slightly more prominent than at higher SFR. Encouragingly, some of the FIRE galaxies at $z \geq 4$ show similarly low $L_{[\text{CII}]}/\text{SFR}$ ratio as MS0451-H.

The $L_{[\text{CII}]}$ -SFR relation of the observed galaxies at $z \geq 5$ reported in this work seems to have lower normalization than a number of the recent observational studies, including *e.g.* Schaefer et al. (2020) (ALPINE paper), Ferrara et al. (2022) (REBELS paper), Matthee et al. (2017, 2019), Carniani et al. (2018a), Harikane et al. (2020) and Fujimoto et al. (2021). This is due to the fact that these studies have assumed a lower T_{eqv} than what we use for this study as derived using equation (7). As has been mentioned in some of these studies, the largest uncertainty of the derived galaxy $L_{[\text{CII}]}$ -SFR relation at $z \geq 5$ is the assumed T_{eqv} . In Table 5, we explicitly show the difference in the mean T_{eqv} adopted by the ALPINE/REBELS projects and this work (for $\delta_{\text{dzt}} = 0.4$), as well as the resulting difference in the derived mean $L_{[\text{CII}]}/\text{SFR}$ ratio ($\langle L_{[\text{CII}]}/\text{SFR} \rangle$) of the galaxies. Note that Ferrara et al. (2022) has used very similar T_{eqv} compared to what is used in our work as fiducial (with $\delta_{\text{dzt}} = 0.4$), whereas Schaefer et al. (2020) has used significantly lower T_{eqv} ($\langle T_{\text{eqv}} \rangle = 42$ K) for the ALPINE galaxies than us ($\langle T_{\text{eqv}} \rangle = 52.1$ K). Our estimate of the $L_{[\text{CII}]}$ -SFR relation of the ALPINE galaxies is therefore about 0.3 dex below the originally reported result.

$L_{[\text{CII}]}/L_{\text{IR}}$ of IR-luminous galaxies

In addition to the LBGs/LAEs having moderate SFRs, there have been studies probing the more extreme systems at $z \geq 5$, in particular, the quasar hosts. These systems are gas/dust-rich and very IR-luminous ($L_{\text{IR}} \gtrsim 10^{12} L_\odot$). They typically are also bright $[\text{CII}]$ emitters, having $L_{[\text{CII}]}$ that spans across the range of $\approx 10^8 - 10^{10} L_\odot$. We summarize the properties of the quasar hosts at $z \geq 5$ having had $[\text{CII}]$ line detections to date in Table 6 (> 65 galaxies in total). Observations targeting the quasar hosts have a high successful detection rate for $[\text{CII}]$ line (*e.g.* Decarli et al. 2017; Venemans et al. 2020).

Table 4. Properties of the star-forming galaxies at $z \gtrsim 5$ targeted for search for [C_{II}] emission.

Name [†]	z	SFR _{UV} ^{‡, #} ($M_{\odot} \text{ yr}^{-1}$)	S (μJy) ^{‡, ¶, #}	$\log(L_{\text{IR}}/L_{\odot})^{\parallel}$	SFR ^{††} ($M_{\odot} \text{ yr}^{-1}$)	$\log(L_{[\text{CII}]} / L_{\odot})^{\ddagger, \#}$	μ	References *
HZ7	5.253	31.2	< 108 (ALMA 7)	< 11.6	< 62.7	8.74 (ALMA 7)	–	[1, 2, 3]
HZ9	5.541	22.1	516 (ALMA 7)	11.9	174.5	9.21 (ALMA 7)	–	[1, 2, 3]
HZ10	5.657	58.2	1261 (ALMA 7)	12.7	432.8	9.13 (ALMA 7)	–	[1, 2, 3]
NB816-S-61269	5.684	19.9	< 66 (ALMA 7)	< 11.4	< 39.6	8.32 (ALMA 7)	–	[4, 5]
WMH13	5.985	87.1	< 48 (ALMA 6)	< 11.7	< 131.3	8.56 (ALMA 6)	–	[4, 5]
A383-5.1	6.029	3.5	< 2.9 (ALMA 6)	< 10.5	< 6.2	6.95 (ALMA 6)	11.4 ± 1.9	[6]
J1211-0118	6.029	55.2	220 (ALMA 6)	12.4	257.3	9.15 (ALMA 6)	–	[7]
NTTDF2313	6.07	18.4	< 54 (ALMA 6)	< 11.8	< 68.0	< 7.7 (ALMA 6)	–	[8]
WMH5	6.07	63.2	218 (ALMA 6)	12.4	263.5	8.82 (ALMA 6)	–	[9, 10]
RXCJ0600-z6	6.0719	2.8	9.5 (ALMA 6)	11.0	11.5	8.04 (ALMA 6)	21 ± 10	[11]
J0235-0532	6.089	58.4	< 101 (ALMA 6)	< 12.1	< 150.5	8.63 (ALMA 6)	–	[7]
BDF2203	6.12	24.2	< 69 (ALMA 6)	< 11.9	< 87.6	8.1 (ALMA 6)	–	[8]
CLM1	6.166	56.0	40 (ALMA 6)	11.7	92.9	8.33 (ALMA 6)	1.13	[4, 9]
J0217-0208	6.203	86.6	239 (ALMA 6)	12.4	307.3	9.15 (ALMA 6)	–	[7]
MACS0308-zD1	6.2078	3.2	< 27 (ALMA 6)	< 11.5	< 33.7	7.47 (ALMA 6)	22	[12,13]
GOODS3203	6.27	27.2	< 123 (ALMA 6)	< 12.2	< 140.4	< 8.1 (ALMA 6)	–	[8]
NIRCam 12053	6.3254	34	66.0 (ALMA 6)	11.9	92.0	8.84 (ALMA 6)	1.97	[14]
COSMOS20521	6.36	20.2	< 60 (ALMA 6)	< 11.8	< 75.5	< 7.7 (ALMA 6)	–	[8]
VR7	6.529	58.2	< 31.8 (ALMA 6)	< 11.6	< 87.5	8.68 (ALMA 6)	–	[15]
MASOSA	6.543	13.0	< 27.6 (ALMA 6)	< 11.5	< 35.5	< 7.34 (ALMA 6)	–	[15]
HCM6A	6.56	5.9	< 680 (PdBI)	< 12.9	< 631.1	< 7.81 (PdBI)	4.5	[16, 17]
UDS4812	6.561	19.3	< 72 (ALMA 6)	< 11.9	< 85.7	< 7.8 (ALMA 6)	–	[8]
Himiko	6.591	19.8	< 27 (ALMA 6)	< 11.5	< 44.8	8.08 (ALMA 6)	–	[18, 19]
CR7	6.600	41.7	< 21 (ALMA 6)	< 11.4	< 61.1	8.34 (ALMA 6)	–	[20, 21]
COSMOS24108	6.629	25.6	< 54 (ALMA 6)	< 11.8	< 68.2	8.04 (ALMA 6)	–	[22]
UDS16291	6.638	13.4	< 60 (ALMA 6)	< 11.8	< 65.4	7.85 (ALMA 6)	–	[22]
NTTDF6345	6.701	21.2	< 48 (ALMA 6)	< 11.7	< 60.2	8.26 (ALMA 6)	–	[22]
MS0451-H	6.703	0.4	< 0.33 (ALMA 6)	< 9.6	< 0.7	< 5.48 (ALMA 6)	100 ± 20	[6]
UVISTA-Z-007	6.7496	23.7	< 52.2 (ALMA 6)	< 11.8	< 72.0	8.75 (ALMA 6)	–	[23, 24]
UVISTA-Z-019	6.7534	15.8	66 (ALMA 6)	11.9	74.1	8.94 (ALMA 6)	–	[23, 24]
RXJ1347-1216	6.766	2.4	< 45 (ALMA 6)	< 11.7	< 44.8	7.18 (ALMA 6)	5.0 ± 0.3	[25]
COS-2987030247	6.808	24.6	< 75 (ALMA 6)	< 11.9	< 94.3	8.56 (ALMA 6)	–	[26]
A1703-zD1	6.827	10.1	< 24.5 (NOEMA)	< 11.5	< 32.8	7.54 (NOEMA)	9.0 ± 2.7	[27]
SDF-46975	6.844	15.4	< 57.6 (ALMA 6)	< 11.8	< 68.7	< 7.75 (ALMA 6)	–	[28]
COS-3018555981	6.854	20.8	< 87 (ALMA 6)	< 12.0	< 101.3	8.67 (ALMA 6)	–	[26]
UVISTA-Z-009	6.86	16.9	< 38.0 (ALMA 6)	< 11.6	< 52.1	< 8.12 (ALMA 6)	≤ 1.5	[23, 24]
IOK-1	6.965	20.0	< 63 (ALMA 6)	< 11.9	< 78.4	< 7.53 (ALMA 6)	–	[29]
BDF-512	7.008	6.0	< 55.2 (ALMA 6)	< 11.8	< 54.2	< 7.78 (ALMA 6)	–	[28]
UVISTA-Z-013	7.02	22.1	< 45.0 (ALMA 6)	< 11.7	< 63.8	< 8.30 (ALMA 6)	–	[23, 24]
UVISTA-Z-001	7.0599	45.8	104 (ALMA 6)	12.1	137.8	8.83 (ALMA 6)	–	[23, 24]
UVISTA-Z-010	7.06	17.4	< 44.1 (ALMA 6)	< 11.7	< 58.3	< 8.30 (ALMA 6)	–	[23, 24]
BDF-3299	7.109	5.7	< 23.4 (ALMA 6)	< 11.4	< 27.4	7.83 (ALMA 6)	–	[28, 30, 31]
A1689-zD1	7.137	4.7	60.2 (ALMA 6)	11.9	67.5	7.87 (ALMA 6)	9.3	[32, 33, 34]
COSMOS13679	7.145	21.1	< 42 (ALMA 6)	< 11.7	< 60.1	7.85 (ALMA 6)	–	[22]
B14-65666	7.152	50.2	130 (ALMA 6)	12.2	170.2	9.12 (ALMA 6)	–	[35, 36]
SXDF-NB1006-2	7.212	21.6	< 42 (ALMA 6)	< 11.7	< 60.6	< 7.45 (ALMA 6)	–	[37]
z8-GND-5296	7.508	16.6	< 480 (PdBI)	< 12.7	< 464.1	< 8.55 (PdBI)	–	[38, 39]
MACS0416-Y1	8.311	11.7	137 (ALMA 7)	11.8	56.8	8.15 (ALMA 5)	1.43 ± 0.04	[40, 41, 42]
A2744-YD4	8.380	11.2	99 (ALMA 7)	11.6	43.8	7.26 (ALMA 5)	1.8 ± 0.3	[31, 43, 44]
S04590	8.4931	0.5	< 4.81 (ALMA 7)	< 10.3	< 2.0	7.22 (ALMA 5)	8.69 ± 2.5	[45, 46]
MACS1149-JD1	9.110	4.5	< 5.3 (ALMA 7)	< 10.4	< 6.5	7.08 (ALMA 5)	10	[31, 44, 47]
REBELS ^{‡‡}								
REBELS-05	6.496	15.1	67.2 (ALMA 6)	11.9	77.2	8.84 (ALMA 6)	–	[48, 49, 50]
REBELS-38	6.577	19.5	163.0 (ALMA 6)	12.3	170.2	9.23 (ALMA 6)	–	[48, 49, 50]
REBELS-29	6.685	27.0	56.1 (ALMA 6)	11.8	78.9	8.74 (ALMA 6)	–	[48, 49, 50]
REBELS-32	6.729	15.1	60.4 (ALMA 6)	11.8	71.0	8.89 (ALMA 6)	–	[48, 49, 50]
REBELS-08	6.749	17.3	101.4 (ALMA 6)	12.1	111.2	8.87 (ALMA 6)	–	[48, 49, 50]
REBELS-39	6.847	40.0	79.6 (ALMA 6)	12.0	113.7	8.90 (ALMA 6)	–	[48, 49, 50]
REBELS-14	7.084	37.9	60.0 (ALMA 6)	11.8	93.6	8.57 (ALMA 6)	–	[48, 49, 50]
REBELS-27	7.090	21.6	50.6 (ALMA 6)	11.8	68.5	8.79 (ALMA 6)	–	[48, 49, 50]

(Continue on next page)

Table 4 – *continued*

Name [†]	z	SFR _{UV} ^{§, #} ($M_{\odot} \text{ yr}^{-1}$)	S (μJy) ^{¶, #}	$\log(L_{\text{IR}}/L_{\odot})^{\parallel}$	SFR ^{††} ($M_{\odot} \text{ yr}^{-1}$)	$\log(L_{[\text{CII}]} / L_{\odot})^{\#}$	μ	References *
REBELS-25	7.306	16.2	56.1 (ALMA 6)	11.8	68.3	9.20 (ALMA 6)	–	[48, 49, 50]
REBELS-12	7.349	32.5	86.8 (ALMA 6)	12.0	113.2	9.00 (ALMA 6)	–	[48, 49, 50]
REBELS-40	7.365	18.4	48.3 (ALMA 6)	11.8	64.5	8.69 (ALMA 6)	–	[48, 49, 50]
REBELS-19	7.369	15.1	71.2 (ALMA 6)	11.9	81.3	8.94 (ALMA 6)	–	[48, 49, 50]
REBELS-18	7.675	33.5	52.9 (ALMA 6)	11.8	82.8	9.03 (ALMA 6)	–	[48, 49, 50]

[†] The table does not include the 118 galaxies ($4.5 \lesssim z \lesssim 6$) selected by the ALPINE project. The information of the ALPINE galaxies can be downloaded from the official webpage of the project: https://cesam.lam.fr/a2c2s/data_release.php. The ALPINE galaxies are unlensed.

[§] SFR_{UV} is converted from L_{UV} via $\text{SFR}_{\text{UV}} (M_{\odot} \text{ yr}^{-1}) = 1.58 \times 10^{-10} L_{\text{UV}} (L_{\odot})$ following [Hao et al. \(2011\)](#) (see Table 3) for the [Kroupa \(2002\)](#) IMF.

[¶] The number in the brackets indicates the specific ALMA band at which dust continuum is measured.

^{¶¶} For the galaxies having no detection of dust thermal continuum ([CII] emission), we show the 3σ upper confidence limit of S ($L_{[\text{CII}]}$).

[#] For the gravitationally-lensed galaxies, L_{UV} (and hence SFR_{UV}), S , L_{IR} and $L_{[\text{CII}]}$ are de-magnified by μ .

^{||} L_{IR} (or the upper limit of L_{IR} for the dust-undetected sources) is converted from S (the 3σ upper limit of S) via the standard MBB function with T_{eqv} calculated by equation (4) (assuming $\beta_{\text{dust}} = 2.0$ and $\delta_{\text{dzt}} = 0.4$).

^{††} SFR is derived using $\text{SFR} (M_{\odot} \text{ yr}^{-1}) = \text{SFR}_{\text{UV}} + \text{SFR}_{\text{IR}} = 1.58 \times 10^{-10} (L_{\text{UV}} + 0.46L_{\text{IR}}) (L_{\odot})$ following [Hao et al. \(2011\)](#) (see Table 3) for the [Kroupa \(2002\)](#) IMF.

^{‡‡} We only list here the 13 galaxies of the REBELS sample that have confirmed detection of both [CII] and dust continuum. The information of the other 5 galaxies having [CII] but no dust detection is not yet publicly available.

* References: [1]: [Capak et al. \(2015\)](#), [2]: [Barisic et al. \(2017\)](#), [3]: [Faisst et al. \(2017\)](#), [4]: [Fujimoto et al. \(2019\)](#), [5]: [Fujimoto et al. \(2016\)](#), [6]: [Knudsen et al. \(2016\)](#), [7]: [Harikane et al. \(2020\)](#), [8]: [Carniani et al. \(2018a\)](#), [9]: [Willott et al. \(2015b\)](#), [10]: [Willott et al. \(2013a\)](#), [11]: [Fujimoto et al. \(2021\)](#), [12]: [Welch et al. \(2023\)](#), [13]: [Fudamoto et al. \(2023a\)](#), [14]: [Fujimoto et al. \(2023\)](#), [15]: [Matthee et al. \(2019\)](#), [16]: [Kanevar et al. \(2013\)](#), [17]: [Hu et al. \(2002\)](#), [18]: [Ouchi et al. \(2013\)](#), [19]: [Carniani et al. \(2018b\)](#), [20]: [Sobral et al. \(2015\)](#), [21]: [Matthee et al. \(2017\)](#), [22]: [Pentericci et al. \(2016\)](#), [23]: [Schouws et al. \(2023\)](#), [24]: [Schouws et al. \(2022\)](#), [25]: [Bradač et al. \(2017\)](#), [26]: [Smit et al. \(2018\)](#), [27]: [Molyneux et al. \(2022\)](#), [28]: [Maiolino et al. \(2015\)](#), [29]: [Ota et al. \(2014\)](#), [30]: [Carniani et al. \(2017\)](#), [31]: [Carniani et al. \(2020\)](#), [32]: [Watson et al. \(2015\)](#), [33]: [Knudsen et al. \(2017\)](#), [34]: [Wong et al. \(2022\)](#), [35]: [Hashimoto et al. \(2019a\)](#), [36]: [Bowler et al. \(2018\)](#), [37]: [Inoue et al. \(2016\)](#), [38]: [Schaerer et al. \(2015a\)](#), [39]: [Finkelstein et al. \(2013\)](#), [40]: [Tamura et al. \(2019\)](#), [41]: [Bakx et al. \(2020\)](#), [42]: [Kawamata et al. \(2016\)](#), [43]: [Laporte et al. \(2017\)](#), [44]: [Laporte et al. \(2019\)](#), [45]: [Fujimoto et al. \(2022\)](#), [46]: [Heintz et al. \(2023b\)](#), [47]: [Hashimoto et al. \(2018\)](#), [48]: [Ferrara et al. \(2022\)](#), [49]: [Sommovigo et al. \(2022\)](#), [50]: [Bouwens et al. \(2022\)](#).

Table 5. Comparison between the mean ‘equivalent dust temperature’ ($\langle T_{\text{eqv}} \rangle$) assumed by the ALPINE and REBELS projects and by this work.

Project name	Reference	No. of galaxies	$\langle z \rangle$	$\langle T_{\text{eqv}} / \text{K} \rangle$ (literature)	$\langle T_{\text{eqv}} / \text{K} \rangle^{\dagger}$ (this work)	$\Delta \langle \log(\frac{L_{[\text{CII}]}}{\text{SFR}}) \rangle^{\ddagger}$ (dex)
ALPINE	Schaerer et al. (2020)	118	4.58	42	47.9	-0.21
REBELS	Ferrara et al. (2022)	40	7.08	55	57.4	-0.12

[†] Calculated using equation (7) with $\delta_{\text{dzt}} = 0.4$. Note that with a lower δ_{dzt} , T_{eqv} is higher than the listed value in this column.

[‡] The resulting difference in the derived mean $L_{[\text{CII}]} / \text{SFR}$ ratio (in dex) of the galaxy samples due to the difference in T_{eqv} used by the previous studies ([Schaerer et al. 2020](#) and [Ferrara et al. 2019](#)) and this work.

Like most of the LBGs/LAEs at this epoch, the selected quasar hosts typically have one or two data points in their dust continuum (measured with ALMA band 6 or 7) and their L_{IR} is converted from a single broad-band sub-mm flux density in the literature using the standard MBB function with an assumed T_{eqv} . L_{IR} has generally been considered as a crude estimate of their SFR by the observational studies assuming that these quasar hosts are gas and dust-rich and the stellar radiation of these galaxies is significantly dust-obscured. It is, however, unknown to what degree the radiation from the accreting supermassive black hole affects the shape of the IR SED and the total IR luminosity of these early galaxies. Observations of galaxies at lower redshifts ($z \approx 0 - 3$) demonstrate that the IR SED shape of galaxies becomes ‘warmer’ (indicating higher T_{eqv}) with increasing AGN power ([Kirkpatrick et al. 2015](#)). A similar conclusion was reached in the early study by [Younger et al. \(2009\)](#) with hydrodynamic simulations of galaxy mergers that include AGN modelling. Note,

however, that some recent studies (*e.g.* [Symeonidis 2016](#); [McKinney et al. 2021b](#)) also suggest that AGN radiation may even dominate the cold-dust emission of the host galaxies at high redshifts.

In Fig. 9, we show the $L_{[\text{CII}]} / L_{\text{IR}}$ vs. L_{IR} relation of the quasar hosts, along with other galaxy populations at $z \gtrsim 5$, including the few SMGs (listed in Table 3), the ALPINE and REBELS galaxies and other rest-UV-selected galaxies at $z \gtrsim 5$ (we only show the galaxies having confirmed dust detection, which have more reliable constraints on L_{IR} than the dust-undetected galaxies). We convert the reported single-band sub-mm flux density of all the quasar hosts to L_{IR} using the standard MBB function and T_{eqv} that follows equation (7) with the best-fit parameters derived by [Liang et al. \(2019\)](#). We note that for the quasar hosts, this is likely to be an underestimate because the best-fit parameters of [Liang et al. \(2019\)](#) are derived using FIRE simulations which do not include AGN feedback. Having a higher T_{eqv} , the data points of the quasar hosts (black stars) will shift in

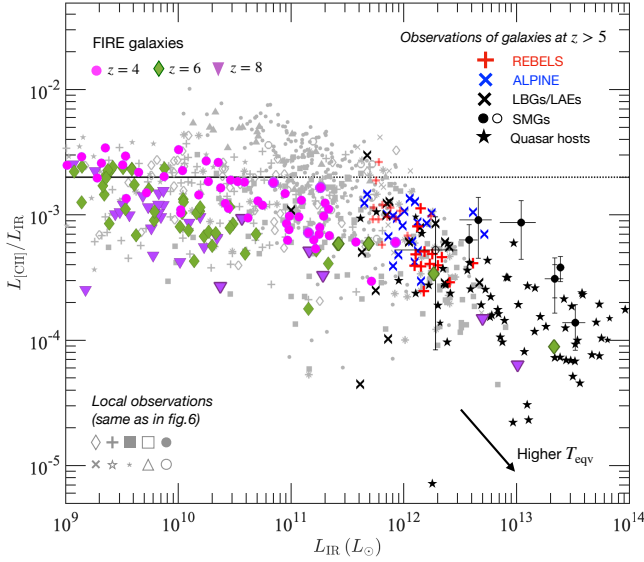


Figure 9. $L_{[\text{CII}]} / L_{\text{IR}}$ vs. L_{IR} relation of galaxies at high redshifts. Filled coloured symbols indicate the data of the FIRE galaxies (magenta circles for $z = 4$, green diamonds for $z = 6$ and purple downward triangles for $z = 8$). Red crosses and blue ‘X’ represent the observational data of the REBELS ($\langle z \rangle \approx 7$) and ALPINE ($\langle z \rangle \approx 4.5$) galaxy samples, respectively. Black symbols represent the observational data of the other galaxy samples at $z \geq 5$. Specifically, black ‘X’s, black circles (filled and unfilled) and black stars correspond to the UV-selected galaxies, SMGs and quasar hosts, respectively. For the galaxies whose dust continuum is measured at only single ALMA band, L_{IR} is derived using T_{eqv} that follows equation (7) assuming $\delta_{\text{dzt}} = 0.4$ except for the REBELS galaxies, for which we show two different sets of data that are produced by using $\delta_{\text{dzt}} = 0.4$ (semi-transparent red crosses) and $\delta_{\text{dzt}} = 0.1$ (non-transparent red crosses). The lower δ_{dzt} yields higher T_{eqv} (and hence L_{IR}) estimates for the galaxies. The black arrow indicates the direction along which the data points of these galaxies move on the diagram with increasing T_{eqv} . For the SMGs, filled circles indicate the galaxies that are either confirmed as un-lensed or have observationally determined lensing magnification factor μ , whereas unfilled circles indicate the lensed SPT galaxies having no determined μ yet (see Section 4.2). Grey symbols in the background represent the observational data of the local $z = 0$ galaxy samples, as is shown in Fig. 6 (right panel). Black horizontal line indicates the median $L_{[\text{CII}]} / L_{\text{IR}}$ ratio ($\langle L_{[\text{CII}]} / L_{\text{IR}} \rangle = 0.002$) of the local galaxies at $L_{\text{IR}} < 10^{11} L_{\odot}$. **Galaxies at $z > 5$ show a trend of declining $L_{[\text{CII}]} / L_{\text{IR}}$ ratio with L_{IR} at $L_{\text{IR}} \gtrsim 10^{11} L_{\odot}$ similar to the local samples. The FIRE simulations successfully reproduced the observed $[\text{CII}]$ deficit at high L_{IR} at $z > 5$.**

the diagonal direction toward the bottom-right corner of the diagram (marked by the black arrow in Fig. 9).

Looking at the observational data, we can see a clear trend of declining $L_{[\text{CII}]} / L_{\text{IR}}$ ($\sim L_{[\text{CII}]} / \text{SFR}$) ratio of the galaxies with L_{IR} ($[\text{CII}]$ deficit) at $L_{\text{IR}} \gtrsim 10^{11.5} L_{\odot}$ at $z \geq 5$, similar to the trend seen at lower redshifts. The $L_{[\text{CII}]} / L_{\text{IR}} - L_{\text{IR}}$ relation of these early galaxies appears to consistent with the local samples (grey symbols) in the overlapping L_{IR} regime and show similarly large scatter.

We also show in Fig. 9 the $L_{[\text{CII}]} / L_{\text{IR}} - L_{\text{IR}}$ relation of the FIRE galaxies at $z = 4 - 8$. The result of the FIRE galaxies is in good agreement with the observational data in overlapping L_{IR} range, except for the REBELS sample ($\langle z \rangle \approx 7$, indicated by red ‘X’s in Fig. 9). Using $\delta_{\text{dzt}} = 0.4$, the REBELS galaxies (semi-transparent red crosses) show systematically higher $L_{[\text{CII}]} / L_{\text{IR}}$ than the rest of the observed galaxy samples (blue and black ‘X’s) as well as the FIRE galaxies at similar L_{IR} ($\approx 10^{12} L_{\odot}$) by ~ 0.5 dex. Using $\delta_{\text{dzt}} = 0.1$

instead, the expected mean T_{eqv} of the REBELS sample increases by $\approx 20\%$ (from 57 K to 71 K), and the derived mean L_{IR} ($L_{[\text{CII}]} / L_{\text{IR}}$ ratio) of the galaxies increases (decreases) by a factor of ~ 3 . The data of the REBELS sample for $\delta_{\text{dzt}} = 0.1$ (non-transparent red crosses) appears to be consistent with the other observed samples as well as the FIRE galaxies.

The FIRE galaxies at $z \geq 4$ show a trend of declining $L_{[\text{CII}]} / L_{\text{IR}}$ ratio with L_{IR} , which agrees with the observational data. It is also clear to see that the $L_{[\text{CII}]} / L_{\text{IR}}$ ratio of the FIRE galaxies decreases with redshift at fixed L_{IR} at $z \geq 4$. The trend of decreasing $L_{[\text{CII}]} / L_{\text{IR}}$ ratio with both redshift and L_{IR} persists up to $z = 8$ in the FIRE simulations.

Finally, we note that it is unclear whether AGN activity is directly related to the $[\text{CII}]$ deficit at high L_{IR} based on the current data, despite the large number of quasar hosts at $z \geq 5$ showing strong $[\text{CII}]$ deficit. This is because most of the selected SMGs in the literature ($2 \lesssim z \lesssim 7$), having similar L_{IR} to the quasar hosts, have no identified AGN feature (see Table 3) but show similarly strong $[\text{CII}]$ deficit as the quasar hosts. In addition, the FIRE simulations, which do not include AGN physics, have also successfully reproduced similarly low $L_{[\text{CII}]} / L_{\text{IR}}$ ratio at high L_{IR} .

5 THE PHYSICS OF THE $L_{[\text{CII}]} - \text{SFR}$ SCALING RELATION OF GALAXIES

In the previous section, we have shown that the $L_{[\text{CII}]} - \text{SFR}$ relation of the FIRE galaxies predicted using our model is in good agreement with the observational data of local and high- z galaxies. In particular, our model reproduces the observed $[\text{CII}]$ deficit of galaxies at high L_{IR} and high redshifts. In this section, we explore the origin(s) of the $[\text{CII}]$ deficit of galaxies using the FIRE galaxy sample.

In Section 5.1, we present the analytic solution of $[\text{CII}]$ line flux emerging from a plane-parallel gas slab. The toy model provides useful insights for understanding the $[\text{CII}]$ emission of galaxies. In Section 5.2, we derive an important scaling relation of galaxies between their $L_{[\text{CII}]} / \text{SFR}$ ratio and other physical properties. Based on this scaling relation, we investigate the cause of the $[\text{CII}]$ deficit of galaxies in Section 5.3. Finally, in Section 5.4, we show the presence of two distinct physical regimes where the main reason for the $[\text{CII}]$ deficit of galaxies is different.

5.1 Insights from the plane parallel slab model

The $[\text{CII}]$ line flux emerging from a plane-parallel slab that is irradiated by an external radiation field has recently been studied by Ferrara et al. (2019, hereafter F19). In this section, we summarize the key points of the F19 model. We refer interested readers to F19 for the details.

The plane-parallel slab can be characterized by three distinct zones based on the ionization structures of gas, as has been discussed in Section 3.1. Right beneath the surface of the slab, ionizing radiation ($E_{\gamma} > 13.6$ eV) creates a H^+ region extending to a gas column density N_s (Zone I), where both hydrogen and carbon are ionized. Beyond N_s , hydrogen becomes neutral but LW ($11.2 < E_{\gamma} < 13.6$ eV) photons maintain carbon in the singly ionized state (Zone II). The LW photons become fully absorbed by dust and H_2 at a column density N_F , beyond which hydrogen turns into H_2 and carbon becomes neutral (Zone III). We have shown in Fig. 2 the ionization structures of a plane-parallel slab calculated by CLOUDY as an example (see also Fig. 1 of F19 for a schematic plot).

N_s can be estimated by equating the photo-ionization rate to the

Table 6. Characteristics of the high- z quasar host galaxies.

Name	z	S_{ν} (mJy)	$\log(L_{\text{IR}}/L_{\odot})^{\S}$	$\log(L_{[\text{CII}]} / L_{\odot})^{\text{ }}$	References*
SDSS J1015+0020	4.407	0.60 (ALMA 7)	12.3	8.46 (ALMA 7)	[1]
BRI 1335-0417	4.41	9.03 (ALMA 6)	14.0	10.21 (APEX/FLASH)	[2, 3]
BR 1202-0725 N	4.691	18.8 (ALMA 7)	13.8	10.00 (ALMA 7)	[4, 5]
BR 1202-0725 S	4.694	18.0 (ALMA 7)	13.8	9.81 (ALMA 7)	[4, 5]
SDSS J0338+0021	5.027	2.98 (ALMA 6)	13.5	9.76 (ALMA 6)	[6]
SDSS J0129-0035	5.779	2.61 (ALMA 6)	13.5	9.28 (ALMA 6)	[7, 8, 9]
SDSS J1044-0125	5.785	3.00 (ALMA 6)	13.5	9.21 (ALMA 6)	[7, 8, 9]
PSO J004+17	5.817	0.88 (ALMA 6)	13.0	8.31 (ALMA 6)	[10]
PSO J352-15	5.832	0.34 (ALMA 7)	12.1	9.09 (ALMA 7)	[11]
HSC J1202-0057	5.929	0.25 (ALMA 6)	12.4	8.79 (ALMA 7)	[12]
PSO J056+16	5.967	0.17 (ALMA 6)	12.3	7.11 (ALMA 6)	[10]
PSO J007+04	6.001	2.07 (ALMA 6)	13.4	9.20 (ALMA 6)	[9, 13]
SDSS J2310+1855 [†]	6.003	–	13.2	9.94 (ALMA 6)	[7, 14]
PSO J009-10	6.004	3.66 (ALMA 6)	13.6	9.95 (ALMA 6)	[9, 13]
CFHQS J0055+0146	6.006	0.21 (ALMA 6)	12.4	8.92 (ALMA 6)	[15]
CFHQS J0216-0455	6.01	< 0.04 (ALMA 6)	< 11.6	< 7.85 (ALMA 6)	[16]
PSO J265+41	6.026	3.61 (ALMA 6)	13.6	9.96 (ALMA 6)	[10]
SDSS J1306+0356	6.033	0.74 (ALMA 6)	12.9	9.05 (ALMA 6)	[9, 13]
ULAS J1207+0630	6.037	0.50 (ALMA 6)	12.7	9.13 (ALMA 6)	[13]
SDSS J2054-0005	6.039	3.15 (ALMA 6)	13.5	9.49 (ALMA 6)	[7, 9]
VDESJ0454-4448	6.058	0.71 (ALMA 6)	12.9	8.86 (ALMA 6)	[13]
PSO J158+14	6.068	3.46 (ALMA 6)	13.6	9.22 (ALMA 6)	[10]
SDSS J0842+1218	6.075	0.68 (ALMA 6)	12.9	8.88 (ALMA 6)	[9, 13, 17]
HSC J2228+0152	6.081	< 0.05 (ALMA 6)	< 11.7	8.39 (ALMA 6)	[18]
CFHQS J2100-1715	6.081	0.56 (ALMA 6)	12.8	9.12 (ALMA 6)	[9, 13, 17, 19]
HSC J2216-0016	6.096	0.14 (ALMA 6)	12.2	9.01 (ALMA 6)	[12]
PSO J239+07	6.110	0.23 (ALMA 6)	12.4	8.37 (ALMA 6)	[10]
HSC J1208-0200	6.117	0.09 (ALMA 6)	12.0	8.43 (ALMA 6)	[18]
CFHQS J1509-1749	6.123	1.72 (ALMA 6)	13.3	9.37 (ALMA 6)	[13]
PSO J065-19	6.125	0.46 (ALMA 6)	12.7	8.97 (ALMA 6)	[13]
CFHQS J0221-0802	6.13	0.25 (ALMA 6)	12.4	< 8.08 (ALMA 6)	[16]
ULAS J1319+0950	6.135	5.13 (ALMA 6)	13.8	9.61 (ALMA 6)	[7, 9, 20]
VIK J2318-3029	6.146	3.11 (ALMA 6)	13.5	9.35 (ALMA 6)	[9, 13]
VIMOS2911	6.149	0.77 (ALMA 6)	12.9	9.41 (ALMA 6)	[16]
PSO J217-16	6.150	0.37 (ALMA 6)	12.6	9.00 (ALMA 6)	[13]
CFHQS J2229+1457	6.152	0.05 (ALMA 6)	11.8	8.78 (ALMA 6)	[15]
PSO J359-06	6.172	0.79 (ALMA 6)	12.9	9.42 (ALMA 6)	[9, 10, 13]
PSO J065-26	6.187	1.37 (ALMA 6)	13.2	9.23 (ALMA 6)	[9, 13]
PSO J308-21	6.236	1.18 (ALMA 6)	13.1	9.53 (ALMA 6)	[9, 13, 17]
HSC J2239+0207	6.250	1.11 (ALMA 6)	13.1	8.98 (ALMA 6)	[18]
SDSS J0100+2802	6.327	1.37 (ALMA 6)	13.2	9.58 (ALMA 6)	[21, 22]
ATLAS J025-33	6.338	2.49 (ALMA 6)	13.4	9.75 (ALMA 6)	[9, 13]
VIK J2211-3206	6.339	0.57 (ALMA 6)	12.8	8.98 (ALMA 6)	[13]
PSO J083+11	6.340	5.10 (ALMA 6)	13.8	10.02 (ALMA 6)	[23]
VIK J1152+0055	6.364	0.22 (ALMA 6)	12.4	8.81 (ALMA 6)	[12, 13]
PSO J159-02	6.381	0.65 (ALMA 6)	12.9	9.05 (ALMA 6)	[13]
HSC J0859+0022	6.390	0.16 (ALMA 6)	12.2	8.66 (ALMA 6)	[12]
J2329-0301	6.417	0.04 (ALMA 6)	11.6	8.59 (ALMA 6)	[16]
SDSS J1148+5251 [†]	6.42	–	13.3	9.64 (NOEMA)	[22, 24, 25, 26]
CFHQS J0210-0456	6.432	0.12 (ALMA 6)	12.1	8.48 (ALMA 6)	[27]
PSO J183+05	6.439	4.79 (ALMA 6)	13.7	9.85 (ALMA 6)	[9, 13]
VIK J2318-3113	6.443	0.36 (ALMA 6)	12.6	9.20 (ALMA 6)	[9, 13]
PSO J011+09	6.469	1.20 (ALMA 6)	13.1	8.47 (ALMA 6)	[10]
PSO J167-13	6.514	0.89 (ALMA 6)	13.0	9.75 (ALMA 6)	[9, 13, 16]
J043947+163415 (lensed [‡])	6.519	3.27 (ALMA 6)	13.6	9.54 (ALMA 6)	[28, 29]
PSO J036+03	6.542	2.55 (ALMA 6)	13.5	9.53 (ALMA 6)	[9, 30]
PSO J231-20	6.587	4.37 (ALMA 6)	13.7	9.55 (ALMA 6)	[9, 13, 17]
PSO J323+12	6.587	0.23 (ALMA 6)	12.4	9.16 (ALMA 6)	[9, 31]
PSO J006+39	6.610	0.55 (NOEMA)	12.8	8.95 (NOEMA)	[32]
VIK J030516-315056	6.614	5.34 (ALMA 6)	13.8	9.77 (ALMA 6)	[9, 32, 33]
PSO J338+29	6.658	0.97 (NOEMA)	13.0	9.30 (NOEMA)	[31]
VIK J1048-0109	6.676	2.84 (ALMA 6)	13.5	9.32 (ALMA 6)	[9, 13]

(Continue on next page)

Table 6 – continued

Name	z	S_ν (mJy)	$\log(L_{\text{IR}}/L_\odot)^\S$	$\log(L_{[\text{CII}]} / L_\odot)$	References*
HSC J1205-0000	6.723	1.17 (ALMA 6)	13.1	8.58 (ALMA 6)	[34]
VIK J0109-3047	6.791	0.52 (ALMA 6)	12.8	9.38 (ALMA 6)	[9, 33]
VIK J2348-3054	6.901	2.28 (ALMA 6)	13.4	9.25 (ALMA 6)	[9, 33]
HSC J1243+0100	7.075	1.52 (ALMA 6)	13.2	9.40 (ALMA 6)	[35]
ULAS J1120+0641	7.085	0.64 (ALMA 6)	12.9	9.08 (ALMA 6)	[9, 36]
ULAS J1342+0928	7.541	0.34 (ALMA 6)	12.6	9.12 (ALMA 6)	[9, 37]

[†] L_{IR} of SDSS J2310+1855 and SDSS J1148+5251 are derived by SED fitting (e.g. Casey 2012; Casey et al. 2014) to multiple data points at both Wien and Rayleigh-Jeans sides of the dust IR SED.

[‡] J043947+163415 has been confirmed to be gravitationally-lensed, and its luminosities have been de-magnified by $\mu = 4.6 \pm 2.0$, estimated based on the lensing configuration from HST imaging by Fan et al. (2019).

^{||} NOEMA: Northern Extended Millimeter Array

(Website: <https://www.iram-institute.org/EN/content-page-235-3-235-0-0-0.html>).

[§] L_{IR} (or its upper 3σ limit) is converted from S (its 3σ upper limit) using the standard MBB function and with T_{eq} that follows equation (7) (assuming $\beta_{\text{dust}} = 2.0$ and $\delta_{\text{dgr}} = 0.4$), except for SDSS J2310+1855 and SDSS J1148+5251.

* References: [1]: Bischetti et al. (2018), [2]: Wagg et al. (2010), [3]: Lu et al. (2018), [4]: Wagg et al. (2012), [5]: Iono et al. (2006), [6]: Leipski et al. (2014), [7]: Wang et al. (2013), [8]: Wang et al. (2019), [9]: Venemans et al. (2020), [10]: Eilers et al. (2020), [11]: Rojas-Ruiz et al. (2021), [12]: Izumi et al. (2018), [13]: Decarli et al. (2018), [14]: Shao et al. (2019), [15]: Willott et al. (2015a), [16]: Willott et al. (2017), [17]: Decarli et al. (2017), [18]: Izumi et al. (2019), [19]: Walter et al. (2018), [20]: Shao et al. (2017), [21]: Wang et al. (2016), [22]: Leipski et al. (2013), [23]: Andika et al. (2020), [24]: Walter et al. (2009), [25]: Maiolino et al. (2005), [26]: Meyer et al. (2022), [27]: Willott et al. (2013b), [28]: Yang et al. (2019b), [29]: Yue et al. (2021), [30]: Bañados et al. (2015), [31]: Mazzucchelli et al. (2017), [32]: Venemans et al. (2019) [33]: Venemans et al. (2016), [34]: Izumi et al. (2021a), [35]: Izumi et al. (2021b), [36]: Venemans et al. (2012), [37]: Venemans et al. (2017).

recombination rate of hydrogen inside the H⁺ region (Zone I) assuming that dust extinction is negligible, which can be expressed as (see Appendix C for the details)

$$N_s = n_{\text{H}} l_s = \frac{Uc}{\alpha_{\text{B}}} \approx 10^{23} U \text{ cm}^{-2}, \quad (8)$$

where l_s is the distance from the surface of the slab to the end of Zone I, U parameter represents the ionizing photon-to-gas density ratio, i.e.

$$U = \frac{n_\gamma}{n_{\text{H}}}, \quad (9)$$

c represents the speed of light, and $\alpha_{\text{B}} = 2.6 \times 10^{-13} \text{ cm}^3 \text{ s}^{-1}$ is the Case-B recombination coefficient at gas temperature $T \approx 10^4 \text{ K}$ (Ferland et al. 1992). For a slab with density $n_{\text{H}} = 50 \text{ cm}^{-3}$ that is exposed to a radiation field having $G = 200 G_\odot$, we obtain $U = n_\gamma/n_{\text{H}} \approx 1.3 \times 10^{-3}$ at and near the surface of the slab. Using equation (8), we obtain $N_s \approx 1.3 \times 10^{20} \text{ cm}^{-2}$. We can see from Fig. 2 that this estimated N_s is in good agreement with the result computed by CLOUDY, in particular, for the metal-poor model (with $Z_{\text{gas}} = 0.1 Z_\odot$; right panels of Fig. 2), where dust extinction in the H⁺ (Zone I) region is negligible. N_s of the metal-rich model (with $Z_{\text{gas}} = Z_\odot$; left panels of Fig. 2) is smaller by about 1/4 due to higher absorption of ionizing photons by dust.

N_{F} can be estimated using

$$N_{\text{F}} = n_{\text{H}} l_{\text{F}} = \bar{\sigma}_{\text{d}}^{-1} \ln(1 + 10^5 \omega U), \quad (10)$$

which is obtained by performing a RT calculation (Sternberg et al. 2014) that accounts for the absorption of LW photons by dust grains and H₂ as light propagates through the slab. In equation (10), l_{F} represents the distance between the surface of the slab and the end of Zone II,

$$\bar{\sigma}_{\text{d}} = 5.9 \times 10^{-22} \left(\frac{\delta_{\text{dgr}}}{\delta_{\text{dgr, MW}}} \right) \text{ cm}^2 \quad (11)$$

represents the flux-weighted dust extinction cross section per H-atom,

and

$$\omega = \frac{1}{1 + 0.9(\delta_{\text{dgr}}/\delta_{\text{dgr, MW}})^{1/2}}, \quad (12)$$

where $\delta_{\text{dgr, MW}} = 10^{-2}$ represents the Galactic dust-to-gas ratio (see e.g. Gilmore et al. 1989; Sodroski et al. 1997; Zubko et al. 2004; Rémy-Ruyer et al. 2014; McKinnon et al. 2016; Li et al. 2019). For the two models where $Z_{\text{gas}} = Z_\odot$ and $Z_{\text{gas}} = 0.1 Z_\odot$, N_{F} is expected to be $\sim 10^{21} \text{ cm}^{-2}$ and $\sim 10^{22} \text{ cm}^{-2}$ (according to equation 10), respectively. This result is again in good agreement with the prediction of CLOUDY as shown in Fig. 2.

Now we can derive the [C_{II}] line flux ($F_{[\text{CII}]}$) emerging from a plane-parallel slab following the three-zone model. $F_{[\text{CII}]}$ can be calculated using

$$F_{[\text{CII}]} = \Lambda_{[\text{CII}]}^{(1)} l_s + \Lambda_{[\text{CII}]}^{(2)} (l_{\text{F}} - l_s), \quad (13)$$

where the first and second terms correspond to the contribution of [C_{II}] line flux by Zone I and Zone II, respectively. $\Lambda_{[\text{CII}]}^{(1)}$ ($\Lambda_{[\text{CII}]}^{(2)}$) in the above equation represents the [C_{II}] cooling rate (erg s⁻¹ cm⁻³) of gas in Zone I (II). In the above and the following equations, the superscript “(1)” (“(2)”) indicates the properties of gas in Zone I (II). We neglect the [C_{II}] emission from the H₂ region (Zone III).

Equation (13) can be rewritten as (see Appendix D for the details)

$$F_{[\text{CII}]} \approx h_{\text{P}} \nu_{[\text{CII}]} \left(\frac{g_{\text{u}}}{g_{\text{l}}} \right) R_{\text{ul}}^{\text{e}^-} (T^{(1)}) n_{\text{C}^+}^{(1)} n_{\text{e}^-}^{(1)} l_s + \frac{2}{5} h_{\text{P}} \nu_{[\text{CII}]} \left(\frac{g_{\text{u}}}{g_{\text{l}}} \right) R_{\text{ul}}^{\text{H}_1} (T^{(2)}) n_{\text{C}^+}^{(2)} n_{\text{H}_1}^{(2)} (l_{\text{F}} - l_s), \quad (14)$$

where h_{P} is the Planck constant, $\nu_{[\text{CII}]} = 1900.5 \text{ GHz}$ is the rest-frame frequency of the [C_{II}] line, $g_{\text{u}} = 4$ ($g_{\text{l}} = 2$) is the statistical weight of the ²P_{3/2} (²P_{1/2}) state, $R_{\text{ul}}^{\text{e}^-}$ ($R_{\text{ul}}^{\text{H}_1}$) is the downward rate coefficient (s⁻¹) for C⁺ + e⁻ (C⁺ + H₁) collision, and $n_{\text{C}^+}^{(1)}$ (and $n_{\text{C}^+}^{(2)}$), $n_{\text{e}^-}^{(1)}$ and $n_{\text{H}_1}^{(2)}$ represent the number density of C⁺ ion, electron and H atom, respectively. Equation (14) implies that in Zone I (II), the

main collision partner of C^+ ion is electron (H atom). Knowing that $n_{e^-}^{(1)} \approx n_H$ and $n_{H_I}^{(2)} \approx n_H$ (see the *upper* panels of Fig. 2), we can rewrite equation (14) to be

$$F_{[C_{II}]} = h_P \nu_{[C_{II}]} \left(\frac{g_u}{g_l} \right) \left[R_{ul}^{e^-} n_{C^+}^{(1)} N_s + \frac{2}{5} R_{ul}^{H_I} n_{C^+}^{(2)} (N_F - N_s) \right], \quad (15)$$

where $N_F = n_H l_F$ and $N_s = n_H l_s$. Furthermore, $n_{C^+}^{(1)}$ and $n_{C^+}^{(2)}$ in the above equation can be rewritten as

$$n_{C^+}^{(1)} = n_H x_{C^+}^{(1)} \mathcal{A}_C \quad \text{and} \quad n_{C^+}^{(2)} = n_H x_{C^+}^{(2)} \mathcal{A}_C, \quad (16)$$

where

$$\mathcal{A}_C = 2.5 \times 10^{-4} \left(\frac{Z_{\text{gas}}}{Z_{\odot}} \right) \quad (17)$$

represents the abundance of carbon. The numerical factor 2.5×10^{-4} in equation (17) is the abundance of carbon in the solar photosphere (Asplund et al. 2009). $x_{C^+}^{(1)}$ ($x_{C^+}^{(2)}$) in equation (16) represents the fraction of carbon in C^+ form in Zone I (II). $x_{C^+}^{(1)}$ is roughly inversely proportional to U (see Appendix E), whereas $x_{C^+}^{(2)} \approx 1$ (see the *middle* panels of Fig. 2). By inputting equation (16) to equation (15), we get

$$\begin{aligned} F_{[C_{II}]} &= n_H \mathcal{A}_C N_F h_P \nu_{[C_{II}]} \left(\frac{g_u}{g_l} \right) \left[R_{ul}^{e^-} x_{C^+}^{(1)} \left(\frac{N_s}{N_F} \right) + \frac{2}{5} R_{ul}^{H_I} \left(\frac{N_F - N_s}{N_F} \right) \right] \\ &= n_H \mathcal{A}_C N_F \bar{\epsilon}_{[C_{II}], \text{slab}}, \end{aligned} \quad (18)$$

where we define

$$\begin{aligned} \bar{\epsilon}_{[C_{II}], \text{slab}} &= h_P \nu_{[C_{II}]} \left(\frac{g_u}{g_l} \right) \left[R_{ul}^{e^-} x_{C^+}^{(1)} \left(\frac{N_s}{N_F} \right) + \frac{2}{5} R_{ul}^{H_I} \left(\frac{N_F - N_s}{N_F} \right) \right] \\ &\equiv \alpha x_{C^+}^{(1)} \left(\frac{N_s}{N_F} \right) + \gamma \left(\frac{N_F - N_s}{N_F} \right) \end{aligned} \quad (19)$$

as the *specific [CII] cooling rate* of the slab ($\text{erg s}^{-1} \text{cm}^3$). It can be shown that (see Appendix D for the details)

$$\begin{aligned} \alpha &\equiv h_P \nu_{[C_{II}]} \left(\frac{g_u}{g_l} \right) R_{ul}^{e^-} (T^{(1)}) \\ &\approx 10^{-21} \text{ erg s}^{-1} \text{ cm}^3 \quad (T^{(1)} \approx 10^4 \text{ K}) \end{aligned} \quad (20)$$

and

$$\begin{aligned} \gamma &\equiv \frac{2}{5} h_P \nu_{[C_{II}]} \left(\frac{g_u}{g_l} \right) R_{ul}^{H_I} (T^{(2)}) \\ &\approx 10^{-23} \text{ erg s}^{-1} \text{ cm}^3 \quad (T^{(2)} \approx 10^2 \text{ K}) \end{aligned} \quad (21)$$

From equation (19), we see that $\bar{\epsilon}_{[C_{II}], \text{slab}}$ depends on $x_{C^+}^{(1)}$, N_s and N_F , and varies typically within the range $10^{-23} - 10^{-21} \text{ erg s}^{-1} \text{ cm}^3$.

Likewise, we can derive the $[C_{II}]$ luminosity of a spherical uniform gas cloud ($L_{[C_{II}], \text{cl}}$). $L_{[C_{II}], \text{cl}}$ can be expressed as

$$L_{[C_{II}], \text{cl}} = \begin{cases} 4\pi \int_0^{R_{\text{cl}}} \Lambda_{[C_{II}]}^{(1)} r^2 dr & (\text{if } l_s \geq R_{\text{cl}}) \\ 4\pi \left[\int_{R_{\text{cl}}-l_s}^{R_{\text{cl}}} \Lambda_{[C_{II}]}^{(1)} r^2 dr + \int_{R_{\text{cl}}-\min(l_F, R_{\text{cl}})}^{R_{\text{cl}}-l_s} \Lambda_{[C_{II}]}^{(2)} r^2 dr \right] & (\text{if } l_s < R_{\text{cl}}) \end{cases} \quad (22)$$

The first condition of equation (22) (*i.e.* $l_s \geq R_{\text{cl}}$) corresponds to when the cloud is fully ionized, while the second condition (*i.e.* $l_s < R_{\text{cl}}$) corresponds to when neutral hydrogen region (Zone II) forms in

the cloud. Through simple re-arrangement, $L_{[C_{II}], \text{cl}}$ can be expressed as

$$L_{[C_{II}], \text{cl}} = f_{[C_{II}], \text{cl}} \left(\frac{M_{\text{cl}}}{\mu_H m_H} \right) n_H \mathcal{A}_C \bar{\epsilon}_{[C_{II}], \text{cl}}, \quad (23)$$

where $f_{[C_{II}], \text{cl}}$ represents the fraction of the gas mass that is in H^+ or H_I phases (Zone I and Zone II), M_{cl} indicates the mass of the gas cloud, μ_H is the mean molecular weight of the gas and m_H represents the proton mass. By definition, $f_{[C_{II}], \text{cl}} = 1$ when $l_F > R_{\text{cl}}$ and the cloud becomes H_2 -free. $\bar{\epsilon}_{[C_{II}], \text{cl}}$ in equation (22) represents the *specific [CII] cooling rate* of the spherical uniform cloud, which accounts for the relative contribution of the $[C_{II}]$ emission from H^+ and H_I regions ($10^{-23} \lesssim \bar{\epsilon}_{[C_{II}], \text{cl}} \lesssim 10^{-21} \text{ erg s}^{-1} \text{ cm}^3$). Like $\bar{\epsilon}_{[C_{II}], \text{slab}}$ for the plane-parallel slab (equation 19), $\bar{\epsilon}_{[C_{II}], \text{cl}}$ depends on $x_{C^+}^{(1)}$, N_s and N_F but have different functional relation with these parameters due to the difference in geometry. We refer the readers to Appendix F, where we present the derivation for $\bar{\epsilon}_{[C_{II}], \text{cl}}$.

Note that we do not take into account the effects of the CMB background on the $[C_{II}]$ cooling rate of gas in the analytic solution for the toy models presented in this section. While the CMB sets a floor for the excitation (or spin) temperature of gas and boosts the upper level ($^2P_{3/2}$) population of the $[C_{II}]$ transition ('CMB heating'), it acts as a background against which the $[C_{II}]$ line is measured ('CMB attenuation'). The CMB effects (both heating and attenuation) can be important for the $[C_{II}]$ emission from the low-density and low-temperature gas in galaxies at high redshifts ($z \gtrsim 6$) (see Appendix D). We find, however, that the total $[C_{II}]$ luminosity of the FIRE sample is not significantly affected by the CMB (in agreement with Lagache et al. 2018). This is due to the fact that the bulk of the $[C_{II}]$ luminosity of the high- z ($z \gtrsim 6$) galaxies in our sample originates from the gas of densities in excess of the densities where the CMB effects become important.

5.2 A scaling relation for the $L_{[C_{II}]}$ /SFR ratio of galaxies

We have summarized the key points of the F19 model for the structures of a plane-parallel gas slab that is exposed to an external radiation field. We then derive the $[C_{II}]$ luminosity of a uniform spherical gas cloud (equation 23). Following the results of the toy models, we now present a scaling relation for the $[C_{II}]$ luminosity of galaxies, based on which we will explore the origins of the $[C_{II}]$ deficit of galaxies.

From equation (23), one would expect that the $[C_{II}]$ luminosity ($L_{[C_{II}]}$) of galaxy has a similar expression, *i.e.*

$$L_{[C_{II}]} \sim f_{[C_{II}]} \left(\frac{M_{\text{gas}}}{\mu m_H} \right) \bar{n}_{\text{gas}} \bar{\mathcal{A}}_C \bar{\epsilon}_{[C_{II}]}, \quad (24)$$

where we have replaced M_{cl} in equation (23) by M_{gas} , *i.e.* the gas mass of galaxy²¹. $f_{[C_{II}]}$ ($= 1 - f_{H_2}$) in the above equation represents the fraction of the total gas mass in ionized or neutral atomic hydrogen forms (Zone I and Zone II), and \bar{n}_{gas} , $\bar{\mathcal{A}}_C$ and $\bar{\epsilon}_{[C_{II}]}$ represent the *statistical average* of gas density, carbon abundance and specific $[C_{II}]$ cooling rate of the galaxy, respectively. We can then divide the two sides of equation (24) by galaxy SFR, and obtain

$$\frac{L_{[C_{II}]}}{\text{SFR}} \sim f_{[C_{II}]} t_{\text{dep}} \bar{n}_{\text{gas}} \bar{\mathcal{A}}_C \bar{\epsilon}_{[C_{II}]} (\mu m_H)^{-1} \quad (25)$$

²¹ We calculate the gas mass of galaxy using the gas particles within $0.1 R_{\text{vir}}$ around the DM halo centre having $T < 10^5 \text{ K}$.

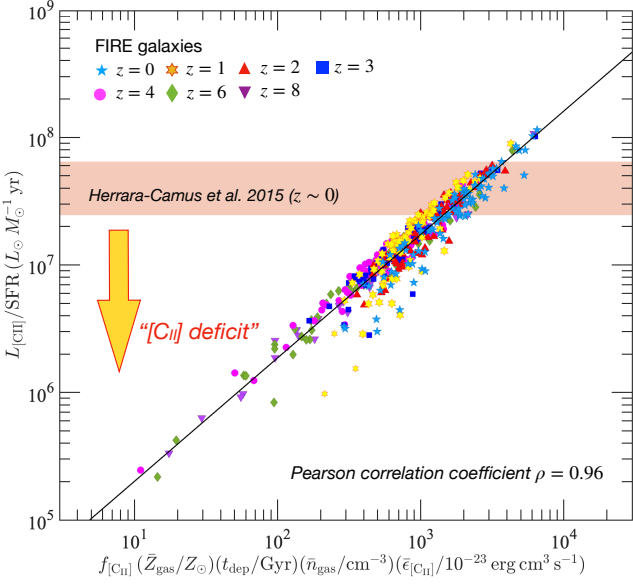


Figure 10. The relation between the $L_{[\text{CII}]}/\text{SFR}$ ratio and $f_{[\text{CII}]}\bar{Z}_{\text{gas}}t_{\text{dep}}\bar{n}_{\text{gas}}\bar{\epsilon}_{[\text{CII}]}$ of the FIRE galaxies at different redshifts (cyan stars for $z = 0$, yellow hexagons for $z = 1$, red triangles for $z = 2$, blue squares for $z = 3$, magenta circles for $z = 4$, green diamonds for $z = 6$ and purple downward triangles for $z = 8$). The orange shaded band indicates the mean $L_{[\text{CII}]}/\text{SFR}$ ratio of the local star-forming galaxy sample measured by H15. The width of the band indicates the $\pm 1\sigma$ scatter. The solid black line shows the best linear fit to the data of the FIRE galaxies. The FIRE galaxies show a strong linear correlation (Pearson correlation coefficient $\rho = 0.96$) between $L_{[\text{CII}]}/\text{SFR}$ and $f_{[\text{CII}]}\bar{Z}_{\text{gas}}t_{\text{dep}}\bar{n}_{\text{gas}}\bar{\epsilon}_{[\text{CII}]}$. A large number of the FIRE galaxies in our sample are below the mean $L_{[\text{CII}]}/\text{SFR}$ ratio of the H15 sample (and those of the local L11; L14 samples, which are not shown in the figure), showing a [CII] deficit.

where

$$t_{\text{dep}} \equiv \frac{M_{\text{gas}}}{\text{SFR}} \quad (26)$$

is the *gas depletion time* of the galaxy (e.g., Genzel et al. 2015; Tacchella et al. 2016; Semenov et al. 2017; Scoville et al. 2017; Tacconi et al. 2018; Feldmann 2020). Through further re-arrangement, equation (25) can be expressed as

$$\frac{L_{[\text{CII}]} / L_{\odot}}{\text{SFR} / (M_{\odot} \text{yr}^{-1})} \sim 4 \times 10^5 f_{[\text{CII}]} \left(\frac{\bar{Z}_{\text{gas}}}{Z_{\odot}} \right) \times \left(\frac{t_{\text{dep}}}{\text{Gyr}} \right) \left(\frac{\bar{n}_{\text{gas}}}{\text{cm}^{-3}} \right) \left(\frac{\bar{\epsilon}_{[\text{CII}]}}{10^{-23} \text{erg s}^{-1} \text{cm}^3} \right) \quad (27)$$

$$\propto f_{[\text{CII}]}\bar{Z}_{\text{gas}}t_{\text{dep}}\bar{n}_{\text{gas}}\bar{\epsilon}_{[\text{CII}]}, \quad (28)$$

where we have replaced the carbon abundance \bar{A}_{C} in equation (25) by metallicity \bar{Z}_{gas} using equation (17).

Equation (27) indicates that the $L_{[\text{CII}]}/\text{SFR}$ ratio of galaxy is determined by five physical parameters, $f_{[\text{CII}]}$, \bar{Z}_{gas} , t_{dep} , \bar{n}_{gas} and $\bar{\epsilon}_{[\text{CII}]}$. Whilst $f_{[\text{CII}]}$ and t_{dep} are *global* properties of galaxy, which are well defined, the other three parameters are the *statistical average* of the corresponding physical properties of all different ‘gas clouds’ in the ISM. This contrasts with the toy models (uniform plane-parallel slab or spherical cloud), where each of these properties (gas density, gas metallicity, and the specific [CII] cooling rate) has a single, definite value.

In Fig. 10, we show the relation between the $L_{[\text{CII}]}/\text{SFR}$ ratio of the FIRE sample at $z = 0 - 8$ and their $f_{[\text{CII}]}\bar{Z}_{\text{gas}}t_{\text{dep}}\bar{n}_{\text{gas}}\bar{\epsilon}_{[\text{CII}]}$,

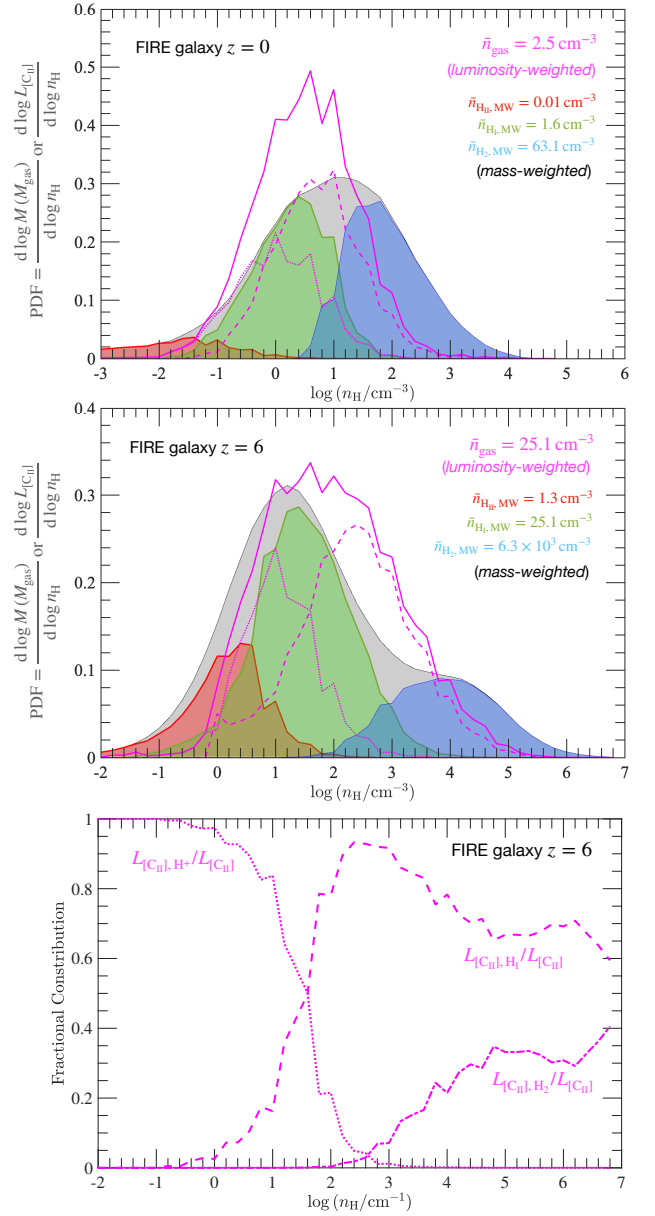


Figure 11. In the *top* and *middle* panels, we present the gas density Probability Density Functions (PDFs) for two selected FIRE galaxies at $z = 0$ and $z = 6$, respectively. The $z = 6$ galaxy exhibits a relatively denser ISM. Magenta lines in both panels indicate the *luminosity-weighted* PDFs. Specifically, solid, dotted, and dashed lines represent the results for the total gas, H⁺ gas (Zone I), and H₁ gas (Zone II) in the ISM. The shaded areas in both panels depict the *mass-weighted* gas density PDFs. Grey, red, green, and blue areas represent the results for the total gas, H⁺ gas (Zone I), H₁ gas (Zone II), and H₂ gas (Zone III), respectively. In the *bottom* panel, dotted, dashed, and dash-dotted lines show the fraction of the [CII] emission from the selected $z = 6$ galaxy originating from the H⁺, H₁, and H₂ gas, respectively.

where \bar{n}_{gas} , \bar{Z}_{gas} and $\bar{\epsilon}_{[\text{CII}]}$ are the *luminosity-weighted* gas density

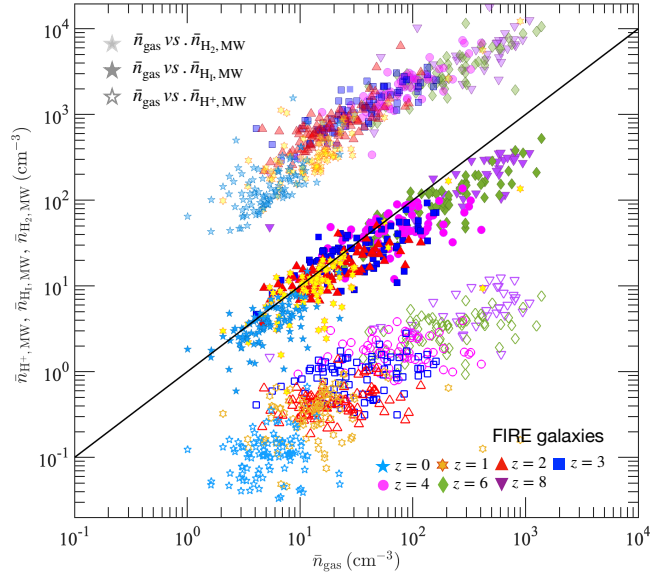


Figure 12. The relation between the $[\text{CII}]$ luminosity-weighted gas density (\bar{n}_{gas}) and the mass-weighted density of the H^+ ($\bar{n}_{\text{H}^+, \text{MW}}$), H_1 ($\bar{n}_{\text{H}_1, \text{MW}}$) and H_2 gas ($\bar{n}_{\text{H}_2, \text{MW}}$) of the FIRE galaxies at $z = 0 - 8$. Filled, empty and semi-transparent symbols correspond to the $\bar{n}_{\text{H}_1, \text{MW}}$ vs. \bar{n}_{gas} , the $\bar{n}_{\text{H}^+, \text{MW}}$ vs. \bar{n}_{gas} and the $\bar{n}_{\text{H}_2, \text{MW}}$ vs. \bar{n}_{gas} relations, respectively. The diagonal line indicates the one-to-one relationship. It can be seen that \bar{n}_{gas} appears to be close to $\bar{n}_{\text{H}_1, \text{MW}}$, both being systematically lower (higher) than $\bar{n}_{\text{H}_2, \text{MW}}$ ($\bar{n}_{\text{H}^+, \text{MW}}$).

²², gas metallicity²³ and specific $[\text{CII}]$ cooling rate of the galaxies, respectively. Our FIRE sample follows a clear linear scaling relation on the diagram (Pearson correlation coefficient $\rho = 0.96$), which is in agreement with equation (27).

In the same figure, we explicitly show the mean $L_{[\text{CII}]} / \text{SFR}$ ratio of the $z = 0$ star-forming galaxy sample of H15 (shaded orange band). The H15 sample demonstrates an almost linear correlation between $L_{[\text{CII}]}$ and SFR. As a result, the $L_{[\text{CII}]} / \text{SFR}$ ratio remains nearly independent of SFR across the range of $\text{SFR} \approx 10^{-3} - 10 M_{\odot} \text{yr}^{-1}$ (see Table 2). We therefore can use the mean $L_{[\text{CII}]} / \text{SFR}$ ratio from the H15 sample as a reference point. Galaxies with significantly lower $L_{[\text{CII}]} / \text{SFR}$ ratios than this reference point are considered to exhibit a $[\text{CII}]$ deficit. It is evident from the figure that a substantial number

²² Note that we use the ‘luminosity-weighted median gas density’, *i.e.* the gas density at the 50th percentile of $[\text{CII}]$ luminosity, instead of the ‘luminosity-weighted mean gas density’. This is because the gas density PDF of galaxy resembles a lognormal function, exhibiting an elongated tail at the high density end. Under certain circumstances, the ‘mean gas density’ can be strongly biased by the $[\text{CII}]$ -emitting gas at the highest density ($n_{\text{H}} \gtrsim 10^3 \text{cm}^{-3}$, see the lower panel of Fig. 11), and hence is not statistically representative for the part of the gas that contributes the bulk of the $[\text{CII}]$ emission of galaxy. Throughout this paper, we use the term ‘luminosity-weighted’ for simplicity when we refer to ‘luminosity-weighted median’. Similarly, ‘mass-weighted’ in this paper refers to ‘mass-weighted median’, *i.e.* value at the 50th percentile of mass. In Appendix G, we show explicitly the difference between the ‘luminosity-weighted median gas density’ and the ‘luminosity-weighted mean gas density’ of the FIRE galaxy sample. The former is higher by a factor of ~ 5 on average.

²³ Unlike the gas densities, the luminosity-weighted mean and the luminosity-weighted median gas metallicity are similar. Both are higher than the mass-weighted gas metallicity (see Appendix H).

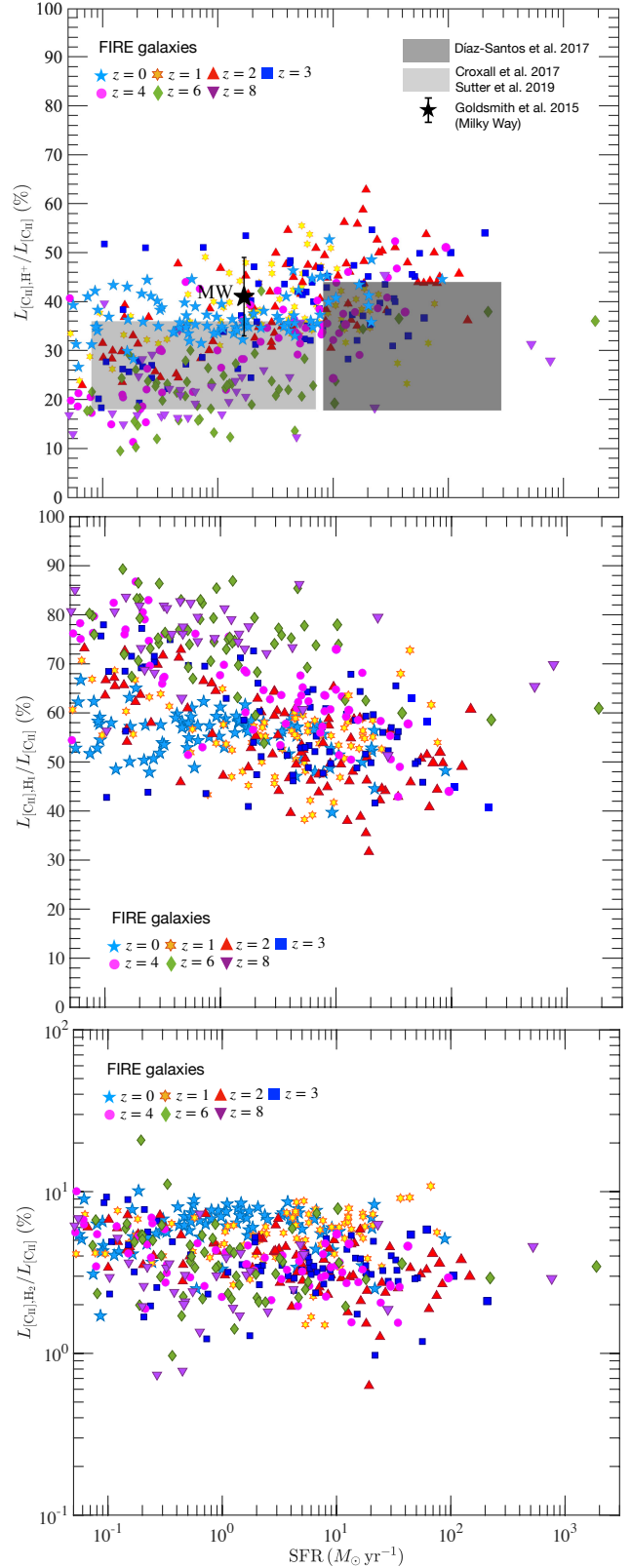


Figure 13. The fraction of the total $[\text{CII}]$ luminosity of the FIRE galaxy sample that originates from the H^+ (upper panel), H_1 (middle panel) and H_2 gas phases (lower panel) as a function of their SFR. In the upper panel, the dark (light) shaded area indicates the observational result ($\pm 1\sigma$) of the local $z = 0$ samples by Sutter et al. (2019). The black hexagon, along with the error bar, represents the constraint on the Galactic Plane measured by Goldsmith et al. (2015).

of the FIRE galaxies in our sample, particularly the early galaxies, display a [C_{II}] deficit.

One crucial question is identifying the primary contributor to the [C_{II}] emission in a galaxy's ISM. The ISM exhibits a wide density range spanning several orders of magnitude, with denser regions dominated by H₂ and diffuse regions by H⁺ gas. In Fig. 11, we depict the [C_{II}] luminosity-weighted (magenta lines) and gas mass-weighted (grey and coloured shaded areas) probability density functions (PDFs) for n_H in two selected FIRE galaxies at z = 0 (*top* panel) and z = 6 (*middle* panel). The figure illustrates that [C_{II}] emission in FIRE galaxies originates from gas spanning a wide density range across several orders of magnitude. Interestingly, we observe that the luminosity-weighted gas density (\bar{n}_{gas}) of FIRE galaxies closely aligns with the mass-weighted density of H_I gas ($\bar{n}_{\text{H I, MW}}$) in the ISM. Both are notably higher (lower) than the mass-weighted density of H⁺ (H₂) gas. This relationship is more evident in Fig. 12, where we depict the correlation between \bar{n}_{gas} and the mass-weighted gas density of H⁺, H_I, and H₂ gas for the FIRE sample at z = 0 – 8.

This observation can be explained by the inefficiency of the bulk of the diffuse, ionized H⁺ gas in producing [C_{II}] emission due to its low gas density ($L_{[\text{C II}], \text{cl}}/M_{\text{cl}} \propto n_{\text{H}}$, see equation 23). Conversely, in the densest ISM regions where gas is primarily in molecular hydrogen form (Zone III), there is not much [C_{II}] emission due to the scarcity of ionized carbon (predominantly in Zone I and Zone II) in those areas. Consequently, the majority of the [C_{II}] luminosity in FIRE galaxies at z = 0 – 8 originates from gas within the intermediate density range.

We present in Fig. 13 the fractional contribution of [C_{II}] emission from different gas phases (H⁺, H_I and H₂) in the FIRE galaxies. Notably, 50% – 80% of the total [C_{II}] emission originates from H_I gas regions, with the majority of the remaining emission attributed to H⁺ gas. Inside the galaxy, the contribution of H_I gas dominates in intermediate and high-density regions, while H⁺ gas dominates in the diffuse regions in the ISM. This trend is illustrated in the *bottom* panel of Fig. 11.

The predicted fractional contribution of the H⁺ gas aligns closely with the upper limits of the observational data reported by Diaz-Santos et al. (2017), who investigated the LIRGs in the GOALS (Armus et al. 2009) sample, as well as Sutter et al. (2019), who studied a sample of normal star-forming galaxies from the KINGFISH (Kennicutt et al. 2011) catalogue. Additionally, our results demonstrate strong agreement with the findings of Goldsmith et al. (2015), who conducted measurements along the Galactic Plane.

Finally, we find that only < 10% of the [C_{II}] emission originates from H₂ gas in our sample (see Section 6.1 for further discussions).

5.3 The physical origins of [C_{II}] deficit of galaxies

In the previous section, we have presented a simple analytic expression for the $L_{[\text{C II}]}/\text{SFR}$ ratio of galaxies (equation 27) found with the FIRE galaxy sample. Based on this result, we will probe in this section the origins of the observed [C_{II}] deficit of galaxies.

Equation (27) indicates that the $L_{[\text{C II}]}/\text{SFR}$ ratio of the galaxies depends on five parameters: the fraction of gas in the [C_{II}]-emitting regions (Zone I and Zone II), the depletion time (*i.e.* gas mass per unit SFR), gas density, gas metallicity and the specific [C_{II}] cooling rate. Hence, the [C_{II}] deficit of the galaxies can, in principle, be due to a strong deficit of one or few of the five parameters with respect to the observed local star-forming samples (*e.g.*, L11, L14 and H15). It should be noted that the observed [C_{II}] deficit in the two regimes, high redshifts and high L_{IR} , may not be due to the same reason. We

will separately discuss the origin of the [C_{II}] deficit in these two regimes in this section.

To investigate the factors influencing the [C_{II}] deficit in the FIRE sample, we analyze the $L_{[\text{C II}]}/\text{SFR}$ ratio in relation to a range of parameters. We assess whether the ‘[C_{II}] deficit’²⁴ diminishes or disappears in new parameter spaces, including $(L_{[\text{C II}]} \text{SFR}^{-1}) f_{[\text{C II}]}$, $(L_{[\text{C II}]} \text{SFR}^{-1}) \bar{Z}_{\text{gas}}^{-1}$, $(L_{[\text{C II}]} \text{SFR}^{-1}) \bar{n}_{\text{gas}}^{-1}$, $(L_{[\text{C II}]} \text{SFR}^{-1}) t_{\text{dep}}^{-1}$ and $(L_{[\text{C II}]} \text{SFR}^{-1}) \bar{\epsilon}_{[\text{C II}]}$.

In Fig. 14, we illustrate these new parameters as a function of SFR for the galaxies in our sample at different redshifts. Note that previous observations have indicated a [C_{II}] deficit at high L_{IR} ($L_{\text{IR}} \gtrsim 10^{11} L_{\odot}$), where SFR and L_{IR} are closely correlated (Fig. 5). By graphing these new parameters as a function of SFR, it becomes clearer which parameters contribute to the [C_{II}] deficit at high SFR ($\sim L_{\text{IR}}$).

In Fig. 15, we also demonstrate how $L_{[\text{C II}]}/\text{SFR}$ in the FIRE sample depends on $f_{[\text{C II}]}$, \bar{Z}_{gas} , \bar{n}_{gas} , t_{dep} and $\bar{\epsilon}_{[\text{C II}]}$, each presented in separate panels. For reference, readers can find the mean values of $f_{[\text{C II}]}$, \bar{Z}_{gas} , \bar{n}_{gas} , t_{dep} and $\bar{\epsilon}_{[\text{C II}]}$, as well as the values of the five new parameters specific to the FIRE sample at each redshift, in Table 8 and Table 7, respectively.

[C_{II}] deficit at high redshifts

The normalization of the $L_{[\text{C II}]}-\text{SFR}$ relation for the FIRE sample consistently decreases with increasing redshift. The mean $L_{[\text{C II}]}/\text{SFR}$ ratio of the galaxies reduces by 0.8 dex (approximately a factor of 6) from z = 0 to z = 8 (as shown in column 2 of Table 7).

Table 7, as well as Fig. 14, demonstrates that the evolution of the $L_{[\text{C II}]}/\text{SFR}$ ratio in galaxies is primarily influenced by \bar{Z}_{gas} and t_{dep} , as the [C_{II}] deficit diminishes at almost all redshifts in the parameter spaces of $(L_{[\text{C II}]}/\text{SFR}) t_{\text{dep}}^{-1}$ and $(L_{[\text{C II}]}/\text{SFR}) \bar{Z}_{\text{gas}}^{-1}$. This suggests that the [C_{II}] deficit in high-redshift galaxies is attributed to either low gas metallicity or a deficiency of gas capable of producing [C_{II}] emission per unit SFR.

A closer look at Table 7 reveals that t_{dep} is the key parameter driving the evolution of the $L_{[\text{C II}]}-\text{SFR}$ relation at z ≤ 3, while \bar{Z}_{gas} plays a more critical role at z ≥ 4. This shift is due to t_{dep} decreasing more significantly from z = 0 to 3 (from 6.3 to 1.1 Gyr, by a factor of ~ 6) compared to the change from z = 3 to 8 (from 1.1 to 0.73 Gyr, by only ~ 30%) as outlined in Table 8. In contrast, \bar{Z}_{gas} for the FIRE sample decreases sharply with redshift at z = 3 – 8 (from 0.43 Z_⊙ to 0.09 Z_⊙, by a factor of ~ 5), exerting a more pronounced impact on the evolution of $L_{[\text{C II}]}/\text{SFR}$ than t_{dep} .

Unlike t_{dep} and \bar{Z}_{gas} , $\bar{\epsilon}_{[\text{C II}]}$ has a relatively modest effect on the redshift evolution of $L_{[\text{C II}]}/\text{SFR}$. From z = 0 to z = 8, the mean $\bar{\epsilon}_{[\text{C II}]}$ of the FIRE sample experiences a slight decrease with redshift (by a factor of 4, as seen in Table 8). The [C_{II}] deficit persists at high redshifts in the parameter space of $(L_{[\text{C II}]}/\text{SFR}) \bar{\epsilon}_{[\text{C II}]}^{-1}$ (Table 7).

The other two parameters, \bar{n}_{gas} and $f_{[\text{C II}]}$, have *completely* no

²⁴ In Section 5.3, the concept of the ‘[C_{II}] deficit’ extends beyond comparing a galaxy’s $L_{[\text{C II}]}/\text{SFR}$ ratio to that of z = 0 normal SFGs; it also encompasses the consideration of the five new parameters. We establish the mean values of these new parameters for local SFGs as the new reference points. Galaxies with significantly lower values for any of the new parameters compared to the z = 0 SFGs are categorized as *having a ‘[C_{II}] deficit’ in that particular parameter space*. For those galaxies that exhibit a ‘[C_{II}] deficit’ in the $L_{[\text{C II}]}/\text{SFR}$ ratio but possess similar or higher values for one of the new parameters than the z = 0 SFGs, we consider their ‘[C_{II}] deficit’ as *‘disappearing’ within the new parameter space*.

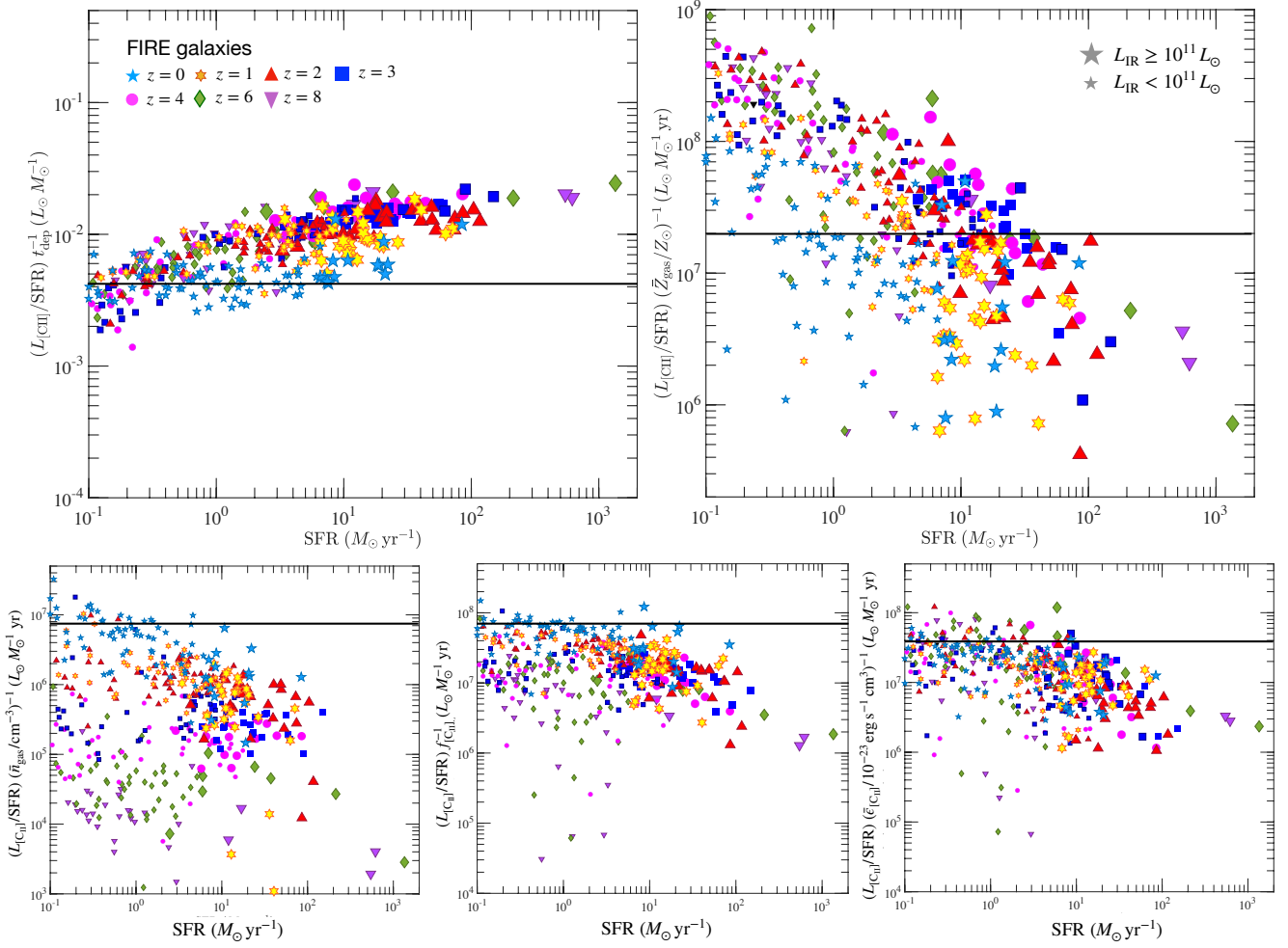


Figure 14. The relation between $L_{[\text{CII}]}/\text{SFR} t_{\text{dep}}^{-1}$ (upper left), $L_{[\text{CII}]}/\text{SFR} \bar{Z}_{\text{gas}}^{-1}$ (upper right), $L_{[\text{CII}]}/\text{SFR} \bar{n}_{\text{gas}}^{-1}$ (lower left), $L_{[\text{CII}]}/\text{SFR} f_{[\text{CII}]}^{-1}$ (lower middle) and $L_{[\text{CII}]}/\text{SFR} \bar{\epsilon}_{[\text{CII}]}^{-1}$ (lower right) against SFR of the FIRE galaxies at different redshifts (cyan stars for $z = 0$, yellow hexagons for $z = 1$, red triangles for $z = 2$, blue squares for $z = 3$, magenta circles for $z = 4$, green diamonds for $z = 6$ and purple downward triangles for $z = 8$). In each panel, large symbols denote galaxies with $L_{\text{IR}} \geq 10^{11} L_{\odot}$, while small symbols denote galaxies with $L_{\text{IR}} < 10^{11} L_{\odot}$. The solid black line indicates the mean value of the normal SFGs at $z = 0$. The figure reveals that the reduced $L_{[\text{CII}]}/\text{SFR}$ ratio of the galaxies with high SFR (at high z) is primarily due to a relatively low t_{dep} (gas metallicity). (see Section 5.3 for the details).

Table 7. The difference between the mean values of $L_{[\text{CII}]}/\text{SFR}$, $L_{[\text{CII}]}/\text{SFR} t_{\text{dep}}^{-1}$, $L_{[\text{CII}]}/\text{SFR} \bar{Z}_{\text{gas}}^{-1}$, $L_{[\text{CII}]}/\text{SFR} \bar{n}_{\text{gas}}^{-1}$, $L_{[\text{CII}]}/\text{SFR} f_{[\text{CII}]}^{-1}$ and $L_{[\text{CII}]}/\text{SFR} \bar{\epsilon}_{[\text{CII}]}^{-1}$ for the FIRE galaxies at redshift z and the values of $z = 0$ normal star-forming galaxies (SFGs) in the sample.

z	$\Delta \log \left(\frac{L_{[\text{CII}]}}{\text{SFR}} \right)$ (dex)	$\Delta \log \left(\frac{L_{[\text{CII}]}}{\text{SFR}} t_{\text{dep}}^{-1} \right)$ (dex)	$\Delta \log \left(\frac{L_{[\text{CII}]}}{\text{SFR}} \bar{Z}_{\text{gas}}^{-1} \right)$ (dex)	$\Delta \log \left(\frac{L_{[\text{CII}]}}{\text{SFR}} \bar{n}_{\text{gas}}^{-1} \right)$ (dex)	$\Delta \log \left(\frac{L_{[\text{CII}]}}{\text{SFR}} f_{[\text{CII}]}^{-1} \right)$ (dex)	$\Delta \log \left(\frac{L_{[\text{CII}]}}{\text{SFR}} \bar{\epsilon}_{[\text{CII}]}^{-1} \right)$ (dex)
1	-0.38	0.39	-0.11	-0.67	-0.25	-0.23
2	-0.32	0.36	0.31	-0.71	-0.34	-0.30
3	-0.50	0.41	0.27	-1.15	-0.51	-0.30
4	-0.58	0.37	0.53	-1.54	-0.60	-0.22
6	-0.70	0.21	0.78	-2.08	-0.67	-0.09
8	-0.81	0.22	0.67	-2.58	-0.86	-0.11

contribution to the $[\text{CII}]$ deficit at high redshifts. Both of these parameters increase with redshift, with higher \bar{n}_{gas} indicating a more compact ISM in earlier galaxies. While it may seem that an increase in gas density should lead to higher $L_{[\text{CII}]}/\text{SFR}$ (according to the

relationship $L_{[\text{CII}],\text{cl}}/M_{\text{cl}} \propto n_{\text{H}}$, equation 23), this effect is overshadowed by the combined impact of t_{dep} and \bar{Z}_{gas} on $L_{[\text{CII}]}/\text{SFR}$.

The increase in $f_{[\text{CII}]}$ with redshift suggests that our sample includes more H_2 gas-poor galaxies at higher redshifts, where a larger fraction of carbon in the ISM gas becomes ionized. Nevertheless, the

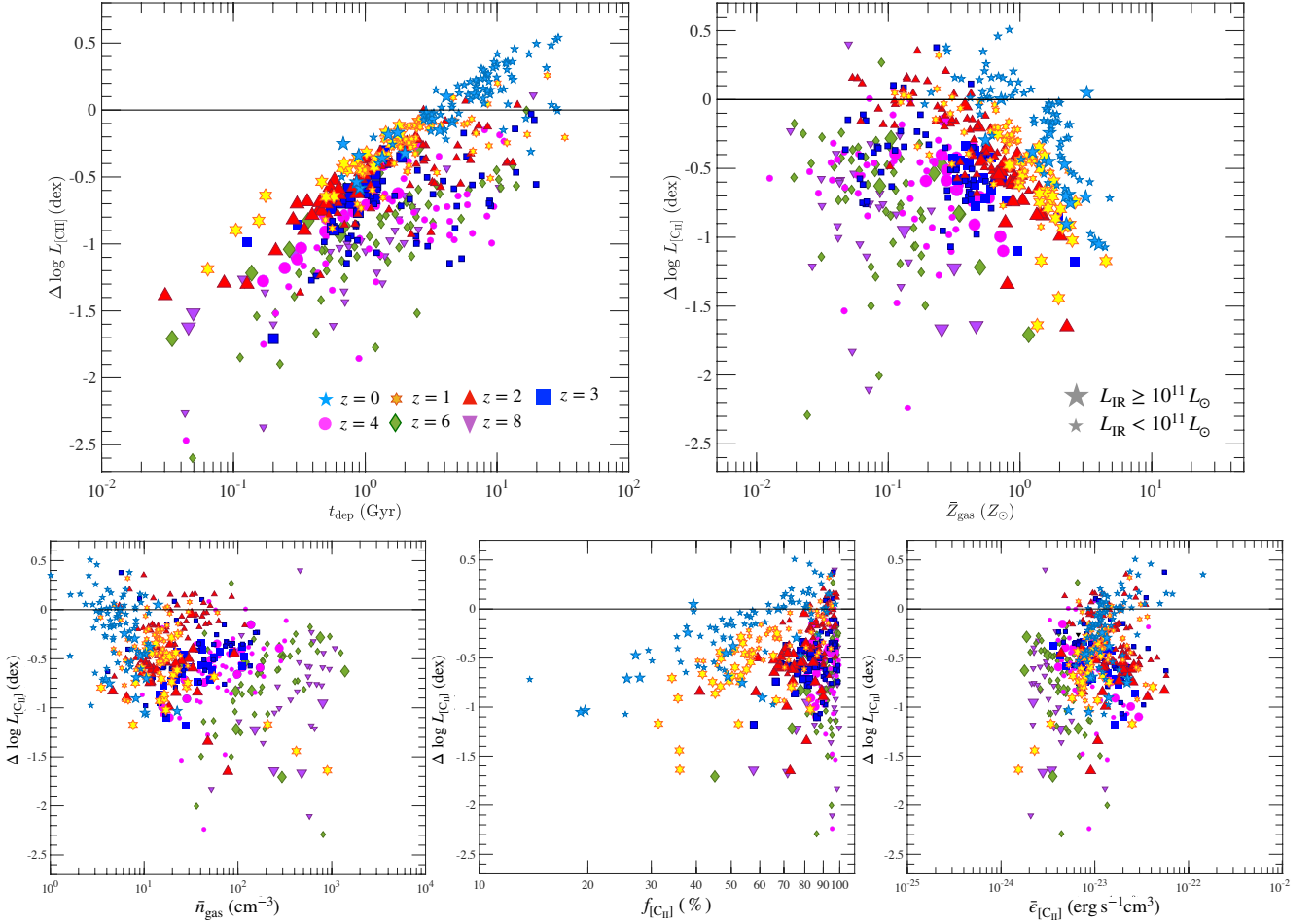


Figure 15. $\Delta(\log L_{\text{CII}})$ as a function of t_{dep} (upper left), \bar{Z}_{gas} (upper right), \bar{n}_{gas} (lower left), f_{CII} (lower middle) and $\bar{\epsilon}_{\text{CII}}$ (lower right) of the FIRE galaxies at different redshifts, where $\Delta(\log L_{\text{CII}})$ represents the offset between the $L_{\text{CII}}/\text{SFR}$ ratio of the galaxies and the observed mean value of the local star-forming sample of H15 ($4.3 \times 10^7 L_{\odot} M_{\odot}^{-1} \text{yr}$). In each panel, large (small) symbols correspond to the FIRE galaxies having $L_{\text{IR}} \geq 10^{11} L_{\odot}$ ($L_{\text{IR}} < 10^{11} L_{\odot}$).

Table 8. The mean of t_{dep} , \bar{Z}_{gas} , $\bar{n}_{\text{gas}}^{-1}$, f_{CII} and $\bar{\epsilon}_{\text{CII}}$ of the FIRE galaxy sample at different redshifts.

z	$\langle \frac{t_{\text{dep}}}{\text{Gyr}} \rangle$	$\langle \frac{\bar{Z}_{\text{gas}}}{Z_{\odot}} \rangle$	$\langle \frac{\bar{n}_{\text{gas}}}{\text{cm}^{-3}} \rangle$	$\langle f_{\text{CII}} \rangle$	$\langle \frac{\bar{\epsilon}_{\text{CII}}}{10^{-23} \text{ erg s}^{-1} \text{ cm}^3} \rangle$
Total					
0	6.30	1.69	5.2	0.57	1.2
1	2.02	1.08	14.6	0.63	1.1
2	1.02	0.56	17.3	0.85	1.6
3	1.10	0.43	30.3	0.88	1.2
4	1.14	0.24	63.6	0.92	0.8
6	0.86	0.12	180.9	0.95	0.5
8	0.73	0.09	468.8	0.97	0.3
$L_{\text{IR}} \geq 10^{11} L_{\odot}$					
0	1.88	2.40	8.7	0.43	1.2
1	1.32	1.45	17.3	0.52	0.8
2	0.52	1.07	17.8	0.74	1.6
3	0.83	0.54	40.6	0.78	0.9
4	0.69	0.36	59.9	0.85	0.9
6	0.51	0.32	217.7	0.81	0.4
8	0.09	0.59	360.0	0.74	0.3

influence of f_{CII} on the evolution of $L_{\text{CII}}/\text{SFR}$ is insignificant, as the mean f_{CII} of the galaxies in our sample increases by no more than a factor of 2 from $z = 0$ to $z = 8$ (from 57% to 97%, as shown in Table 8).

In summary, the decrease in $L_{\text{CII}}/\text{SFR}$ for the FIRE sample with redshift is primarily driven by a reduction in t_{dep} and gas metallicity. While t_{dep} plays a more significant role at $z \leq 3$, gas metallicity becomes the key parameter driving the [CII] deficit in galaxies at higher redshifts. The redshift evolution of \bar{n}_{gas} , f_{CII} , and $\bar{\epsilon}_{\text{CII}}$ has either no or limited impact.

[CII] deficit at high L_{IR}

The FIRE sample shows a consistent trend of decreasing $L_{\text{CII}}/L_{\text{IR}}$ ratio with L_{IR} at each redshift. To identify the primary driver of the [CII] deficit in IR-luminous galaxies, we examined how each of the five physical parameters (f_{CII} , t_{dep} , \bar{n}_{gas} , \bar{Z}_{gas} , and $\bar{\epsilon}_{\text{CII}}$) depends on L_{IR} .

In Table 8, we present the mean values of f_{CII} , t_{dep} , \bar{n}_{gas} , \bar{Z}_{gas} , and $\bar{\epsilon}_{\text{CII}}$ for galaxies with $L_{\text{IR}} \geq 10^{11} L_{\odot}$ (where galaxies are observed to exhibit a [CII] deficit) at different redshifts. We also include the mean values for the entire sample, which includes fainter galaxies. The table, as well as Fig. 15, reveals that IR-luminous galaxies ($L_{\text{IR}} \geq 10^{11} L_{\odot}$) typically have lower t_{dep} and f_{CII} , but

higher \bar{n}_{gas} and \bar{Z}_{gas} compared to the rest of the sample at a given redshift. This suggests that IR-luminous galaxies are richer in metals and H_2 gas, have more compact ISM, and shorter gas depletion time. The mean $\bar{\epsilon}_{[\text{CII}]}$ of these galaxies shows no significant dependence on L_{IR} .

Therefore, the reduced $L_{[\text{CII}]}/\text{SFR}$ ratio in IR-bright galaxies can be attributed to their lower t_{dep} (*i.e.*, gas mass per SFR) and $f_{[\text{CII}]}$. Fig. 14 indicates that t_{dep} plays a more significant role than $f_{[\text{CII}]}$. While these galaxies still exhibit a ‘[CII] deficit’ in the space of $(L_{[\text{CII}]}/\text{SFR})f_{[\text{CII}]}^{-1}$ (*lower middle panel*), their $(L_{[\text{CII}]}/\text{SFR})t_{\text{dep}}^{-1}$ (*upper left panel*) is higher than that of local star-forming galaxies. Hence, the primary reason for the reduced $L_{[\text{CII}]}/\text{SFR}$ in these galaxies compared to local star-forming galaxies is their lower t_{dep} .

It’s worth noting that $(L_{[\text{CII}]}/\text{SFR})t_{\text{dep}}^{-1}$ can be re-written as $L_{[\text{CII}]} / M_{\text{gas}}$, following equation 26. Therefore, an alternative interpretation of the upper left panel of Fig. 14 is that the ISM of IR-luminous galaxies produces more [CII] emission per unit gas mass than fainter ones (due to higher gas metallicity and density). If t_{dep} were a constant, meaning that M_{gas} is proportional to SFR, IR-luminous galaxies should exhibit an excess in $L_{[\text{CII}]}/\text{SFR}$ rather than a deficit. The fact that they exhibit a reduced $L_{[\text{CII}]}/\text{SFR}$ ratio compared to local star-forming galaxies is due to their low gas mass relative to their SFR.

5.4 The two regimes of [CII] emission of galaxies

In the previous section, we have shown with the FIRE sample that the main driver of the [CII] deficit at high redshifts and high L_{IR} is different. The observed [CII] deficit of the galaxies at $z \geq 4$ (at $L_{\text{IR}} \geq 10^{11} L_{\odot}$) may be due to their low gas metallicity (gas depletion time). In this section, we explore the fundamental reason for galaxies having different origin of [CII] deficit in the two regimes.

We at first discuss the $L_{[\text{CII}]}/\text{SFR}$ vs. t_{dep} relation of the FIRE galaxies (Section 5.4.1). We subsequently explore the reason for galaxies showing two distinct regimes on the $\Delta(\log L_{[\text{CII}]})$ vs. t_{dep} diagram (Section 5.4.2). Finally, we discuss how this is related to the distinct origin of [CII] deficit at high redshifts and high L_{IR} (Section 5.4.3).

5.4.1 The $L_{[\text{CII}]}/\text{SFR}$ vs. t_{dep} relation

The FIRE galaxies exhibit two distinct regimes on the $\Delta(\log L_{[\text{CII}]})$ vs. t_{dep} diagram. While a considerable number of the galaxies show a tight linear correlation between their $\log(t_{\text{dep}}/\text{Gyr})$ and $\Delta(\log L_{[\text{CII}]})$, exhibiting a linear sequence (we hereafter refer to it as the ‘deficit-depletion time sequence’, or DDS), others show larger scatter on the diagram and fall systematically below the DDS.

The galaxies on the DDS appear to be more H_2 gas-rich. In Fig. 16, we show the same $L_{[\text{CII}]}/\text{SFR}$ vs. t_{dep} relation of the FIRE sample as in Fig. 15 (*upper left panel*), but colour-code the data points by the H_2 gas mass fraction, f_{H_2} , of the galaxies instead of their redshift. It can be seen from Fig. 16 that the galaxies along the DDS tend to be more H_2 gas-rich, having $f_{\text{H}_2} \geq 50\%$ (equivalent to $f_{[\text{CII}]} \lesssim 50\%$). Besides, we see from the two figures that the majority of the low-redshift ($z = 0 - 2$), shown by cyan stars, yellow hexagons and red triangles in Fig. 15) and IR-luminous ($L_{\text{IR}} \geq 10^{11} L_{\odot}$, indicated by large symbols in Fig. 15 and Fig. 16) galaxies locate on or close to the DDS.

We derive the best-fit linear scaling relation between $\log(t_{\text{dep}}/\text{Gyr})$ and $\Delta(\log L_{[\text{CII}]})$ for the H_2 gas-rich galaxies in our

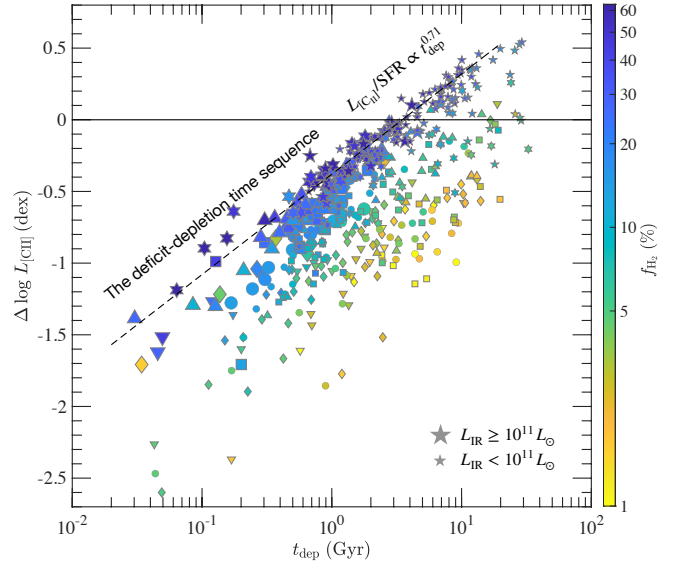


Figure 16. The relation between t_{dep} and $\Delta(\log L_{[\text{CII}]})$ of the FIRE sample at $z = 0 - 8$ (same as the *upper left panel* of Fig. 15 except for the colour). The data points are colour-coded by f_{H_2} of the galaxies. The large (small) symbols represent the galaxies having $L_{\text{IR}} \geq 10^{11} L_{\odot}$ ($L_{\text{IR}} < 10^{11} L_{\odot}$). The H_2 gas-rich galaxies ($f_{\text{H}_2} \geq 50\%$) exhibit a linear correlation between $\log(t_{\text{dep}}/\text{Gyr})$ and $\Delta(\log L_{[\text{CII}]})$ (indicated by the black dashed line), which can be converted to a power-law relation $L_{[\text{CII}]}/\text{SFR} \propto t_{\text{dep}}^{0.71}$ (equation 30).

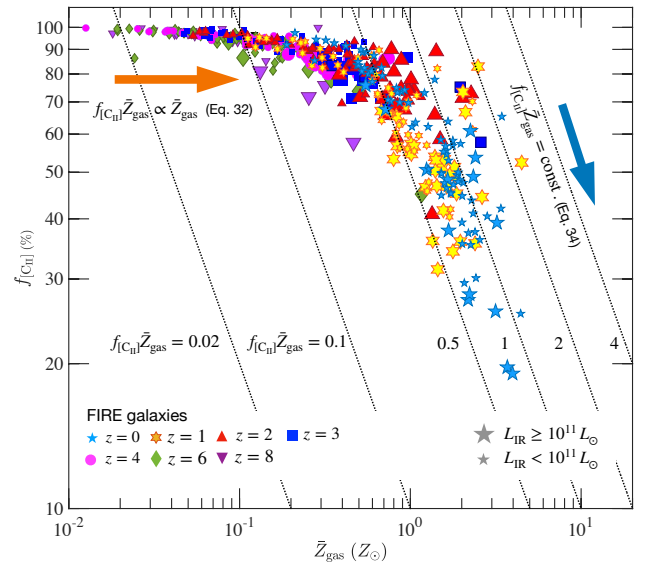


Figure 17. The relation between \bar{Z}_{gas} and $f_{[\text{CII}]}$ of the FIRE sample at different redshifts. The large (small) symbols represent the galaxies having $L_{\text{IR}} \geq 10^{11} L_{\odot}$ ($L_{\text{IR}} < 10^{11} L_{\odot}$). The black dotted lines indicate the relation of $f_{[\text{CII}]} \bar{Z}_{\text{gas}} = 0.02, 0.1, 0.5, 1, 2$ and 4 (from left to right). At $\bar{Z}_{\text{gas}} \lesssim Z_{\odot}$, where galaxies are H_2 gas-poor, $f_{[\text{CII}]} \approx 1$ and $f_{[\text{CII}]} \bar{Z}_{\text{gas}} \approx \bar{Z}_{\text{gas}}$ (*c.f.* equation 32). At larger \bar{Z}_{gas} , $f_{[\text{CII}]}$ scales roughly inversely with \bar{Z}_{gas} and hence $f_{[\text{CII}]} \bar{Z}_{\text{gas}} \approx \text{const.}$ (*c.f.* equation 34).

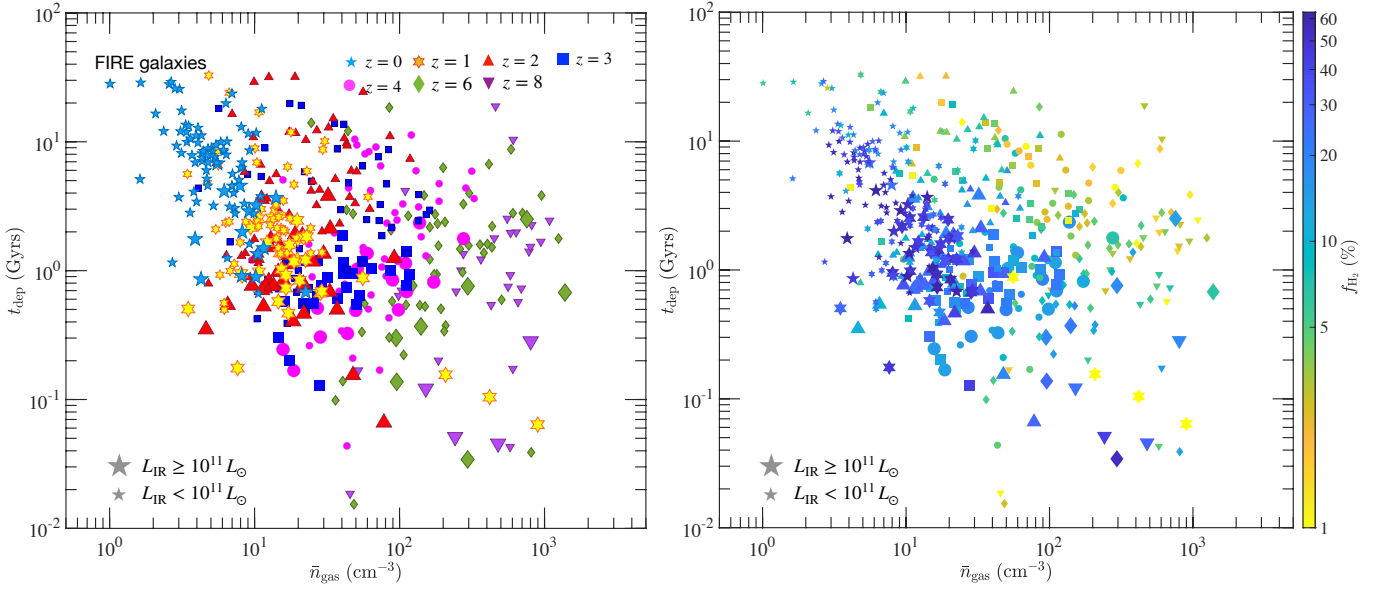


Figure 18. The relation between \bar{n}_{gas} and t_{dep} of the FIRE sample at different redshifts. The data points in the *left (right)* panel are colour-coded by the redshift (f_{H_2}) of the galaxies. Large (small) symbols represent the galaxies having $L_{\text{IR}} \geq 10^{11} L_{\odot}$ ($L_{\text{IR}} < 10^{11} L_{\odot}$). The FIRE galaxies show a clear anti-correlation between t_{dep} and \bar{n}_{gas} , in particular, the H₂ gas-rich galaxies in the sample.

sample having $f_{\text{H}_2} \geq 50\%$, *i.e.*

$$\Delta(\log L_{[\text{CII}]}) = (-0.38 \pm 0.01) + (0.71 \pm 0.03) \log \left(\frac{t_{\text{dep}}}{\text{Gyr}} \right), \quad (29)$$

which can be rewritten as

$$\frac{L_{[\text{CII}]} / L_{\odot}}{\text{SFR} / (M_{\odot} \text{ yr}^{-1})} = 1.78 \times 10^7 \left(\frac{t_{\text{dep}}}{\text{Gyr}} \right)^{0.71}. \quad (30)$$

The coefficient of determination is $R^2 = 0.936$.

5.4.2 The two regimes on the $\Delta(\log L_{[\text{CII}]})$ vs. t_{dep} diagram

The reasons for the H₂ gas-rich galaxies ($f_{\text{H}_2} \geq 50\%$) showing a linear sequence on the $\Delta(\log L_{[\text{CII}]})$ vs. t_{dep} diagram are threefolds: i) Their $f_{[\text{CII}]} \bar{Z}_{\text{gas}}$ ‘saturates’, meaning that it becomes almost like a constant and hence $L_{[\text{CII}]} / \text{SFR}$ of the galaxies simply scales to $t_{\text{dep}} \bar{n}_{\text{gas}}$, ii) their t_{dep} and \bar{n}_{gas} anti-correlate with each other, and iii) $\bar{\epsilon}_{[\text{CII}]}$ has relatively small variation among different galaxies.

Let us at first understand the $f_{[\text{CII}]}$ vs. \bar{Z}_{gas} relation. In Fig. 17, we show the $f_{[\text{CII}]}$ vs. \bar{Z}_{gas} relation for the FIRE sample. It can be seen that at $\bar{Z}_{\text{gas}} \lesssim Z_{\odot}$, $f_{[\text{CII}]}$ barely declines from unity ($f_{[\text{CII}]} \approx 1$) with increasing \bar{Z}_{gas} , whereas at higher \bar{Z}_{gas} , $f_{[\text{CII}]}$ declines sharply and $f_{[\text{CII}]} \bar{Z}_{\text{gas}}$ becomes approximately a constant (‘saturates’) with increasing \bar{Z}_{gas} (or decreasing $f_{[\text{CII}]}$).

The shape of the $f_{[\text{CII}]}$ vs. \bar{Z}_{gas} relation of the FIRE galaxies can be understood as follows. Consider a spherical gas cloud having a radius R_{cl} and a surface-to-centre column density $N_{\text{cl}} (= n_{\text{H}} R_{\text{cl}})$. When the cloud is metal and dust-poor (having very low Z_{gas} and δ_{dgr}), the LW photons from the radiation field can penetrate the entire cloud (*i.e.* $l_{\text{F}} > R_{\text{cl}}$) and dissociate all the molecular hydrogen (H₂) and neutral carbon (C_I and CO) in the cloud. In such a low-metallicity (or δ_{dgr}) regime, we have

$$f_{[\text{CII}], \text{cl}} \approx 1 \quad (31)$$

and

$$f_{[\text{CII}], \text{cl}} Z_{\text{gas}} \propto Z_{\text{gas}}. \quad (32)$$

Since $N_{\text{F}} \propto l_{\text{F}} \propto \delta_{\text{dgr}}^{-1} \propto Z_{\text{gas}}^{-1}$ (equation 10 and 11), indicating stronger dust absorption of UV photons with increasing gas metallicity, l_{F} decreases with Z_{gas} and will become equal or less than R_{cl} when Z_{gas} becomes sufficiently large. Through simple mathematics, it can be derived that for a spherical geometry, $f_{[\text{CII}]} Z_{\text{gas}}$ increases *sub-linearly* with Z_{gas} until when $l_{\text{F}} \ll R_{\text{cl}}$, we have

$$f_{[\text{CII}], \text{cl}} \propto \frac{N_{\text{F}}}{N_{\text{cl}}} \propto (Z_{\text{gas}} N_{\text{cl}})^{-1} \quad (33)$$

or

$$f_{[\text{CII}], \text{cl}} Z_{\text{gas}} = \text{constant}. \quad (34)$$

It is not surprising to find similar scaling relations with the FIRE galaxies, $f_{[\text{CII}]} \bar{Z}_{\text{gas}} \approx \bar{Z}_{\text{gas}}$ at low \bar{Z}_{gas} and $f_{[\text{CII}]} \bar{Z}_{\text{gas}} \approx \text{const.}$ at high \bar{Z}_{gas} (as shown in Fig. 17), given that the ISM of the galaxies can be viewed as being made up of numerous such idealized gas ‘clouds’. The ‘saturation’ of $f_{[\text{CII}]} \bar{Z}_{\text{gas}}$ at high \bar{Z}_{gas} indicates that the [CII] cooling rate of the galaxies does not increase much with gas metallicity due to the shrinking of the size of the [CII]-emitting region (Zone I + Zone II).

Another important reason for the H₂ gas-rich galaxies showing a clear sequence on the $\Delta(\log L_{[\text{CII}]})$ vs. t_{dep} diagram is that their t_{dep} and \bar{n}_{gas} have clear anti-correlation. In Fig. 18, we show the t_{dep} vs. \bar{n}_{gas} relation of the FIRE sample. This anti-correlation is due to the fact that the local free-fall timescale of star-forming clouds decreases with gas density ($t_{\text{ff}} \propto \rho^{-1/2}$), and hence gas is converted into stars more rapidly in the galaxies having denser ISM. It also accounts for the sub-linearity (power law index $n = 0.71$) of the $L_{[\text{CII}]} / \text{SFR}$ vs. t_{dep} scaling relation of the H₂ gas-rich galaxies on the DDS (equation 30).

For the H₂ gas-poor galaxies, the fact that they lie below the DDS on the $\Delta(\log L_{[\text{CII}]})$ vs. t_{dep} diagram (Fig. 16) is because of their low gas metallicity (and hence low $f_{[\text{CII}]} \bar{Z}_{\text{gas}}$). From equation (27),

we see that at fixed $L_{[\text{CII}]}/\text{SFR}$ (equivalently, at fixed $\Delta \log L_{[\text{CII}]}$), their t_{dep} has to be higher than that of the galaxies on the DDS so as to compensate for their having lower $f_{[\text{CII}]} \bar{Z}_{\text{gas}}$. Besides, the fact that the H_2 gas-poor galaxies show a larger scatter of t_{dep} at given $\Delta(\log L_{[\text{CII}]})$ (Fig. 16) than the H_2 gas-rich galaxies is due to the non-trivial scatter of $f_{[\text{CII}]} \bar{Z}_{\text{gas}}$ among these galaxies, as opposed to $f_{[\text{CII}]} \bar{Z}_{\text{gas}}$ being like a constant for the H_2 gas-rich galaxies (Fig. 17).

5.4.3 The physical origins of $[\text{CII}]$ deficit of galaxies (a revisit)

The important consequence of $f_{[\text{CII}]} \bar{Z}_{\text{gas}}$ being ‘saturated’ for the H_2 gas-rich galaxies is that the overall $L_{[\text{CII}]}/\text{SFR}$ ratio of the galaxies shows a tight and steep dependence on t_{dep} (equation 30). As a result, t_{dep} becomes the dominating parameter that determines the $L_{[\text{CII}]}/\text{SFR}$ ratio of these galaxies. Their $L_{[\text{CII}]}/\text{SFR}$, in contrast, does not show a clear correlation with any of the other four parameters ($f_{[\text{CII}]}$, \bar{Z}_{gas} , \bar{n}_{gas} or $\bar{\epsilon}_{[\text{CII}]}$).

Now we should be able to understand the fundamental reason for t_{dep} being the main driver of the $[\text{CII}]$ deficit at high L_{IR} . The IR-luminous galaxies are H_2 gas-rich (due both to their being dust-rich and having high gas column density). Hence, they are in the regime where the $L_{[\text{CII}]}/\text{SFR}$ ratio of galaxies is determined primarily by t_{dep} (i.e. they lie on the DDS in the $\Delta(\log L_{[\text{CII}]})$ vs. t_{dep} diagram) and their $[\text{CII}]$ deficit is due to their low t_{dep} .

Besides, we can now understand the redshift evolution of the $L_{[\text{CII}]}/\text{SFR}$ ratio of the FIRE sample at $z = 0 - 2$. At these low redshifts, our sample includes more galaxies that are H_2 gas-rich as a result of their being more metal and dust-rich than the galaxies at higher redshifts. The $L_{[\text{CII}]}/\text{SFR}$ ratio of these low- z galaxies therefore depends more sensitively on t_{dep} .

At higher redshifts, in contrast, our sample includes a large fraction of metal and dust-poor galaxies that are also H_2 gas-poor. They are off the DDS in the $\Delta(\log L_{[\text{CII}]})$ vs. t_{dep} diagram. For these galaxies, $f_{[\text{CII}]} \bar{Z}_{\text{gas}} \approx \bar{Z}_{\text{gas}}$ (Fig. 17) and hence $L_{[\text{CII}]}/\text{SFR}$ of the galaxies depends more sensitively on \bar{Z}_{gas} . As a result, gas metallicity becomes the main driver of the $[\text{CII}]$ deficit of the high- z galaxies in our sample.

6 DISCUSSIONS

6.1 The origins of $[\text{CII}]$ emission in galaxies

In Section 5.2, we presented the fractional contributions of the $[\text{CII}]$ emission from various gas phases in the FIRE galaxies (fig. 13). Here in this section, we will compare our findings with the observational results in more details.

Observational results

Observational studies on the origins of $[\text{CII}]$ emission in galaxies have been limited to the Milky Way and local galaxies.

Estimating the fraction of $[\text{CII}]$ emission that originates from the H^+ gas ($L_{[\text{CII}], \text{H}^+}/L_{[\text{CII}]}$) is relatively straightforward. The common approach is by using the $[\text{NII}]$ 205 μm fine-structure line. This line has a critical density ($\sim 32 \text{ cm}^{-3}$) that is similar to that of the $[\text{CII}]$ 158 μm line ($\sim 45 \text{ cm}^{-3}$) in ionized gas, resulting in a negligible dependence of the $[\text{CII}]_{158 \mu\text{m}}/[\text{NII}]_{205 \mu\text{m}}$ ratio on gas density in the H^+ regions (Oberst et al. 2006; Croxall et al. 2012). Goldsmith et al. (2015) conducted the first large-scale Galactic survey of the $[\text{NII}]_{205 \mu\text{m}}$ line, comprising 149 positions in the Galactic Plane. They showed that 1/3 – 1/2 of the $[\text{CII}]$ emission originates from the H^+ gas in those regions. Using the GOALS sample, Díaz-Santos

et al. (2017) found that H^+ gas contributes to 18% – 35% ($\pm 1\sigma$) of the total $[\text{CII}]$ emission of the LIRGs. A similar result has been reported by Croxall et al. (2017) using the KINGFISH sample, which incorporates more moderately star-forming galaxies (see also the updated result by Sutter et al. 2019 using the same sample). Studies probing small-scale regions in other nearby galaxies (e.g. Okada et al. 2015; Jameson et al. 2018; Tarantino et al. 2021) have also indicated a lower $L_{[\text{CII}], \text{H}^+}/L_{[\text{CII}]}$ ratio. Overall, ionized gas does not appear to be the dominant source of $[\text{CII}]$ emission in galaxies based on the local observations.

The $[\text{CII}]$ emission that originates from the H_2 gas regions has been used as a tracer of ‘CO-dark’ H_2 gas (Grenier et al. 2005; Langer et al. 2010, 2014; Wolfire et al. 2010). To disentangle this component from the others, the common method is to compare the velocity profile of $[\text{CII}]$ to those of CO and H_1 21 cm, typically considered tracers of ‘CO-bright’ and H_1 gas, respectively. The remaining $[\text{CII}]$ emission attributed to ‘CO-dark’ H_2 gas. Using this method, Pineda et al. (2013, 2014) find that $\sim 25\%$ of the total $[\text{CII}]$ luminosity of the Milky Way is associated with the ‘CO-dark’ H_2 gas. Similar analyses have been conducted for the Magellanic Clouds (Requena-Torres et al. 2016; Pineda et al. 2017; Lebouteiller et al. 2019; Tarantino et al. 2021) and nearby low-metallicity dwarf galaxies (Fahrion et al. 2017; Madden et al. 2020). The reported fractional contributions of H_2 gas to the total $[\text{CII}]$ emission exhibit a significant scatter among different studies, ranging from $\sim 20\%$ to over 50%. However, it’s important to note that these studies typically probe individual star-forming regions rather than providing a complete mapping of emissions across entire galaxies. Consequently, their results may be biased toward the densest regions within the ISM. Additionally, the findings are constrained by small sample sizes and may be influenced by the sensitivity limits of the observations.

Simulated vs. observational results

In Section 5.2, we demonstrated that the primary source of $[\text{CII}]$ emission in the FIRE galaxies is the H_1 gas phase, constituting 50% to 80% of the total luminosity. The majority of the remaining emission originates from the H^+ gas phase, while the H_2 gas phase contributes only around 10%. The fractional contributions of $[\text{CII}]$ emission from these phases do not strongly depend on the galaxy’s SFR.

We find that the $L_{[\text{CII}], \text{H}^+}/L_{[\text{CII}]}$ ratio at $z = 0$ broadly aligns with the constraints from observations by Goldsmith et al. (2015), Díaz-Santos et al. (2017), Croxall et al. (2017), and Sutter et al. (2019) over a wide range of overlapping SFR values ($\text{SFR} \approx 0.1 - 100 M_{\odot} \text{ yr}^{-1}$), except that our simulations do not produce any system at $z = 0$ that shows a very small ($\lesssim 20\%$) contribution of H^+ gas as some of the local observations have found (e.g. Okada et al. 2015; Jameson et al. 2018; Sutter et al. 2019; Tarantino et al. 2021). This may suggest that our simulations over-predict the amount of diffuse gas in the ISM, where the contribution by the H^+ gas is more significant (see the bottom panel of Fig. 11).

The predicted $L_{[\text{CII}], \text{H}_2}/L_{[\text{CII}]}$ ratio ($\lesssim 10\%$) at $z = 0$ appears to be lower than what recent observational studies (e.g. Pineda et al. 2013, 2014; Tarantino et al. 2021) have reported. The disparity between the simulated and observed $L_{[\text{CII}], \text{H}_2}/L_{[\text{CII}]}$ ratio may suggest that the ISM of the $z = 0$ FIRE galaxies, especially the low-metallicity dwarf systems, has lower gas column densities than the observed samples in the star-forming regions that observations have mainly probed. Studies have shown that self-shielding of H_2 from Lyman-Werner radiation can become significant at high column densities (e.g. Draine & Bertoldi 1996; Madden et al. 1997, 2020; Wolfire et al. 2010). Consequently, a significant amount of C^+ can be found within the envelope of the H_2 regions, and the contribution of H_2 gas

to the [C_{II}] emission can be non-trivial. However, it's worth noting that the reported high $L_{[\text{C}_{\text{II}}], \text{H}_2} / L_{[\text{C}_{\text{II}}]}$ ratio for local galaxies may be largely influenced by several systematic factors, as mentioned earlier.

6.2 Comparison with the previous studies

Here we discuss the relation between the findings of the previous studies to this from this work. Specifically, we will discuss the conclusions regarding the origin of the [C_{II}] deficit at high L_{IR} in Section 6.2.1, whereas in Section 6.2.2, we will compare the predictions of the $L_{[\text{C}_{\text{II}}]}$ -SFR relation of galaxies at redshift $z \geq 5$ from the recent studies with ours.

6.2.1 The [C_{II}] deficit at high L_{IR}

[C_{II}] deficit due to a strong ISRF

A number of studies suggest that the observed [C_{II}] deficit at high L_{IR} is due to a strong ISRF in IR-luminous galaxies. This can result in large positive grain charges, leading to inefficient heating of gas through photo-electric processes in the neutral galactic medium (Tielens & Hollenbach 1985; Kaufman et al. 1999; Malhotra et al. 2001; Croxall et al. 2012; McKinney et al. 2021a). Consequently, the rate of gas cooling via [C_{II}] line drops. Additionally, a strong ISRF (and hence high U) may also give rise to “dust-bounded” H⁺ regions near the newly formed young stars (Bottorff et al. 1998; Abel et al. 2009), where $N_s \approx N_F$ (note: N_s increases about linearly with U until $N_s \approx N_F$). In this scenario, gas cooling through [C_{II}] can become inefficient due to a lack of C⁺ ions in the H⁺ regions — when U is large, a significant fraction of carbon can be ionized further into C²⁺ ions (In Zone I, $x_{\text{C}^+}^{(1)} \approx 1 - x_{\text{C}^{2+}}^{(1)} \propto U^{-1}$, see Appendix E). Both mechanisms can ultimately lead to a reduced $\bar{\epsilon}_{[\text{C}_{\text{II}}]}$ in galaxies.

Examining the FIRE sample, we do not find that the IR-luminous galaxies in our sample exhibit significantly lower $\bar{\epsilon}_{[\text{C}_{\text{II}}]}$ compared to the fainter galaxies at each given redshift, as indicated in Table 8. It is important to note that CLOUDY (version 17.01) incorporates grain charging physics (Baldwin et al. 1991; van Hoof et al. 2004; Abel et al. 2005), and our approach of conducting dust Radiative Transfer (RT) calculations with SKIRT provides a more accurate estimate of the of the ISRF (and hence U) distribution within galaxies compared to previous studies. Our findings suggest that the [C_{II}] deficit at high L_{IR} is not primarily caused by a high U in these galaxies.

However, we do observe that the mean $\bar{\epsilon}_{[\text{C}_{\text{II}}]}$ decreases with redshift from $z = 0$ to $z = 8$ by a factor of ~ 4 , which is associated with an increasing value of U with redshift. We will delve into this effect in more detail in a follow-up study.

[C_{II}] deficit due to a high gas density

It has also been suggested that the [C_{II}] deficit in IR-luminous galaxies can be driven by the high density of the star-forming gas in these galaxies (e.g. Narayanan & Krumholz 2017). With increasing density, ISM gas becomes more shielded from ionizing radiation of massive young stars and therefore more carbon in the ISM gas becomes neutral (in CO or C_I). The [C_{II}] deficit is thus due to a lack of C⁺ ions in the ISM gas in this scenario (*i.e.* due to a low $f_{[\text{C}_{\text{II}}]}$).

This, however, does not seem to be exactly like what we find with the FIRE simulations. The ISM of the FIRE galaxies spans a very wide range of density (see Fig. 11), and even for the most massive starburst galaxies in our sample, much of their [C_{II}] luminosity originates from the gas having intermediate density ($\bar{n}_{\text{gas}} \approx \bar{n}_{\text{H}_I, \text{MW}}$, see Fig. 11). Overall, the luminosity-weighted gas density (\bar{n}_{gas}) of

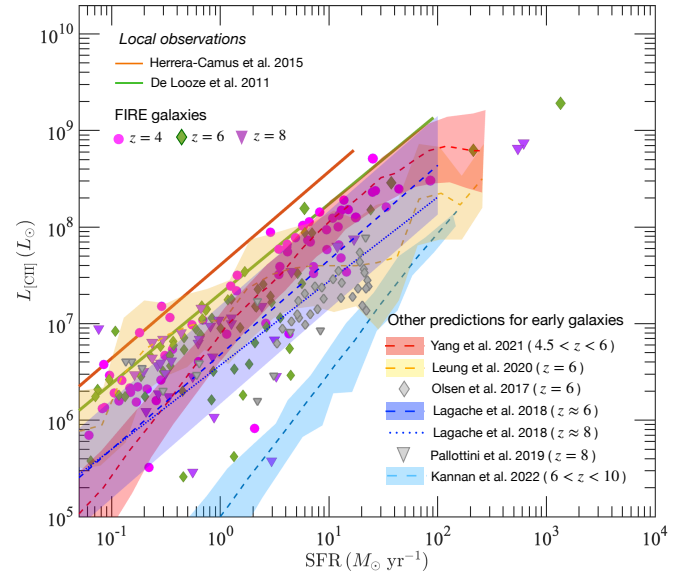


Figure 19. The $L_{[\text{C}_{\text{II}}]}$ -SFR relation at $z \geq 5$ predicted by different simulation groups. Red, yellow, blue and cyan lines indicate the mean result of Yang et al. (2021) ($4.5 < z < 6$), Leung et al. (2020) ($z = 6$), Lagache et al. (2018) (dashed blue line for $z \approx 6$ and dotted blue line for $z \approx 8$), and Kannan et al. (2022b) ($6 < z < 10$). These studies use statistically significant samples. The corresponding coloured shaded areas represent the 1σ dispersion of the data around the mean relation of each sample. In addition, we also show the data of individual galaxies of the Olsen et al. (2017) ($z = 6$) and Pallottini et al. (2019) ($z = 8$) samples by grey diamonds and grey downward triangles, respectively. For reference, we show the observed $L_{[\text{C}_{\text{II}}]}$ -SFR relation of the local star-forming samples of H15 (solid orange line) and L11 (solid green line) as well as the data of the FIRE sample at $z = 4$ (magenta circles), $z = 6$ (green diamonds) and $z = 8$ (purple downward triangles). A [C_{II}] deficit at $z \geq 5$ is generally predicted by various simulation groups.

the IR-luminous galaxies ($L_{\text{IR}} \geq 10^{11} L_{\odot}$) is not much higher than that of the IR-faint galaxies in our sample at any given redshift (see Table 8), and the difference is not as strong as that in t_{dep} . Therefore, the [C_{II}] deficit of the IR-luminous galaxies in FIRE simulations does not appear to be mainly driven by their having too dense ISM gas.

6.2.2 The $L_{[\text{C}_{\text{II}}]}$ -SFR relation at redshift $z \geq 5$

As mentioned in the Introduction, several planned ground-based [C_{II}] line intensity mapping (LIM) experiments will target the emitting sources at redshift $z \geq 5$ (Kovetz et al. 2017), including CCAT-PRIME, CONCERTO and TIME. Predicting the $L_{[\text{C}_{\text{II}}]}$ -SFR relation of galaxies at this early epoch has thus become extremely important for interpreting the upcoming data of these experiments (see e.g. Visbal et al. 2011; Gong et al. 2012; Serra et al. 2016; Fonseca et al. 2017; Padmanabhan 2019; Yue & Ferrara 2019; Chung et al. 2020; Padmanabhan et al. 2022; Karoumpis et al. 2022; Sun et al. 2023; Murmu et al. 2023; Horlaville et al. 2023).

In Fig. 19, we present the results from a number of recent studies. These include the ones using SAMs (Lagache et al. 2018; Yang et al. 2021) as well as those using hydrodynamic simulations (Olsen et al. 2017; Pallottini et al. 2019; Leung et al. 2020; Kannan et al. 2022b). It can be seen that different studies have generally predicted a clear [C_{II}] deficit at $z \geq 5$ with respect to the local samples of L11 and H15, similar to this work using the FIRE simulations. Some have also predicted a mild trend of growing deficit with increasing redshift

(e.g. Lagache et al. 2018; Kannan et al. 2022b). The predicted 1σ scatter of the $L_{[\text{CII}]}$ -SFR relation at a given redshift of these studies is typically as large as 0.3 – 0.5 dex (except Kannan et al. 2022b, which shows noticeably smaller scatter than the others).

There is, however, a clear difference in the normalization and slope of the $L_{[\text{CII}]}$ -SFR relation predicted by the different groups. In particular, Yang et al. (2021) (Kannan et al. 2022b) produce the highest (lowest) normalization among all different groups at SFR $\approx 1\text{--}100 M_{\odot} \text{ yr}^{-1}$. Both also produce a considerably steeper power-law slope (≈ 1.5) than the others.

The difference in the $L_{[\text{CII}]}$ -SFR relation indicates that the predicted ISM properties (e.g. \bar{Z}_{gas} , t_{dep}) of the galaxies at $z \gtrsim 5$ are not well converged between the current simulations. We highlight that the data of the upcoming LIM experiments may provide useful constraints on the ISM properties of the galaxies in this early epoch, given that direct measurement of these properties is very challenging using the current techniques.

7 SUMMARY AND CONCLUSIONS

The $158 \mu\text{m}$ fine structure line of singly ionized carbon ($[\text{CII}]$) has been considered as a SFR indicator since observations of nearby star-forming galaxies found a linear correlation between their $L_{[\text{CII}]}$ and SFR. There is, however, evidence showing that IR-bright ($L_{\text{IR}} \gtrsim 10^{11} L_{\odot}$), starburst galaxies as well as early galaxies at $z \gtrsim 5$ have reduced $L_{[\text{CII}]}/\text{SFR}$ with respect to the local star-forming samples (so-called ‘ $[\text{CII}]$ deficit’ problem). Different models have been posited to explain the origin of the $[\text{CII}]$ deficit of galaxies at high L_{IR} or at high redshifts and yet no consensus has been reached at both regimes.

In this work, we present a comprehensive analysis on the $L_{[\text{CII}]}$ -SFR relation of galaxies using a galaxy sample at $z = 0\text{--}8$ ($M_{*} = 10^7\text{--}5 \times 10^{11} M_{\odot}$) extracted from the cosmological hydrodynamic simulations, which are part of the FIRE project (Hopkins et al. 2014, 2018, 2023), coupled with CLOUDY (Ferland et al. 1998, 2017) models. The sample consists mainly of galaxies ($N_{\text{gal}} \sim 500$) from FIREBOX (Feldmann et al. 2023), a high-resolution cosmological-volume hydrodynamic simulation run with FIRE-2 physics, and is supplemented with a few dozen of high- z massive galaxies from the cosmological ‘zoom-in’ simulations of the MASSIVEFIRE suite (Feldmann et al. 2016, 2017; Anglés-Alcázar et al. 2017). The sample covers an unprecedentedly broad dynamic range among all studies on $[\text{CII}]$, including normal star-forming galaxies, (U)LIRG and SMG candidates as well as UV-bright galaxies at EoR, which can be used to study the full range of the observational data on $[\text{CII}]$ currently available.

The predicted $L_{[\text{CII}]}$ -SFR relation of the FIRE sample agrees well with the observational data. In particular, we successfully reproduce the observed linear correlation of the local star-forming samples over the SFR range $\approx 0.1\text{--}10 M_{\odot} \text{ yr}^{-1}$ (Fig. 4 and Fig. 6). Apart from that, we also reproduce the sharp decline of $L_{[\text{CII}]}/\text{SFR}$ with L_{IR} ($\sim \text{SFR}$) at $L_{\text{IR}} \gtrsim 10^{11} L_{\odot}$ at low and high redshifts, which is consistent with the data of the (U)LIRGs and SMGs in this L_{IR} regime (Fig. 7 and Fig. 9).

Our sample shows a general decline of $L_{[\text{CII}]}/\text{SFR}$ with redshift, in particular, at low SFR (Fig. 8). The mean $L_{[\text{CII}]}/\text{SFR}$ ratio of the early EoR galaxies at $z > 5$ in our sample is about one order of magnitude below the local galaxies, showing a clear $[\text{CII}]$ deficit, similar to what has been previously found with other simulations (Section 6.2.2). Observations of galaxies at EoR have drawn divergent conclusions on their $L_{[\text{CII}]}$ -SFR relation, which is largely due to the uncertainty

in the dust SED shape (or ‘dust temperature’) of the galaxies at these high redshifts. We analyze the sub-mm data of all the observed EoR galaxies and derive their dust-obscured SFR using the ‘dust temperature’ estimated from the SED templates of the FIRE samples self-consistently. We conclude that the $L_{[\text{CII}]}$ -SFR relation of the FIRE galaxies at $z > 5$ is in no conflict with the current observational constraints, including those placed by the recent ALPINE and REBELS surveys.

The $L_{[\text{CII}]}/\text{SFR}$ ratio of the FIRE sample roughly follows a simple linear scaling relationship (equation 27)

$$\frac{L_{[\text{CII}]}}{\text{SFR}} \propto f_{[\text{CII}]} \bar{Z}_{\text{gas}} t_{\text{dep}} \bar{n}_{\text{gas}},$$

where $f_{[\text{CII}]}$ is the mass fraction of ionized or neutral atomic hydrogen gas in the ISM, t_{dep} is the gas depletion time ($= M_{\text{gas}}/\text{SFR}$), and \bar{Z}_{gas} and \bar{n}_{gas} indicate the gas metallicity and gas density that are weighted by $[\text{CII}]$ luminosity. Following this scaling relationship, we find that the key driver of the $[\text{CII}]$ deficit is different at high L_{IR} and high redshifts (Section 5.3). At high L_{IR} , the $[\text{CII}]$ deficit is mainly due to the low t_{dep} of galaxies, indicating that IR-luminous, starburst galaxies have less amount of gas that is able to produce $[\text{CII}]$ emission per unit SFR than the normal star-forming galaxies with moderate SFR. The $[\text{CII}]$ deficit at $z \gtrsim 5$, in contrast, is mainly driven by the low gas metallicity of galaxies at this epoch.

The underlying reason for $[\text{CII}]$ deficit being driven by different physical parameters at high L_{IR} and high redshifts is as follows. In the low-metallicity regime (corresponding to high- z galaxies), $L_{[\text{CII}]}$ of galaxies depends sensitively on metallicity because line emissivity scales linearly with metallicity. In the high-metallicity regime (corresponding to low- z , massive and starburst galaxies), however, such dependence can become weak. This is because dust-to-gas ratio (δ_{dgr}) in the ISM increases with metallicity, which leads to the shrinking of the size of $[\text{CII}]$ -emitting region (Section 5.4). The shrinking of its size almost cancels out the effect of increasing emissivity with metallicity (in this case, $f_{[\text{CII}]} \bar{Z}_{\text{gas}} \approx \text{constant}$). As a result, $L_{[\text{CII}]}/\text{SFR}$ of galaxies does not depend much on metallicity — but instead, on $t_{\text{dep}} = M_{\text{gas}}/\text{SFR}$, see equation (30) — for massive, metal (dust) and H_2 gas-rich starburst galaxies at low redshifts.

In summary, the FIRE simulations have predicted a reduced $L_{[\text{CII}]}/\text{SFR}$ ratio in early high-redshift galaxies, as well as in IR-luminous galaxies, compared to local normal star-forming galaxies, which aligns with what observations have indicated. The results suggest that the ‘ $[\text{CII}]$ deficit’ may be a common phenomenon among galaxies. This finding has significant implications for the interpretation of data from several major upcoming $[\text{CII}]$ line intensity mapping experiments, such as EXCLAIM (Ade et al. 2020), TIME (Sun et al. 2021), CCAT-PRIME (CCAT-Prime collaboration et al. 2021) and CONCERTO (CONCERTO Collaboration et al. 2020; Gkogkou et al. 2023). Our results further imply that utilizing a constant linear $L_{[\text{CII}]}$ -SFR relation derived from nearby star-forming galaxies (e.g. De Looze et al. 2011, 2014; Herrera-Camus et al. 2015) may lead to a systematic overestimation of the cosmic star formation rate density in the high-redshift Universe.

ACKNOWLEDGEMENTS

We thank the anonymous referee for useful comments which have helped improved the quality of this manuscript. LL acknowledges financial support from the Swiss National Science Foundation (hereafter SNSF) (grant no P2ZHP2_199729) and the University of Toronto Faculty of Arts and Science. RF acknowledges financial support from the SNSF (grant no PP00P2_194814,

200021_188552). NM was supported by the Natural Sciences and Engineering Research Council of Canada (grant no RGPIN-2023-04901). DN acknowledges funding from the NSF via AST-1909153. DAA acknowledges support by NSF grants AST-2009687 and AST-2108944, CXO grant TM2-23006X, and Simons Foundation award CCA-1018464. LB acknowledge financial support from the SNSF (grant no PP00P2_194814). CAFG was supported by NSF through grants AST-1715216, AST-2108230, and CAREER award AST-1652522; by NASA through grants 17-ATP17-0067 and 21-ATP21-0036; by STScI through grants HST-AR-16124.001-A and HST-GO-16730.016-A; by CXO through grant TM2-23005X; and by the Research Corporation for Science Advancement (RCSA) through a Cottrell Scholar Award. DTC is supported by a CITA/Dunlap Institute postdoctoral fellowship. The Dunlap Institute is funded through an endowment established by the David Dunlap family and the University of Toronto. DTC also acknowledges support through the Vincent and Beatrice Tremaine Postdoctoral Fellowship at CITA during the preparation and review of this work. JYHC acknowledges support from a CITA postdoctoral fellowship. DK were supported by NSF grant AST-1715101 and the Cottrell Scholar Award from the RCSA. Support for PFH was provided by NSF Research Grants 1911233, 20009234, 2108318, NSF CAREER grant 1455342, NASA grants 80NSSC18K0562, HST-AR-15800. This work was performed in part at the Aspen Center for Physics, which is supported by National Science Foundation grant PHY-2210452. The Flatiron Institute is supported by the Simons Foundation.

We acknowledge PRACE for awarding us access to MareNostrum at the Barcelona Supercomputing Center (BSC), Spain. This research was partly carried out via the Frontera computing project at the Texas Advanced Computing Center. Frontera is made possible by National Science Foundation award OAC-1818253. Computations were performed on the Niagara supercomputer at the SciNet HPC Consortium. SciNet is funded by Innovation, Science and Economic Development Canada; the Digital Research Alliance of Canada; the Ontario Research Fund: Research Excellence; and the University of Toronto. This work was supported in part by a grant from the Swiss National Supercomputing Centre (CSCS) under project IDs s697 and s698. We acknowledge access to Piz Daint at the Swiss National Supercomputing Centre, Switzerland under the University of Zurich's share with the project ID uzh18. This work made use of infrastructure services provided by S3IT (www.s3it.uzh.ch), the Service and Support for Science IT team at the University of Zurich.

The authors would also like to acknowledge the use of AI language model ChatGPT for assistance in refining the writing and language of this manuscript.

DATA AVAILABILITY STATEMENT

The data underlying this article will be shared on reasonable request to the corresponding author.

REFERENCES

- Abel N. P., Ferland G. J., Shaw G., van Hoof P. A. M., 2005, *ApJS*, 161, 65
- Abel N. P., Sarma A. P., Troland T. H., Ferland G. J., 2007, *ApJ*, 662, 1024
- Abel N. P., van Hoof P. A. M., Shaw G., Ferland G. J., Elwert T., 2008, *ApJ*, 686, 1125
- Abel N. P., Dudley C., Fischer J., Satyapal S., van Hoof P. A. M., 2009, *ApJ*, 701, 1147
- Ade P. A. R., et al., 2020, *Journal of Low Temperature Physics*, 199, 1027
- Andika I. T., et al., 2020, *ApJ*, 903, 34
- Anglés-Alcázar D., Faucher-Giguère C.-A., Quataert E., Hopkins P. F., Feldmann R., Torrey P., Wetzel A., Kereš D., 2017, *MNRAS*, 472, L109
- Aravena M., et al., 2016, *ApJ*, 833, 68
- Armus L., et al., 2009, *PASP*, 121, 559
- Asplund M., Grevesse N., Sauval A. J., Scott P., 2009, *ARA&A*, 47, 481
- Baes M., Camps P., 2015, *Astronomy and Computing*, 12, 33
- Baes M., Verstappen J., Looze I. D., Fritz J., Saftly W., Pérez E. V., Stalevski M., Valcke S., 2011, *ApJS*, 196, 22
- Bakx T. J. L. C., et al., 2020, *MNRAS*, 493, 4294
- Baldwin J. A., Ferland G. J., Martin P. G., Corbin M. R., Cota S. A., Peterson B. M., Slettebak A., 1991, *ApJ*, 374, 580
- Bañados E., Decarli R., Walter F., Venemans B. P., Farina E. P., Fan X., 2015, *ApJ*, 805, L8
- Bañados E., et al., 2016, *ApJS*, 227, 11
- Barisic I., et al., 2017, *ApJ*, 845, 41
- Bassini L., Feldmann R., Gensior J., Hayward C. C., Faucher-Giguère C.-A., Cenci E., Liang L., Bernardini M., 2023, *MNRAS*, 525, 5388
- Behrens C., Pallottini A., Ferrara A., Gallerani S., Vallini L., 2018, *MNRAS*, 477, 552
- Bernal J. L., Kovetz E. D., 2022, *A&AR*, 30
- Béthermin M., et al., 2020, *A&A*, 643, A2
- Bisbas T. G., et al., 2022, *ApJ*, 934, 115
- Bischetti M., et al., 2018, *A&A*, 617, A82
- Black J. H., Dalgarno A., 1977, *ApJS*, 34, 405
- Blain A. W., 1999, *MNRAS*, 304, 669
- Boselli A., Gavazzi G., Lequeux J., Pierini D., 2002, *A&A*, 385, 454
- Bottoff M., LaMothe J., Momjian E., Verner E., Vinković D., Ferland G., 1998, *PASP*, 110, 1040
- Bouwens R. J., Illingworth G. D., Franx M., Ford H., 2007, *ApJ*, 670, 928
- Bouwens R. J., et al., 2011, *ApJ*, 737, 90
- Bouwens R. J., et al., 2015, *ApJ*, 803, 34
- Bouwens R. J., et al., 2016, *ApJ*, 833, 72
- Bouwens R. J., Stefanon M., Oesch P. A., Illingworth G. D., Nanayakkara T., Roberts-Borsani G., Labbé I., Smit R., 2019, *ApJ*, 880, 25
- Bouwens R. J., et al., 2022, *ApJ*, 931, 160
- Bowler R. A. A., Bourne N., Dunlop J. S., McLure R. J., McLeod D. J., 2018, *MNRAS*, 481, 1631
- Bowler R. A. A., Jarvis M. J., Dunlop J. S., McLure R. J., McLeod D. J., Adams N. J., Milvang-Jensen B., McCracken H. J., 2020, *MNRAS*, 493, 2059
- Bradač M., et al., 2017, *ApJ*, 836, L2
- Brauer J. R., Dale D. A., Helou G., 2008, *ApJS*, 178, 280
- Breuck C. D., et al., 2014, *A&A*, 565, A59
- Brisbin D., Ferkinhoff C., Nikola T., Parshley S., Stacey G. J., Spoon H., Hailey-Dunsheath S., Verma A., 2015, *ApJ*, 799, 13
- Burgarella D., et al., 2013, *A&A*, 554, A70
- CCAT-Prime collaboration et al., 2021, arXiv e-prints, arXiv:2107.10364
- CONCERTO Collaboration et al., 2020, *A&A*, 642, A60
- Calzetti D., et al., 2007, *ApJ*, 666, 870
- Camps P., Baes M., 2015, *Astronomy and Computing*, 9, 20
- Camps P., Trayford J. W., Baes M., Theuns T., Schaller M., Schaye J., 2016, *MNRAS*, 462, 1057
- Camps P., et al., 2018, *ApJS*, 234, 20
- Cañameras R., et al., 2018, *A&A*, 620, A61
- Capak P. L., et al., 2015, *Nature*, 522, 455
- Carilli C., Walter F., 2013, *ARA&A*, 51, 105
- Carlstrom J. E., et al., 2011, *PASP*, 123, 568
- Carniani S., et al., 2017, *A&A*, 605, A42
- Carniani S., et al., 2018a, *MNRAS*, 478, 1170
- Carniani S., Maiolino R., Smit R., Amorín R., 2018b, *ApJ*, 854, L7
- Carniani S., et al., 2020, *MNRAS*, 499, 5136
- Casey C. M., 2012, *MNRAS*, 425, 3094
- Casey C. M., Narayanan D., Cooray A., 2014, *Physics Reports*, 541, 45
- Casey C. M., et al., 2018a, *ApJ*, 862, 77
- Casey C. M., Hodge J., Zavala J. A., Spilker J., da Cunha E., Staguhn J., Finkelstein S. L., Drew P., 2018b, *ApJ*, 862, 78

- Çatmabacak O., Feldmann R., Anglés-Alcázar D., Faucher-Giguère C.-A., Hopkins P. F., Kereš D., 2022, *MNRAS*, 511, 506
- Chung D. T., Viero M. P., Church S. E., Wechsler R. H., 2020, *ApJ*, 892, 51
- Cochrane R. K., et al., 2019, *MNRAS*, 488, 1779
- Cochrane R. K., Hayward C. C., Anglés-Alcázar D., 2022, *ApJ*, 939, L27
- Contursi A., et al., 2017, *A&A*, 606, A86
- Cooke E. A., et al., 2018, *ApJ*, 861, 100
- Cooray A., et al., 2014, *ApJ*, 790, 40
- Cormier D., et al., 2015, *A&A*, 578, A53
- Cox P., et al., 2011, *ApJ*, 740, 63
- Croxall K. V., et al., 2012, *ApJ*, 747, 81
- Croxall K. V., et al., 2017, *ApJ*, 845, 96
- Curti M., et al., 2023, *MNRAS*, 518, 425
- Davé R., Thompson R., Hopkins P. F., 2016, *MNRAS*, 462, 3265
- Dayal P., Ferrara A., 2018, *Physics Reports*, 780-782, 1
- De Looze I., Baes M., Bendo G. J., Cortese L., Fritz J., 2011, *MNRAS*, 416, 2712
- De Looze I., et al., 2014, *A&A*, 568, A62
- Decarli R., et al., 2017, *Nature*, 545, 457
- Decarli R., et al., 2018, *ApJ*, 854, 97
- Dessauges-Zavadsky M., et al., 2020, *A&A*, 643, A5
- Dey A., et al., 2008, *ApJ*, 677, 943
- Díaz-Santos T., et al., 2013, *ApJ*, 774, 68
- Díaz-Santos T., et al., 2015, *ApJ*, 816, L6
- Díaz-Santos T., et al., 2017, *ApJ*, 846, 32
- Dole H., et al., 2006, *A&A*, 451, 417
- Donnan C. T., et al., 2023, *MNRAS*, 518, 6011
- Draine B. T., Bertoldi F., 1996, *ApJ*, 468, 269
- Draine B. T., Salpeter E. E., 1979, *ApJ*, 231, 438
- Draine B. T., et al., 2007, *ApJ*, 663, 866
- Dullemond C. P., Juhasz A., Pohl A., Sereshti F., Shetty R., Commercon B., Flock M., 2012, RADMC-3D: A multi-purpose radiative transfer tool, *Astrophysics Source Code Library*, record ascl:1202.015 (ascl:1202.015)
- Dunne L., Eales S., Edmunds M., Ivison R., Alexander P., Clements D. L., 2000, *MNRAS*, 315, 115
- Dwek E., 1998, *ApJ*, 501, 643
- Eilers A.-C., et al., 2020, *ApJ*, 900, 37
- Eisenhardt P. R. M., et al., 2012, *ApJ*, 755, 173
- Elbaz D., et al., 2011, *A&A*, 533, A119
- Ellis R. S., et al., 2013, *ApJ*, 763, L7
- Fähring K., et al., 2017, *A&A*, 599, A9
- Faisst A. L., et al., 2017, *ApJ*, 847, 21
- Faisst A. L., et al., 2020a, *ApJS*, 247, 61
- Faisst A. L., Fudamoto Y., Oesch P. A., Scoville N., Riechers D. A., Pavesi R., Capak P., 2020b, *MNRAS*, 498, 4192
- Fan X., et al., 2019, *ApJ*, 870, L11
- Farrah D., et al., 2013, *ApJ*, 776, 38
- Faucher-Giguère C.-A., Lidz A., Zaldarriaga M., Hernquist L., 2009, *ApJ*, 703, 1416
- Federman S. R., Glassgold A. E., Kwan J., 1979, *ApJ*, 227, 466
- Feldmann R., 2017, *MNRAS: Letters*, 470, L59
- Feldmann R., 2020, *Communications Physics*, 3
- Feldmann R., Hopkins P. F., Quataert E., Faucher-Giguère C.-A., Kereš D., 2016, *MNRAS: Letters*, 458, L14
- Feldmann R., Quataert E., Hopkins P. F., Faucher-Giguère C.-A., Kereš D., 2017, *MNRAS*, 470, 1050
- Feldmann R., et al., 2023, *MNRAS*, 522, 3831
- Ferland G. J., Peterson B. M., Horne K., Welsh W. F., Nahar S. N., 1992, *ApJ*, 387, 95
- Ferland G. J., Korista K. T., Verner D. A., Ferguson J. W., Kingdon J. B., Verner E. M., 1998, *PASP*, 110, 761
- Ferland G. J., et al., 2013, *Rev. Mex. Astron. Astrofis.*, 49, 137
- Ferland G. J., et al., 2017, *Rev. Mex. Astron. Astrofis.*, 53, 385
- Ferrara A., Vallini L., Pallottini A., Gallerani S., Carniani S., Kohandel M., Decataldo D., Behrens C., 2019, *MNRAS*, 489, 1
- Ferrara A., et al., 2022, *MNRAS*, 512, 58
- Finkelstein S. L., et al., 2013, *Nature*, 502, 524
- Finkelstein S. L., et al., 2015, *ApJ*, 810, 71
- Fixsen D. J., Dwek E., Mather J. C., Bennett C. L., Shafer R. A., 1998, *ApJ*, 508, 123
- Fonseca J., Silva M. B., Santos M. G., Cooray A., 2017, *MNRAS*, 464, 1948
- Fudamoto Y., et al., 2021, *Nature*, 597, 489
- Fudamoto Y., et al., 2022, *ApJ*, 934, 144
- Fudamoto Y., et al., 2023a, arXiv e-prints, arXiv:2303.07513
- Fudamoto Y., et al., 2023b, arXiv e-prints, arXiv:2309.02493
- Fujimoto S., Ouchi M., Ono Y., Shibuya T., Ishigaki M., Nagai H., Momose R., 2016, *ApJS*, 222, 1
- Fujimoto S., et al., 2019, *ApJ*, 887, 107
- Fujimoto S., et al., 2020, *ApJ*, 900, 1
- Fujimoto S., et al., 2021, *ApJ*, 911, 99
- Fujimoto S., et al., 2022, arXiv e-prints, arXiv:2212.06863
- Fujimoto S., et al., 2023, arXiv e-prints, arXiv:2309.07834
- Garaldi E., Kannan R., Smith A., Springel V., Pakmor R., Vogelsberger M., Hernquist L., 2022, *MNRAS*, 512, 4909
- Geach J. E., et al., 2016, *ApJ*, 832, 37
- Genzel R., Cesarsky C. J., 2000, *ARA&A*, 38, 761
- Genzel R., et al., 2015, *ApJ*, 800, 20
- Gill S. P. D., Knebe A., Gibson B. K., 2004, *MNRAS*, 351, 399
- Gilmore G., Wyse R. F. G., Kuijken K., 1989, *ARA&A*, 27, 555
- Ginolfi M., et al., 2020, *A&A*, 633, A90
- Gkogkou A., et al., 2023, *A&A*, 670, A16
- Gnedin N. Y., Draine B. T., 2014, *ApJ*, 795, 37
- Gnedin N. Y., Kravtsov A. V., 2011, *ApJ*, 728, 88
- Gnedin N. Y., Tassis K., Kravtsov A. V., 2009, *ApJ*, 697, 55
- Goldsmith P. F., Langer W. D., Pineda J. L., Velusamy T., 2012, *ApJS*, 203, 13
- Goldsmith P. F., Yıldız U. A., Langer W. D., Pineda J. L., 2015, *ApJ*, 814, 133
- Gong Y., Cooray A., Silva M., Santos M. G., Bock J., Bradford C. M., Zemcov M., 2012, *ApJ*, 745, 49
- Graciá-Carpio J., et al., 2011, *ApJ*, 728, L7
- Grenier I. A., Casandjian J.-M., Terrier R., 2005, *Science*, 307, 1292
- Griffin M. J., et al., 2010, *A&A*, 518, L3
- Gruppioni C., et al., 2013, *MNRAS*, 432, 23
- Guilloteau S., et al., 1992, *A&A*, 262, 624
- Gullberg B., et al., 2015, *MNRAS*, 449, 2883
- Gullberg B., et al., 2018, *ApJ*, 859, 12
- Habing H. J., 1968, *Bull. Astron. Inst. Netherlands*, 19, 421
- Hahn O., Abel T., 2011, *MNRAS*, 415, 2101
- Hailey-Dunsheath S., 2009, PhD thesis, Cornell University, United States
- Hao C.-N., Kennicutt R. C., Johnson B. D., Calzetti D., Dale D. A., Moustakas J., 2011, *ApJ*, 741, 124
- Harikane Y., et al., 2020, *ApJ*, 896, 93
- Harikane Y., et al., 2023, *ApJS*, 265, 5
- Harrington K. C., et al., 2021, *ApJ*, 908, 95
- Hashimoto T., et al., 2018, *Nature*, 557, 392
- Hashimoto T., et al., 2019a, *PASJ*, 71
- Hashimoto T., et al., 2019b, *MNRAS*, 488, 5029
- Hayward C. C., Kereš D., Jonsson P., Narayanan D., Cox T. J., Hernquist L., 2011, *ApJ*, 743, 159
- Hayward C. C., et al., 2014, *MNRAS*, 445, 1598
- Heintz K. E., Watson D., Oesch P. A., Narayanan D., Madden S. C., 2021, *ApJ*, 922, 147
- Heintz K. E., et al., 2022, *ApJ*, 934, L27
- Heintz K. E., et al., 2023a, *Nature Astronomy*
- Heintz K. E., et al., 2023b, *ApJ*, 944, L30
- Helou G., Malhotra S., Hollenbach D. J., Dale D. A., Contursi A., 2001, *ApJ*, 548, L73
- Herrera-Camus R., et al., 2015, *ApJ*, 800, 1
- Herrera-Camus R., et al., 2018, *ApJ*, 861, 95
- Heyminck S., Kasemann C., Güsten R., de Lange G., Graf U. U., 2006, *A&A*, 454, L21
- Hezaveh Y. D., Marrone D. P., Holder G. P., 2012, *ApJ*, 761, 20
- Hezaveh Y. D., et al., 2013, *ApJ*, 767, 132
- Hildebrand R. H., 1983, *QJRAS*, 24, 267

- Ho P. T. P., Moran J. M., Lo K. Y., 2004, *ApJ*, 616, L1
- Hodge J. A., da Cunha E., 2020, *Royal Society Open Science*, 7, 200556
- Hollenbach D. J., Tielens A. G. G. M., 1999, *Reviews of Modern Physics*, 71, 173
- Hollenbach D. J., Takahashi T., Tielens A. G. G. M., 1991, *ApJ*, 377, 192
- Hopkins P. F., Kereš D., Oñorbe J., Faucher-Giguère C.-A., Quataert E., Murray N., Bullock J. S., 2014, *MNRAS*, 445, 581
- Hopkins P. F., et al., 2018, *MNRAS*, 480, 800
- Hopkins P. F., et al., 2023, *MNRAS*, 519, 3154
- Hopwood R., et al., 2011, *ApJ*, 728, L4
- Horlavlille P., Chung D. T., Bond J. R., Liang L., 2023, *arXiv e-prints*, [arXiv:2309.15733](https://arxiv.org/abs/2309.15733)
- Hu E. M., Cowie L. L., McMahon R. G., Capak P., Iwamuro F., Kneib J.-P., Maihara T., Motohara K., 2002, *ApJ*, 568, L75
- Hughes T. M., et al., 2017, *A&A*, 602, A49
- Indriolo N., McCall B. J., 2012, *ApJ*, 745, 91
- Indriolo N., Geballe T. R., Oka T., McCall B. J., 2007, *ApJ*, 671, 1736
- Inoue A. K., et al., 2016, *Science*, 352, 1559
- Iono D., et al., 2006, *ApJ*, 645, L97
- Ivison R. J., et al., 2010, *A&A*, 518, L35
- Izumi T., et al., 2018, *PASJ*, 70
- Izumi T., et al., 2019, *PASJ*, 71
- Izumi T., et al., 2021a, *ApJ*, 908, 235
- Izumi T., et al., 2021b, *ApJ*, 914, 36
- Jameson K. E., et al., 2018, *ApJ*, 853, 111
- Jones T. A., Swinbank A. M., Ellis R. S., Richard J., Stark D. P., 2010, *MNRAS*
- Kanekar N., Wagg J., Chary R. R., Carilli C. L., 2013, *ApJ*, 771, L20
- Kannan R., Garaldi E., Smith A., Pakmor R., Springel V., Vogelsberger M., Hernquist L., 2022a, *MNRAS*, 511, 4005
- Kannan R., Smith A., Garaldi E., Shen X., Vogelsberger M., Pakmor R., Springel V., Hernquist L., 2022b, *MNRAS*, 514, 3857
- Karoumpis C., Magnelli B., Romano-Díaz E., Haslbauer M., Bertoldi F., 2022, *A&A*, 659, A12
- Katz H., Kimm T., Sijacki D., Haehnelt M. G., 2017, *MNRAS*, 468, 4831
- Katz H., et al., 2019, *MNRAS*, 487, 5902
- Kaufman M. J., Wolfire M. G., Hollenbach D. J., Luhman M. L., 1999, *ApJ*, 527, 795
- Kawamata R., Oguri M., Ishigaki M., Shimasaku K., Ouchi M., 2016, *ApJ*, 819, 114
- Keating L. C., et al., 2020, *MNRAS*, 499, 837
- Kennicutt R. C., 1998, *ApJ*, 498, 541
- Kennicutt R. C., Evans N. J., 2012, *ARA&A*, 50, 531
- Kennicutt R. C., et al., 2011, *PASP*, 123, 1347
- Kessler M. F., et al., 1996, *A&A*, 500, 493
- Khusanova Y., et al., 2021, *A&A*, 649, A152
- Kirkpatrick A., Pope A., Sajina A., Roebuck E., Yan L., Armus L., Díaz-Santos T., Stierwalt S., 2015, *ApJ*, 814, 9
- Knollmann S. R., Knebe A., 2009, *ApJS*, 182, 608
- Knudsen K. K., Richard J., Kneib J.-P., Jauzac M., Clément B., Drouart G., Egami E., Lindroos L., 2016, *MNRAS*, 462, L6
- Knudsen K. K., Watson D., Frayer D., Christensen L., Gallazzi A., Michałowski M. J., Richard J., Zavala J., 2017, *MNRAS*, 466, 138
- Kohandel M., Pallottini A., Ferrara A., Zanella A., Behrens C., Carniani S., Gallerani S., Vallini L., 2019, *MNRAS*, 487, 3007
- Kovetz E. D., et al., 2017, *arXiv e-prints*, [arXiv:1709.09066](https://arxiv.org/abs/1709.09066)
- Kovetz E., et al., 2019, *BAAS*, 51, 101
- Kroupa P., 2002, *Science*, 295, 82
- Krumholz M. R., 2014, *MNRAS*, 437, 1662
- Lagache G., Cousin M., Chatzikos M., 2018, *A&A*, 609, A130
- Langer W. D., Velusamy T., Pineda J. L., Goldsmith P. F., Li D., Yorke H. W., 2010, *A&A*, 521, L17
- Langer W. D., Velusamy T., Pineda J. L., Willacy K., Goldsmith P. F., 2014, *A&A*, 561, A122
- Laporte N., et al., 2017, *ApJ*, 837, L21
- Laporte N., et al., 2019, *MNRAS*, 487, L81
- Le Fèvre O., et al., 2020, *A&A*, 643, A1
- Lebouteiller V., et al., 2019, *A&A*, 632, A106
- Leech K. J., et al., 1999, *MNRAS*, 310, 317
- Leethochawalit N., Roberts-Borsani G., Morishita T., Trenti M., Treu T., 2023a, *MNRAS*, 524, 5454
- Leethochawalit N., et al., 2023b, *ApJ*, 942, L26
- Lehar J., et al., 2000, *ApJ*, 536, 584
- Leipski C., et al., 2013, *ApJ*, 772, 103
- Leipski C., et al., 2014, *ApJ*, 785, 154
- Leitherer C., Heckman T. M., 1995, *ApJS*, 96, 9
- Leitherer C., et al., 1999, *ApJS*, 123, 3
- Leroy A. K., Walter F., Brinks E., Bigiel F., de Blok W. J. G., Madore B., Thornley M. D., 2008, *ApJ*, 136, 2782
- Leung T. K. D., Olsen K. P., Somerville R. S., Davè R., Greve T. R., Hayward C. C., Narayanan D., Popping G., 2020, *ApJ*, 905, 102
- Li Q., Narayanan D., Davè R., Krumholz M. R., 2018, *ApJ*, 869, 73
- Li Q., Narayanan D., Davè R., 2019, *MNRAS*, 490, 1425
- Liang L., Feldmann R., Faucher-Giguère C.-A., Kereš D., Hopkins P. F., Hayward C. C., Quataert E., Scoville N. Z., 2018, *MNRAS:Letters*, 478, L83
- Liang L., et al., 2019, *MNRAS*, 489, 1397
- Liang L., Feldmann R., Hayward C. C., Narayanan D., Çatmabacak O., Kereš D., Faucher-Giguère C.-A., Hopkins P. F., 2021, *MNRAS*, 502, 3210
- Lu N., et al., 2018, *ApJ*, 864, 38
- Luhman M. L., et al., 1998, *ApJ*, 504, L11
- Luhman M. L., Satyapal S., Fischer J., Wolfire M. G., Sturm E., Dudley C. C., Lutz D., Genzel R., 2003, *ApJ*, 594, 758
- Lupi A., Bovino S., 2020, *MNRAS*, 492, 2818
- Lupi A., Pallottini A., Ferrara A., Bovino S., Carniani S., Vallini L., 2020, *MNRAS*, 496, 5160
- Ma X., Hopkins P. F., Faucher-Giguère C.-A., Zolman N., Muratov A. L., Kereš D., Quataert E., 2016, *MNRAS*, 456, 2140
- Ma X., et al., 2019, *MNRAS*, 487, 1844
- Madau P., Dickinson M., 2014, *ARA&A*, 52, 415
- Madden S. C., Poglitsch A., Geis N., Stacey G. J., Townes C. H., 1997, *ApJ*, 483, 200
- Madden S. C., et al., 2013, *PASP*, 125, 600
- Madden S. C., et al., 2020, *A&A*, 643, A141
- Magdis G. E., et al., 2014, *ApJ*, 796, 63
- Magnelli B., Elbaz D., Chary R. R., Dickinson M., Borgne D. L., Frayer D. T., Willmer C. N. A., 2009, *A&A*, 496, 57
- Maiolino R., et al., 2005, *A&A*, 440, L51
- Maiolino R., Caselli P., Nagao T., Walmsley M., Breuck C. D., Meneghetti M., 2009, *A&A*, 500, L1
- Maiolino R., et al., 2015, *MNRAS*, 452, 54
- Malhotra S., et al., 1997, *ApJ*, 491, L27
- Malhotra S., et al., 2001, *ApJ*, 561, 766
- Marrone D. P., et al., 2018, *Nature*, 553, 51
- Matthee J., et al., 2017, *ApJ*, 851, 145
- Matthee J., et al., 2019, *ApJ*, 881, 124
- Mazzucchelli C., et al., 2017, *ApJ*, 849, 91
- McKinney J., Pope A., Armus L., Chary R.-R., Díaz-Santos T., Dickinson M. E., Kirkpatrick A., 2020, *ApJ*, 892, 119
- McKinney J., Armus L., Pope A., Díaz-Santos T., Charmandaris V., Inami H., Song Y., Evans A. S., 2021a, *ApJ*, 908, 238
- McKinney J., Hayward C. C., Rosenthal L. J., Martínez-Galarza J. R., Pope A., Sajina A., Smith H. A., 2021b, *ApJ*, 921, 55
- McKinnon R., Torrey P., Vogelsberger M., 2016, *MNRAS*, 457, 3775
- McLeod D. J., McLure R. J., Dunlop J. S., Robertson B. E., Ellis R. S., Targett T. A., 2015, *MNRAS*, 450, 3032
- McLure R. J., et al., 2013, *MNRAS*, 432, 2696
- Meyer R. A., et al., 2022, *ApJ*, 927, 152
- Miettinen O., et al., 2017, *A&A*, 606, A17
- Molyneux S. J., et al., 2022, *MNRAS*, 512, 535
- Muñoz J. A., Oh S. P., 2016, *MNRAS*, 463, 2085
- Murmu C. S., et al., 2023, *MNRAS*, 518, 3074
- Nahar S. N., Pradhan A. K., 1997, *ApJS*, 111, 339
- Naidu R. P., et al., 2022, *ApJ*, 940, L14
- Narayanan D., Krumholz M. R., 2017, *MNRAS*, 467, 50
- Narayanan D., et al., 2015, *Nature*, 525, 496

- Neri R., Downes D., Cox P., Walter F., 2014, *A&A*, 562, A35
- Neufeld D. A., Wolfire M. G., 2017, *ApJ*, 845, 163
- Novak M., et al., 2020, *ApJ*, 904, 131
- Oberst T. E., et al., 2006, *ApJ*, 652, L125
- Oesch P. A., et al., 2012, *ApJ*, 745, 110
- Oesch P. A., et al., 2016, *ApJ*, 819, 129
- Oesch P. A., Bouwens R. J., Illingworth G. D., Labbé I., Stefanon M., 2018, *ApJ*, 855, 105
- Okada Y., Requena-Torres M. A., Güsten R., Stutzki J., Wiesemeyer H., Pütz P., Ricken O., 2015, *A&A*, 580, A54
- Olsen K. P., Greve T. R., Narayanan D., Thompson R., Toft S., Brinch C., 2015, *ApJ*, 814, 76
- Olsen K., Greve T. R., Narayanan D., Thompson R., Davé R., Rios L. N., Stawinski S., 2017, *ApJ*, 846, 105
- Olsen K., Greve T. R., Narayanan D., Thompson R., Davé R., Rios L. N., Stawinski S., 2018, *ApJ*, 857, 148
- Ota K., et al., 2014, *ApJ*, 792, 34
- Oteo I., et al., 2016, *ApJ*, 827, 34
- Ouchi M., et al., 2013, *ApJ*, 778, 102
- Padmanabhan H., 2019, *MNRAS*, 488, 3014
- Padmanabhan H., Breyse P., Lidz A., Switzer E. R., 2022, *MNRAS*, 515, 5813
- Pallottini A., Ferrara A., Bovino S., Vallini L., Gallerani S., Maiolino R., Salvadori S., 2017, *MNRAS*, 471, 4128
- Pallottini A., et al., 2019, *MNRAS*, 487, 1689
- Pentericci L., et al., 2016, *ApJ*, 829, L11
- Pilbratt G. L., et al., 2010, *A&A*, 518, L1
- Pillepich A., et al., 2018a, *MNRAS*, 473, 4077
- Pillepich A., et al., 2018b, *MNRAS*, 475, 648
- Pineda J. L., Langer W. D., Velusamy T., Goldsmith P. F., 2013, *A&A*, 554, A103
- Pineda J. L., Langer W. D., Goldsmith P. F., 2014, *A&A*, 570, A121
- Pineda J. L., et al., 2017, *ApJ*, 839, 107
- Planck Collaboration et al., 2016, *A&A*, 594, A1
- Popping G., Pérez-Beaupuits J. P., Spaans M., Trager S. C., Somerville R. S., 2014, *MNRAS*, 444, 1301
- Popping G., van Kampen E., Decarli R., Spaans M., Somerville R. S., Trager S. C., 2016, *MNRAS*, 461, 93
- Popping G., Narayanan D., Somerville R. S., Faisst A. L., Krumholz M. R., 2019, *MNRAS*, 482, 4906
- Priddy R. S., McMahon R. G., 2001, *MNRAS*, 324, L17
- Pullen A. R., et al., 2023, *MNRAS*, 521, 6124
- Rawle T. D., et al., 2014, *ApJ*, 783, 59
- Rémy-Ruyer A., et al., 2014, *A&A*, 563, A31
- Requena-Torres M. A., Israel F. P., Okada Y., Güsten R., Stutzki J., Risacher C., Simon R., Zinnecker H., 2016, *A&A*, 589, A28
- Rhoads J. E., et al., 2023, *ApJ*, 942, L14
- Richings A. J., Schaye J., Oppenheimer B. D., 2014a, *MNRAS*, 440, 3349
- Richings A. J., Schaye J., Oppenheimer B. D., 2014b, *MNRAS*, 442, 2780
- Richings A. J., Faucher-Giguère C.-A., Gurvich A. B., Schaye J., Hayward C. C., 2022, *MNRAS*, 517, 1557
- Riechers D. A., et al., 2013, *Nature*, 496, 329
- Rigopoulou D., Pereira-Santaella M., Magdis G. E., Cooray A., Farrah D., Marques-Chaves R., Perez-Fournon I., Riechers D., 2018, *MNRAS*, 473, 20
- Rojas-Ruiz S., et al., 2021, *ApJ*, 920, 150
- Rybak M., et al., 2019, *ApJ*, 876, 112
- Safarzadeh M., Hayward C. C., Ferguson H. C., Somerville R. S., 2016, *ApJ*, 818, 62
- Salim S., Narayanan D., 2020, *ARA&A*, 58, 529
- Sanders D. B., Mazzarella J. M., Kim D.-C., Surace J. A., Soifer B. T., 2003, *AJ*, 126, 1607
- Sargsyan L., et al., 2012, *ApJ*, 755, 171
- Schaerer D., Boone F., Zamojski M., Staguhn J., Dessauges-Zavadsky M., Finkelstein S., Combes F., 2015a, *A&A*, 574, A19
- Schaerer D., et al., 2015b, *A&A*, 576, L2
- Schaerer D., et al., 2020, *A&A*, 643, A3
- Schaerer D., Marques-Chaves R., Barrufet L., Oesch P., Izotov Y. I., Naidu R., Guseva N. G., Brammer G., 2022, *A&A*, 665, L4
- Schouws S., et al., 2022, *ApJ*, 928, 31
- Schouws S., et al., 2023, *ApJ*, 954, 103
- Scoville N. Z., 2013, in Falcón-Barroso J., Knapen J. H., eds, *Secular Evolution of Galaxies*. Cambridge University Press, Cambridge, UK, p. 491
- Scoville N., et al., 2017, *ApJ*, 837, 150
- Semenov V. A., Kravtsov A. V., Gnedin N. Y., 2017, *ApJ*, 845, 133
- Serjeant S., 2012, *MNRAS*, 424, 2429
- Serra P., Doré O., Lagache G., 2016, *ApJ*, 833, 153
- Shao Y., et al., 2017, *ApJ*, 845, 138
- Shao Y., et al., 2019, *ApJ*, 876, 99
- Shen X., Vogelsberger M., Nelson D., Tacchella S., Hernquist L., Springel V., Marinacci F., Torrey P., 2022, *MNRAS*, 510, 5560
- Silva M., Santos M. G., Cooray A., Gong Y., 2015, *ApJ*, 806, 209
- Sklias P., et al., 2014, *A&A*, 561, A149
- Smit R., et al., 2018, *Nature*, 553, 178
- Smith J. D. T., et al., 2017, *ApJ*, 834, 5
- Sobolev V. V., 1957, *Soviet Ast.*, 1, 678
- Sobral D., Matthee J., Darvish B., Schaerer D., Mobasher B., Röttgering H. J. A., Santos S., Hemmati S., 2015, *ApJ*, 808, 139
- Sodroski T. J., Odegard N., Arendt R. G., Dwek E., Weiland J. L., Hauser M. G., Kelsall T., 1997, *ApJ*, 480, 173
- Somerville R. S., Davé R., 2015, *ARA&A*, 53, 51
- Somerville R. S., Primack J. R., 1999, *MNRAS*, 310, 1087
- Somerville R. S., Popping G., Trager S. C., 2015, *MNRAS*, 453, 4338
- Sommovigo L., Ferrara A., Pallottini A., Carniani S., Gallerani S., Decataldo D., 2020, *MNRAS*, 497, 956
- Sommovigo L., Ferrara A., Carniani S., Zanella A., Pallottini A., Gallerani S., Vallini L., 2021, *MNRAS*, 503, 4878
- Sommovigo L., et al., 2022, *MNRAS*, 513, 3122
- Sparre M., Hayward C. C., Feldmann R., Faucher-Giguère C.-A., Muratov A. L., Kereš D., Hopkins P. F., 2017, *MNRAS*, 466, 88
- Spilker J. S., et al., 2016, *ApJ*, 826, 112
- Spitzer L., 1998, *Physical Processes in the Interstellar Medium*. Wiley, doi:10.1002/9783527617722, <https://doi.org/10.1002/9783527617722>
- Stacey G. J., Geis N., Genzel R., Lugten J. B., Poglitsch A., Sternberg A., Townes C. H., 1991, *ApJ*, 373, 423
- Stacey G. J., et al., 2007, in Baker A. J., Glenn J., Harris A. I., Mangum J. G., Yun M. S., eds, *Astronomical Society of the Pacific Conference Series Vol. 375, From Z-Machines to ALMA: (Sub)Millimeter Spectroscopy of Galaxies*. p. 52
- Stacey G. J., Hailey-Dunsheath S., Ferkinhoff C., Nikola T., Parshley S. C., Benford D. J., Staguhn J. G., Fiolet N., 2010, *ApJ*, 724, 957
- Stecher T. P., Williams D. A., 1967, *ApJ*, 149, L29
- Sternberg A., Le Petit F., Roueff E., Le Bourlot J., 2014, *ApJ*, 790, 10
- Suginohara M., Suginohara T., Spergel D. N., 1999, *ApJ*, 512, 547
- Sun G., et al., 2021, *ApJ*, 915, 33
- Sun G., Mas-Ribas L., Chang T.-C., Furlanetto S. R., Mebane R. H., Gonzalez M. O., Parsons J., Trapp A. C., 2023, *ApJ*, 950, 40
- Sutter J., et al., 2019, *ApJ*, 886, 60
- Swinbank A. M., et al., 2010, *Nature*, 464, 733
- Swinbank A. M., et al., 2012, *MNRAS*, 427, 1066
- Swinbank A. M., et al., 2014, *MNRAS*, 438, 1267
- Switzer E. R., et al., 2021, *Journal of Astronomical Telescopes, Instruments, and Systems*, 7
- Symeonidis M., 2016, *MNRAS*, 465, 1401
- Tacchella S., Dekel A., Carollo C. M., Ceverino D., DeGraf C., Lapiner S., Mandelker N., Joel R. P., 2016, *MNRAS*, 457, 2790
- Tacconi L. J., et al., 2018, *ApJ*, 853, 179
- Tadaki K., et al., 2018, *Nature*, 560, 613
- Tadaki K., et al., 2020, *ApJ*, 889, 141
- Takeuchi T. T., Buat V., Burgarella D., 2005, *A&A*, 440, L17
- Tamura Y., et al., 2019, *ApJ*, 874, 27
- Tarantino E., et al., 2021, *ApJ*, 915, 92
- Tielens A. G. G. M., Hollenbach D., 1985, *ApJ*, 291, 722

Tielens A. G. G. M., McKee C. F., Seab C. G., Hollenbach D. J., 1994, *ApJ*, 431, 321

Trayford J. W., et al., 2017, *MNRAS*, 470, 771

Trump J. R., et al., 2023, *ApJ*, 945, 35

Umehata H., et al., 2017, *ApJ*, 834, L16

Vallini L., Gallerani S., Ferrara A., Baek S., 2013, *MNRAS*, 433, 1567

Vallini L., Gallerani S., Ferrara A., Pallottini A., Yue B., 2015, *ApJ*, 813, 36

Vallini L., Pallottini A., Ferrara A., Gallerani S., Sobacchi E., Behrens C., 2018, *MNRAS*, 473, 271

Vallini L., Ferrara A., Pallottini A., Carniani S., Gallerani S., 2021, *MNRAS*, 505, 5543

Valtchanov I., et al., 2011, *MNRAS*, 415, 3473

Vazquez G. A., Leitherer C., 2005, *ApJ*, 621, 695

Velusamy T., Langer W. D., Pineda J. L., Goldsmith P. F., Li D., Yorke H. W., 2010, *A&A*, 521, L18

Venemans B. P., et al., 2012, *ApJ*, 751, L25

Venemans B. P., Walter F., Zschaechner L., Decarli R., Rosa G. D., Findlay J. R., McMahon R. G., Sutherland W. J., 2016, *ApJ*, 816, 37

Venemans B. P., et al., 2017, *ApJ*, 851, L8

Venemans B. P., Neeleman M., Walter F., Novak M., Decarli R., Hennawi J. F., Rix H.-W., 2019, *ApJ*, 874, L30

Venemans B. P., et al., 2020, *ApJ*, 904, 130

Vieira J. D., et al., 2010, *ApJ*, 719, 763

Visbal E., Trac H., Loeb A., 2011, *J. Cosmology Astropart. Phys.*, 2011, 010

Vizgan D., et al., 2022, *ApJ*, 929, 92

Vogelsberger M., et al., 2020, *MNRAS*, 492, 5167

Wagg J., Carilli C. L., Wilner D. J., Cox P., Breuck C. D., Menten K., Riechers D. A., Walter F., 2010, *A&A*, 519, L1

Wagg J., et al., 2012, *ApJ*, 752, L30

Walter F., Riechers D., Cox P., Neri R., Carilli C., Bertoldi F., Weiss A., Maiolino R., 2009, *Nature*, 457, 699

Walter F., et al., 2012, *Nature*, 486, 233

Walter F., et al., 2018, *ApJ*, 869, L22

Wang R., et al., 2013, *ApJ*, 773, 44

Wang R., et al., 2016, *ApJ*, 830, 53

Wang R., et al., 2019, *ApJ*, 887, 40

Wardlow J. L., et al., 2018, *MNRAS*, 479, 3879

Watson D., 2011, *A&A*, 533, A16

Watson D., Christensen L., Knudsen K. K., Richard J., Gallazzi A., Michałowski M. J., 2015, *Nature*, 519, 327

Weingartner J. C., Draine B. T., 2001a, *ApJS*, 134, 263

Weingartner J. C., Draine B. T., 2001b, *ApJ*, 548, 296

Weiß A., et al., 2013, *ApJ*, 767, 88

Welch B., et al., 2023, *ApJ*, 943, 2

Whitaker K. E., Pope A., Cybulski R., Casey C. M., Popping G., Yun M. S., 2017, *ApJ*, 850, 208

Willott C. J., et al., 2013a, *ApJ*, 145, 4

Willott C. J., Omont A., Bergeron J., 2013b, *ApJ*, 770, 13

Willott C. J., Bergeron J., Omont A., 2015a, *ApJ*, 801, 123

Willott C. J., Carilli C. L., Wagg J., Wang R., 2015b, *ApJ*, 807, 180

Willott C. J., Bergeron J., Omont A., 2017, *ApJ*, 850, 108

Wolfire M. G., McKee C. F., Hollenbach D., Tielens A. G. G. M., 2003, *ApJ*, 587, 278

Wolfire M. G., Hollenbach D., McKee C. F., 2010, *ApJ*, 716, 1191

Wong Y. H. V., et al., 2022, *ApJ*, 929, 161

Woody D. P., et al., 2004, in Zmuidzinas J., Holland W. S., Withington S., eds, *Millimeter and Submillimeter Detectors for Astronomy II*. SPIE, doi:10.1117/12.552446, <https://doi.org/10.1117%2F12.552446>

Wooten A., Thompson A., 2009, *Proceedings of the IEEE*, 97, 1463

Yang C., et al., 2019a, *A&A*, 624, A138

Yang J., et al., 2019b, *ApJ*, 880, 153

Yang S., Somerville R. S., Pullen A. R., Popping G., Breyse P. C., Maniyar A. S., 2021, *ApJ*, 911, 132

Yang S., Popping G., Somerville R. S., Pullen A. R., Breyse P. C., Maniyar A. S., 2022, *ApJ*, 929, 140

Younger J. D., Hayward C. C., Narayanan D., Cox T. J., Hernquist L., Jonsson P., 2009, *MNRAS: Letters*, 396, L66

Yue B., Ferrara A., 2019, *MNRAS*, 490, 1928

Yue M., et al., 2021, *ApJ*, 917, 99

Zanella A., et al., 2018, *MNRAS*, 481, 1976

Zavala J. A., et al., 2021, *ApJ*, 909, 165

Zhu Y.-N., Wu H., Cao C., Li H.-N., 2008, *ApJ*, 686, 155

Zubko V., Dwek E., Arendt R. G., 2004, *ApJS*, 152, 211

da Cunha E., et al., 2013, *ApJ*, 766, 13

da Cunha E., et al., 2021, *ApJ*, 919, 30

van Dishoeck E. F., Black J. H., 1986, *ApJS*, 62, 109

van Hoof P. A. M., Weingartner J. C., Martin P. G., Volk K., Ferland G. J., 2004, *MNRAS*, 350, 1330

APPENDIX A: THE RADIATIVE COOLING RATE OF GAS FROM THE $[C_{\text{II}}]$ FINE STRUCTURE TRANSITION — I. THE GENERAL CASE

The C^+ ion has two fine structure levels in the ground electronic state. The radiative cooling rate of gas from the $[C_{\text{II}}]$ transition can therefore be calculated by solving a classical two-level problem (Goldsmith et al. 2012).

The cooling rate in $\text{erg s}^{-1} \text{cm}^{-3}$ can be written as

$$\Lambda_{[C_{\text{II}}]} = [A_{\text{ul}}n_{\text{u}} + B_{\text{ul}}n_{\text{u}}U(T^{\text{b}}) - B_{\text{lu}}n_{\text{l}}U(T^{\text{b}})]E_{\text{ul}} \quad (\text{A1})$$

where n_{u} and n_{l} represent the densities of the upper ($^2P_{3/2}$) and lower level ($^2P_{1/2}$) C^+ ions (cm^{-3}) that result from the combination of collisional and radiative processes. A_{ul} , B_{ul} and B_{lu} in the above equation represent the Einstein coefficients for spontaneous emission (s^{-1}), stimulated emission ($\text{erg}^{-1} \text{s}^{-2} \text{cm}^3$) and stimulated absorption ($\text{erg}^{-1} \text{s}^{-2} \text{cm}^3$), respectively. $E_{\text{ul}} (\equiv h\nu_{[C_{\text{II}}]}$, where $\nu_{[C_{\text{II}}]} = 1900.5 \text{ GHz}$) represents the transition energy of the $[C_{\text{II}}]$ line. $U(T^{\text{b}})$ indicates the radiative energy density at $\nu_{[C_{\text{II}}]}$ and T^{b} is the brightness temperature of the background radiation field. The source of the background radiation may be the CMB and/or the thermal emission of warm dust.

$\Lambda_{[C_{\text{II}}]}$ can be rewritten as a function of the excitation (or spin) temperature for the transition (T^{ex}) and the temperature of the background radiation field (T^{b}). The excitation temperature is defined by the relative populations of the upper and lower levels through

$$\frac{n_{\text{u}}}{n_{\text{l}}} \equiv \frac{g_{\text{u}}}{g_{\text{l}}} e^{-T^*/T^{\text{ex}}}, \quad (\text{A2})$$

where $T^* = h\nu_{[C_{\text{II}}]}/k_{\text{B}} = 91.8 \text{ K}$ is the equivalent temperature of the $[C_{\text{II}}]$ transition, and $g_{\text{u}} = 4$ ($g_{\text{l}} = 2$) is the statistical weight of the upper (lower)-level state. Given the relationships between the Einstein coefficients, *i.e.*

$$B_{\text{lu}} = (g_{\text{u}}/g_{\text{l}})B_{\text{ul}} \quad (\text{A3})$$

and

$$\frac{A_{\text{ul}}}{B_{\text{ul}}} = \frac{8\pi h\nu_{[C_{\text{II}}]}^3}{c^3}, \quad (\text{A4})$$

and substituting equation (A2) into equation (A1), we obtain

$$\Lambda_{[C_{\text{II}}]} = n_{\text{u}}A_{\text{ul}}h\nu_{[C_{\text{II}}]} \left[1 - \frac{e^{(T^*/T^{\text{ex}})} - 1}{e^{(T^*/T^{\text{b}})} - 1} \right]. \quad (\text{A5})$$

Neglecting background radiation (*i.e.* $T^{\text{b}} \approx 0$), we get

$$\Lambda_{[C_{\text{II}}]} = n_{\text{u}}A_{\text{ul}}h\nu_{[C_{\text{II}}]}, \quad (\text{A6})$$

which is the usual expression for the cooling rate. The term in the square brackets in equation (A5) is the background correction term

for attenuation (see [da Cunha et al. 2013](#) for the details). From equation (A2), we have

$$n_u = n_{C^+} \left[1 + \left(\frac{g_l}{g_u} \right) e^{T^*/T^{\text{ex}}} \right]^{-1}. \quad (\text{A7})$$

By substituting equation (A7) into equation (A5), we then obtain the analytic expression for the $[C_{\text{II}}]$ cooling rate when a background is included,

$$\Lambda_{[C_{\text{II}}]} = n_{C^+} A_{\text{ul}} h\nu_{[C_{\text{II}}]} \Psi(T^{\text{ex}}, T^{\text{b}}), \quad (\text{A8})$$

where

$$\Psi(T^{\text{ex}}, T^{\text{b}}) = \left[1 - \frac{e^{(T^*/T^{\text{ex}})} - 1}{e^{(T^*/T^{\text{b}})} - 1} \right] \left[1 + \left(\frac{g_l}{g_u} \right) e^{T^*/T^{\text{ex}}} \right]^{-1}. \quad (\text{A9})$$

Equations (A8)-(A9) indicates that one can derive $\Lambda_{[C_{\text{II}}]}$ by solving for T^{ex} .

APPENDIX B: EXCITATION TEMPERATURE FOR THE $[C_{\text{II}}]$ TRANSITION

Here we present the analytic expression for the excitation temperature (T^{ex}) for the $[C_{\text{II}}]$ transition.

The rate equation that determines the upper and lower level C^+ densities, n_u and n_l , includes both collisional and radiative processes, and is

$$n_u [A_{\text{ul}} + B_{\text{ul}} U(T^{\text{b}}) + C_{\text{ul}}] = n_l [B_{\text{lu}} U(T^{\text{b}}) + C_{\text{lu}}], \quad (\text{B1})$$

where C_{ul} (C_{lu}) represents the collisional de-excitation (excitation) rate (s^{-1}). The Einstein coefficients, A_{ul} , B_{ul} and B_{lu} , are related by equations (A3) and (A4). For a single collision partner, the collision rates are equal to the rate coefficients ($\text{cm}^3 \text{s}^{-1}$) times the density n_X of that collision partner ($X = e^-, \text{H}_1$ or H_2), *i.e.*

$$C_{\text{ul}} = R_{\text{ul}}^X n_X \quad \text{and} \quad C_{\text{lu}} = R_{\text{lu}}^X n_X, \quad (\text{B2})$$

where R_{ul}^X (R_{lu}^X) is the downward (upward) rate coefficient for collision partner X . The two rate coefficients are related by detailed balance

$$R_{\text{lu}}^X / R_{\text{ul}}^X = (g_u / g_l) e^{-T^*/T}, \quad (\text{B3})$$

where T is the kinetic temperature of gas. By substituting equations (A2)-(A4), (B1)-(B3) into equation (B1) and through rearrangement, we obtain the analytic expression for the excitation temperature

$$e^{T^*/T^{\text{ex}}} = \frac{(1+G)A_{\text{ul}} + n_X R_{\text{ul}}^X}{G A_{\text{ul}} + n_X R_{\text{ul}}^X e^{-T^*/T}} \quad (\text{B4})$$

where we define

$$G = \frac{1}{e^{T^*/T^{\text{b}}} - 1} \quad (\text{B5})$$

following [Goldsmith et al. \(2012\)](#). For the $[C_{\text{II}}]$ transition, we have (see *e.g.* [Suginohara et al. 1999](#); [Goldsmith et al. 2012](#))

$$A_{\text{ul}} = 2.36 \times 10^{-6} \text{ s}^{-1}, \quad (\text{B6})$$

$$R_{\text{ul}}^{e^-}(T) = 8.7 \times 10^{-8} (T/2000)^{-0.37} \text{ cm}^3 \text{ s}^{-1}, \quad (\text{B7})$$

$$R_{\text{ul}}^{\text{H}_1}(T) = 4.0 \times 10^{-11} (16 + 0.35T^{0.5} + 48T^{-1}) \text{ cm}^3 \text{ s}^{-1}, \quad (\text{B8})$$

and

$$R_{\text{ul}}^{\text{H}_2}(T) = 3.8 \times 10^{-10} (T/100)^{0.14} \text{ cm}^3 \text{ s}^{-1}. \quad (\text{B9})$$

We can see from equations (B4) and (B5) that for no background

radiation (*i.e.* $T^{\text{b}} \simeq 0$) and high gas density (*i.e.* $n_X \gg A_{\text{ul}}/R_{\text{ul}}^X$), $G \rightarrow 0$ and $T^{\text{ex}} \rightarrow T$. In this case, T^{ex} (and hence the C^+ level populations) is set totally by the kinetic temperature of gas. The impact of background radiation on T^{ex} can be important in low-density environments (*i.e.* $n_X \ll A_{\text{ul}}/R_{\text{ul}}^X$).

APPENDIX C: THE STRÖMGREN DEPTH OF A PLANE-PARALLEL SLAB

The Strömgren depth (l_s) can be derived by equating the ionizing photon rate (\dot{N}_{ion}) to the hydrogen recombination rate (\dot{N}_{rec}) in the H^+ region. \dot{N}_{ion} can be expressed as

$$\dot{N}_{\text{ion}} = F_{\text{ion}} A, \quad (\text{C1})$$

where

$$F_{\text{ion}} = \int_{\nu_L}^{\infty} \frac{F_\nu}{h\nu} d\nu, \quad (\text{C2})$$

is the ionizing photon flux ($\text{cm}^{-2} \text{s}^{-1}$) and A is the surface area of the slab. F_ν indicates the specific energy flux ($\text{cm}^{-2} \text{s}^{-1} \text{Hz}^{-1}$) at frequency ν and $\nu_L = 3.2 \times 10^6 \text{ GHz}$ is the frequency corresponding to the ionization energy of hydrogen, *i.e.* $h\nu_L = 13.6 \text{ eV}$. \dot{N}_{rec} can be expressed as

$$\dot{N}_{\text{rec}} = n_e n_p \alpha_B l_s dA \approx n_{\text{H}}^2 \alpha_B l_s A, \quad (\text{C3})$$

where $\alpha_B = 2.6 \times 10^{-13} \text{ cm}^3 \text{ s}^{-1}$ is the Case-B recombination coefficient at temperature $T \approx 10^4 \text{ K}$. Combining equation (C1) and equation (C3), we have

$$l_s = \frac{F_{\text{ion}}}{n_{\text{H}}^2 \alpha_B}. \quad (\text{C4})$$

Hence, the gas column density at the Strömgren depth is

$$N_s = n_{\text{H}} l_s = \frac{F_{\text{ion}}}{n_{\text{H}} \alpha_B} = \frac{Uc}{\alpha_B} \approx 10^{23} U \text{ cm}^{-2}, \quad (\text{C5})$$

where

$$U = \frac{F_{\text{ion}}}{n_{\text{H}} c} = \frac{n_\gamma}{n_{\text{H}}} \quad (\text{C6})$$

is the ionizing photon-to-gas density ratio.

APPENDIX D: THE RADIATIVE COOLING RATE OF GAS FROM THE $[C_{\text{II}}]$ FINE STRUCTURE TRANSITION — II. THE PLANE-PARALLEL SLAB MODEL

Following Appendix A, we present specifically here an analytic expression for the gas cooling rate via $[C_{\text{II}}]$ line in the H^+ (Zone I) and H_1 regions (Zone II) of a plane-parallel slab. The superscript “(1)” and “(2)” in the following equations indicate the properties of gas in Zone I and II, respectively.

H^+ region

For H^+ region (Zone I), where $T^{(1)} \approx 10^4 \text{ K}$ (hence $e^{-T^*/T^{(1)}} \approx 1$) and the main collision partner of C^+ ions is e^- , we can rewrite equation (B4) to be

$$e^{T^*/T^{\text{ex}}} = \frac{A_{\text{ul}} + n_e^{(1)} R_{\text{ul}}^{e^-}(T^{(1)})}{n_e^{(1)} R_{\text{ul}}^{e^-}(T^{(1)})}, \quad (\text{D1})$$

where we neglect the effect of background field. For densities below the critical one (i.e. $n_{e^-}^{(1)} \lesssim A_{ul}/R_{ul}^{e^-}$),

$$e^{T^*/T^{\text{ex}}} \approx \frac{A_{ul}}{n_{e^-}^{(1)} R_{ul}^{e^-}(T^{(1)})}. \quad (\text{D2})$$

Given $A_{ul} = 2.36 \times 10^{-6} \text{ s}^{-1}$ and $R_{ul}^{e^-}(T^{(1)}) \approx 5 \times 10^{-8} \text{ cm}^3 \text{ s}^{-1}$ (equation (B7)), equation (D2) can be rewritten as

$$e^{T^*/T^{\text{ex}}} \approx \frac{50}{n_{e^-}^{(1)}}. \quad (\text{D3})$$

Substituting equation (D3) into equation (A9) gives

$$\Psi^{(1)} \approx \left[1 + \left(\frac{g_l}{g_u} \right) e^{T^*/T^{\text{ex}}} \right]^{-1} \approx \frac{n_{e^-}^{(1)}}{25}. \quad (\text{D4})$$

Finally, by substituting equation (D4) into equation (A8), we obtain the expression for the [C_{II}] cooling rate in H⁺ region

$$\begin{aligned} \Lambda_{[\text{CII}]}^{(1)} &= n_{\text{C}^+}^{(1)} A_{ul} h_{\text{P}\nu}[\text{CII}] \Psi^{(1)} \\ &= \left[A_{ul} h_{\text{P}\nu}[\text{CII}] \left(\frac{g_u}{g_l} \right) e^{-T^*/T^{\text{ex}}} \right] n_{\text{C}^+}^{(1)} \\ &\approx 10^{-21} n_{\text{C}^+}^{(1)} n_{e^-}^{(1)} \text{ erg s}^{-1} \text{ cm}^{-3}. \end{aligned} \quad (\text{D5})$$

H_I region

Now consider the [C_{II}] cooling rate in H_I region (Zone II), where $T^{(2)} \approx 100 \text{ K}$ (hence $e^{-T^*/T^{(2)}} \approx \frac{2}{5}$) and the main collision partner of C⁺ ions is H_I. In this case, equation (B5) can be rewritten as

$$\begin{aligned} e^{T^*/T^{\text{ex}}} &= \frac{(1+G)A_{ul} + n_{\text{HI}}^{(2)} R_{ul}^{\text{HI}}}{GA_{ul} + n_{\text{HI}}^{(2)} R_{ul}^{\text{HI}} e^{-T^*/T^{(2)}}} \\ &\approx \frac{1}{G + \frac{2}{5} n_{\text{HI}}^{(2)} (R_{ul}^{\text{HI}}/A_{ul})}. \end{aligned} \quad (\text{D6})$$

Given $R_{ul}^{\text{HI}}(T^{(2)}) \approx 8 \times 10^{-10} \text{ cm}^3 \text{ s}^{-1}$ (equation (B8)), we have

$$e^{T^*/T^{\text{ex}}} \approx \frac{1}{G + n_{\text{HI}}^{(2)}/7400}. \quad (\text{D7})$$

For the case when background radiation is unimportant (e.g. low- z CMB), $T^b \rightarrow 0$ and thus $G \rightarrow 0$, we get

$$e^{T^*/T^{\text{ex}}} \approx 7400/n_{\text{HI}}^{(2)}. \quad (\text{D8})$$

Substituting equation (D8) into equation (A9) and equation (A8) gives

$$\Psi^{(2)}(T^b = 0) \approx \left[1 + \left(\frac{g_l}{g_u} \right) e^{T^*/T^{\text{ex}}} \right]^{-1} \approx 2.7 \times 10^{-4} n_{\text{HI}}^{(2)} \quad (\text{D9})$$

and

$$\begin{aligned} \Lambda_{[\text{CII}]}^{(2)}(T^b = 0) &= n_{\text{C}^+}^{(2)} A_{ul} h_{\text{P}\nu}[\text{CII}] \Psi^{(2)}(T^b = 0) \\ &= \left[A_{ul} h_{\text{P}\nu}[\text{CII}] \left(\frac{g_u}{g_l} \right) e^{-T^*/T^{\text{ex}}} \right] n_{\text{C}^+}^{(2)} \\ &\approx 10^{-23} n_{\text{C}^+}^{(2)} n_{\text{HI}}^{(2)} \text{ erg s}^{-1} \text{ cm}^{-3}. \end{aligned} \quad (\text{D10})$$

Equation (D10) is the expression for the [C_{II}] cooling rate in H_I region when background radiation is neglected.

Taking into account background radiation, equation (A9) can be expressed as

$$\Psi^{(2)} = \eta^b (n_u/n_{\text{C}^+}), \quad (\text{D11})$$

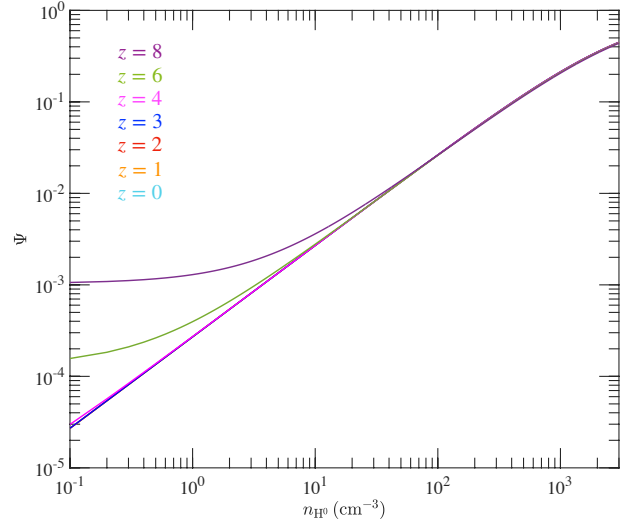


Figure D1. The relation between Ψ (equation D12) and gas density for H_I gas ($T = 100 \text{ K}$) at different redshifts. Ψ is unaffected by the CMB at redshift $0 \leq z \leq 4$. At $z = 6 - 8$, Ψ (and hence the [C_{II}] cooling rate) can be much affected by the CMB in low-density gas.

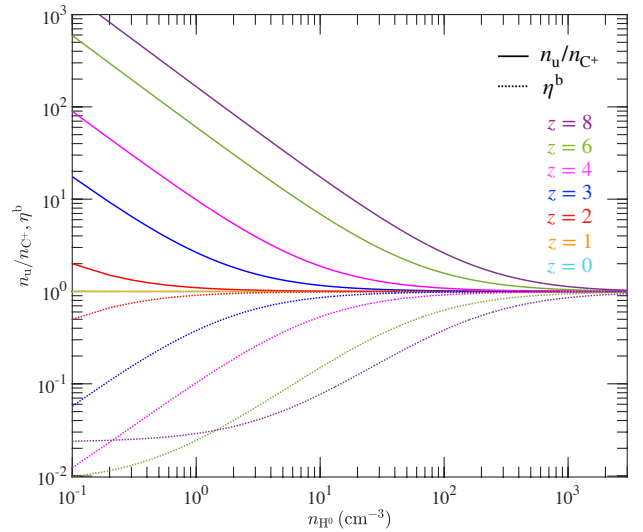


Figure D2. Solid (dotted) lines indicate the relation between $\eta^b (n_u/n_{\text{C}^+})$ and gas density for H_I gas ($T = 100 \text{ K}$) at different redshifts. At a given redshift, both the effects of CMB heating and attenuation increases with decreasing gas density.

where

$$\eta^b \equiv 1 - \frac{e^{(T^*/T^{\text{ex}})} - 1}{e^{(T^*/T^b)} - 1} \approx \frac{G + n_{\text{HI}}^{(2)}/(7400 G)}{1 + n_{\text{HI}}^{(2)}/(7400 G)} \quad (\text{D12})$$

is the background attenuation term and

$$\frac{n_u}{n_{\text{C}^+}} = \left[1 + \left(\frac{g_l}{g_u} \right) e^{T^*/T^{\text{ex}}} \right]^{-1} \approx \left[1 + \frac{1}{2(G + n_{\text{HI}}^{(2)}/7400)} \right]^{-1}. \quad (\text{D13})$$

Equation (D13) indicates that background radiation (e.g. the CMB) leads to increased upper level ($^2P_{3/2}$) population of the [C_{II}] transition ('background heating'). Using the above equations, we obtain

the level of change of the $[\text{C}_{\text{II}}]$ cooling rate by the CMB at redshift z ,

$$\mathcal{R} \equiv \frac{\Lambda_{[\text{C}_{\text{II}}]}^{(2)}(T^{\text{CMB}}(z))}{\Lambda_{[\text{C}_{\text{II}}]}^{(2)}(T^{\text{b}}=0)} = \frac{\Psi^{(2)}(T^{\text{CMB}}(z))}{\Psi^{(2)}(T^{\text{b}}=0)}$$

$$\approx \left[\frac{G + n_{\text{H}_1}^{(2)}/(7400 G)}{1 + n_{\text{H}_1}^{(2)}/(7400 G)} \right] \left[\frac{2}{7400 n_{\text{H}_1}^{(2)}} + \frac{1}{7400 G/n_{\text{H}_1}^{(2)} + 1} \right]^{-1}. \quad (\text{D14})$$

We show in Fig. D1 the relation between $\Psi^{(2)}$ (equation D11) and gas density for H_1 gas ($T^{(2)} \approx 100$ K) at different redshifts ($z = 0-8$), where we account for the effects of the CMB background. It can be seen that $\Psi^{(2)}$ shows almost no redshift evolution at $z = 0-4$ over the wide density range being considered. At higher redshifts, $\Psi^{(2)}$ (and hence $\Lambda_{[\text{C}_{\text{II}}]}^{(2)}$) is raised by the CMB in low-density gas. At $z = 6$ ($z = 8$), for example, $\Psi^{(2)}$ appears to be much higher than that of the lower redshifts at densities below $\sim 1 \text{ cm}^{-3}$ ($\sim 10 \text{ cm}^{-3}$).

It should be noted, however, that although the net effect of CMB heating and attenuation on the $[\text{C}_{\text{II}}]$ cooling rate is negligible except for the low-density gas at $z \gtrsim 6$, their own effect can be prominent at various densities and at lower redshifts. This can be seen from Fig. D2, where we explicitly show how $n_{\text{u}}/n_{\text{C}^+}$ (indicating heating) and η^{b} (indicating attenuation) depend on gas density for H_1 gas ($T^{(2)} \approx 100$ K) at different redshifts (*c.f.* Kohandel et al. 2019). Both the effects of CMB heating and attenuation becomes stronger with decreasing gas density, but they almost cancel out each other at above 0.1 cm^{-3} at $z = 0-4$ (and at higher densities at $z = 6-8$). As a result, the $[\text{C}_{\text{II}}]$ cooling rate becomes almost unaffected by the CMB in that regime.

APPENDIX E: CARBON IONIZATION IN THE H^+ REGION

Here we present the analytic expression for the abundance of C^+ ions in the H^+ region. Consider the carbon ionization equilibrium equation:

$$\Gamma_{\text{C}} n_{\text{C}^+} = \alpha_{\text{C}} n_{\text{C}^{2+}} n_{\text{e}^-}, \quad (\text{E1})$$

where we only account for the $\text{C}^+ \Leftrightarrow \text{C}^{2+}$ equilibrium. Γ_{C} is the optically thin carbon photo-ionization rate (s^{-1}) and $\alpha_{\text{C}} = 6.02 \times 10^{-12} \text{ cm}^3 \text{ s}^{-1}$ is the recombination coefficient (Nahar & Pradhan 1997). Given $n_{\text{C}^+} = x_{\text{C}^+} n_{\text{C}}$ and $n_{\text{C}^{2+}} = (1 - x_{\text{C}^+}) n_{\text{C}}$, we can rewrite equation (E1) to be

$$x_{\text{C}^+} = \left(1 + \frac{\Gamma_{\text{C}}}{n_{\text{e}^-} \alpha_{\text{C}}} \right)^{-1} \approx \frac{n_{\text{e}^-} \alpha_{\text{C}}}{\Gamma_{\text{C}}}. \quad (\text{E2})$$

Following Ferrara et al. (2019), we have

$$\Gamma_{\text{C}} = F_{\text{ion}} \bar{\sigma}_{\text{C}} = U n_{\text{H}} c \bar{\sigma}_{\text{C}}, \quad (\text{E3})$$

where $\bar{\sigma}_{\text{C}} \approx 4 \times 10^{-18} \text{ cm}^2$ is the flux-weighted carbon photo-ionization cross section (Spitzer 1998). Substituting equation (E3) into equation (E2) and given $n_{\text{e}^-} \approx n_{\text{H}}$ for the H^+ region, we then get

$$x_{\text{C}^+} \approx \frac{\alpha_{\text{C}}}{U c \bar{\sigma}_{\text{C}}} \propto U^{-1}. \quad (\text{E4})$$

Hence, x_{C^+} is inversely proportional to U .

APPENDIX F: $[\text{C}_{\text{II}}]$ LUMINOSITY OF A UNIFORM SPHERICAL GAS CLOUD

Here we derive the specific $[\text{C}_{\text{II}}]$ cooling rate ($\text{erg cm}^3 \text{ s}^{-1}$) for a spherical uniform cloud ($\bar{\epsilon}_{[\text{C}_{\text{II}}], \text{cl}}$). For the case where the cloud is fully photo-ionized by the external UV radiation (*i.e.* $l_{\text{s}} \geq R_{\text{cl}}$), the luminosity of the cloud ($L_{[\text{C}_{\text{II}}], \text{cl}}$) can be expressed as

$$L_{[\text{C}_{\text{II}}], \text{cl}} = 4\pi \int_0^{R_{\text{cl}}} \Lambda_{[\text{C}_{\text{II}}]}^{(1)} r^2 dr. \quad (\text{F1})$$

Substituting equation (D5) into the above equation, we get

$$L_{[\text{C}_{\text{II}}], \text{cl}} = \left(\frac{4\pi}{3} n_{\text{H}} R_{\text{cl}}^3 \right) n_{\text{H}} \mathcal{A}_{\text{C}} \left[h_{\text{P}} \nu_{[\text{C}_{\text{II}}]} \left(\frac{g_{\text{u}}}{g_{\text{l}}} \right) R_{\text{ul}}^{\text{e}^-} (T^{(1)}) x_{\text{C}^+}^{(1)} \right]. \quad (\text{F2})$$

For the case where H_1 region forms in the cloud (*i.e.* $l_{\text{s}} < R_{\text{cl}}$), $L_{[\text{C}_{\text{II}}], \text{cl}}$ can be expressed as

$$L_{[\text{C}_{\text{II}}], \text{cl}} = 4\pi \left[\int_{R_{\text{cl}}-l_{\text{s}}}^{R_{\text{cl}}} \Lambda_{[\text{C}_{\text{II}}]}^{(1)} r^2 dr + \int_{\max(0, R_{\text{cl}}-l_{\text{F}})}^{R_{\text{cl}}-l_{\text{s}}} \Lambda_{[\text{C}_{\text{II}}]}^{(2)} r^2 dr \right], \quad (\text{F3})$$

where the first and second terms on the right-hand side of the equation correspond to the $[\text{C}_{\text{II}}]$ emission from H^+ (Zone I) and H_1 regions (Zone II), respectively. By substituting equation (D5) into the first term and equation (D13) into the second term, we can rewrite the above equation to be

$$L_{[\text{C}_{\text{II}}], \text{cl}} = f_{[\text{C}_{\text{II}}], \text{cl}} \left(\frac{4\pi}{3} n_{\text{H}} R_{\text{cl}}^3 \right) n_{\text{H}} \mathcal{A}_{\text{C}} \times h_{\text{P}} \nu_{[\text{C}_{\text{II}}]} \left(\frac{g_{\text{u}}}{g_{\text{l}}} \right) \frac{\int_{R_{\text{cl}}-l_{\text{s}}}^{R_{\text{cl}}} x_{\text{C}^+}^{(1)} R_{\text{ul}}^{\text{e}^-} r^2 dr + \int_{\max(0, R_{\text{cl}}-l_{\text{F}})}^{R_{\text{cl}}-l_{\text{s}}} (2/5) R_{\text{ul}}^{\text{H}_1} r^2 dr}{\int_{\max(0, R_{\text{cl}}-l_{\text{F}})}^{R_{\text{cl}}} r^2 dr}, \quad (\text{F4})$$

where $f_{[\text{C}_{\text{II}}], \text{cl}}$ represents the total fraction of gas mass in H^+ or H_1 regions (Zone I + Zone II). Combining equation (F2) and equation (F4), and substituting $M_{\text{cl}} = \frac{4}{3} \pi R_{\text{cl}}^3 (\mu_{\text{H}} m_{\text{H}} n_{\text{H}})$ into the equations, we obtain

$$L_{[\text{C}_{\text{II}}], \text{cl}} = f_{[\text{C}_{\text{II}}], \text{cl}} \left(\frac{M_{\text{cl}}}{\mu_{\text{H}} m_{\text{H}}} \right) n_{\text{H}} \mathcal{A}_{\text{C}} \bar{\epsilon}_{[\text{C}_{\text{II}}], \text{cl}}, \quad (\text{F5})$$

where

$$f_{[\text{C}_{\text{II}}], \text{cl}} = \begin{cases} 1 & (\text{if } l_{\text{F}} \geq R_{\text{cl}}) \\ 3 \int_{R_{\text{cl}}-l_{\text{s}}}^{R_{\text{cl}}} (r/R_{\text{cl}})^2 d(r/R_{\text{cl}}) & (\text{if } l_{\text{F}} < R_{\text{cl}}) \end{cases} \quad (\text{F6})$$

and

$$\bar{\epsilon}_{[\text{C}_{\text{II}}], \text{cl}} = h_{\text{P}} \nu_{[\text{C}_{\text{II}}]} \left(\frac{g_{\text{u}}}{g_{\text{l}}} \right) \times \begin{cases} R_{\text{ul}}^{\text{e}^-} (T^{(1)}) x_{\text{C}^+}^{(1)} & (\text{if } l_{\text{s}} \geq R_{\text{cl}}) \\ \frac{\int_{R_{\text{cl}}-l_{\text{s}}}^{R_{\text{cl}}} x_{\text{C}^+}^{(1)} R_{\text{ul}}^{\text{e}^-} r^2 dr + \int_{\max(0, R_{\text{cl}}-l_{\text{F}})}^{R_{\text{cl}}-l_{\text{s}}} \left(\frac{2}{5} \right) R_{\text{ul}}^{\text{H}_1} r^2 dr}{\int_{\max(0, R_{\text{cl}}-l_{\text{F}})}^{R_{\text{cl}}} r^2 dr} & (\text{if } l_{\text{s}} < R_{\text{cl}}) \end{cases} \quad (\text{F7})$$

Equation (F7) is the analytic expression for the specific $[\text{C}_{\text{II}}]$ cooling rate for a uniform spherical gas cloud.

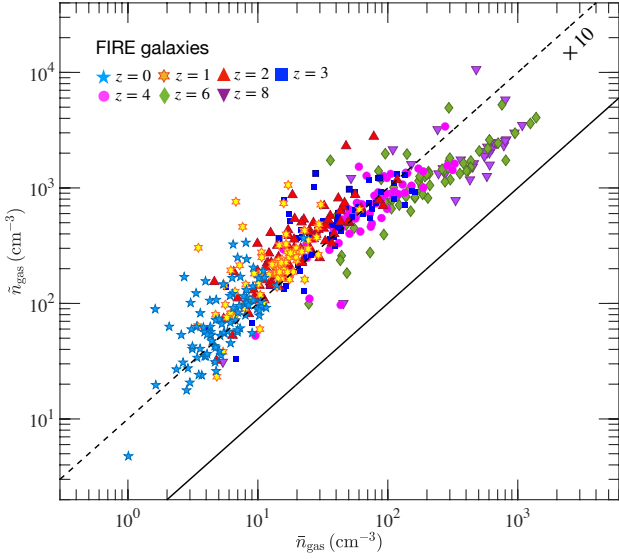


Figure G1. The relation between the [C_{II}] luminosity-weighted *median* gas density (\bar{n}_{gas}) and the [C_{II}] luminosity-weighted *mean* gas density (\tilde{n}_{gas}) of the FIRE galaxy sample at $z = 0 - 8$. The solid black line indicates the one-to-one relationship, whilst the dashed black line indicates the relation $\tilde{n}_{\text{gas}} = 10\bar{n}_{\text{gas}}$. \tilde{n}_{gas} is systematically higher than \bar{n}_{gas} .

APPENDIX G: LUMINOSITY-WEIGHTED GAS DENSITY OF GALAXIES

In Fig. G1, we show the relation between the [C_{II}] luminosity-weighted *median* gas density (\bar{n}_{gas}) and the [C_{II}] luminosity-weighted *mean* gas density (\tilde{n}_{gas}) of the FIRE sample at different redshifts ($z = 0 - 8$). It can be seen from the figure that the latter is systematically higher.

The reason for this result is that the [C_{II}] luminosity-weighted PDF of gas density (n_{H}) of the galaxies resembles a lognormal function (see Fig. G2 for an example), showing an elongated tail at high density end. Consider a lognormal function with two parameters μ and σ , *i.e.*

$$P(n_{\text{H}}; \mu, \sigma) = \frac{1}{n_{\text{H}}\sqrt{2\pi}\sigma} e^{-\frac{(\ln(n_{\text{H}}) - \mu)^2}{2\sigma^2}}. \quad (\text{G1})$$

The cumulative distribution function (CDF) for a lognormal distribution is

$$C(n_{\text{H}}; \mu, \sigma) \equiv \int_{-\infty}^{n_{\text{H}}} P(x; \mu, \sigma) dx = \frac{1}{2} \left[1 + \operatorname{erf} \left(\frac{\ln(n_{\text{H}}) - \mu}{\sqrt{2}\sigma} \right) \right], \quad (\text{G2})$$

where erf is the error function. It is easy to show that the mean density (\bar{n}_{H}) of a lognormal distribution is

$$\bar{n}_{\text{H}} = \int_{-\infty}^{\infty} xP(x; \mu, \sigma) dx = \int_{-\infty}^{\infty} \frac{1}{\sqrt{2\pi}\sigma} e^{-\frac{(\ln(x) - \mu)^2}{2\sigma^2}} dx = e^{\mu + \frac{\sigma^2}{2}}, \quad (\text{G3})$$

whereas the median density (\tilde{n}_{H}), *i.e.* the density at which $C(n_{\text{H}}; \mu, \sigma) = \frac{1}{2}$, is

$$\tilde{n}_{\text{H}} = e^{\mu}. \quad (\text{G4})$$

Hence, \tilde{n}_{H} is higher than \bar{n}_{H} by a factor of $\tilde{n}_{\text{H}}/\bar{n}_{\text{H}} = e^{-\frac{\sigma^2}{2}}$.

In Fig. G2, we show the luminosity-weighted density PDF of two

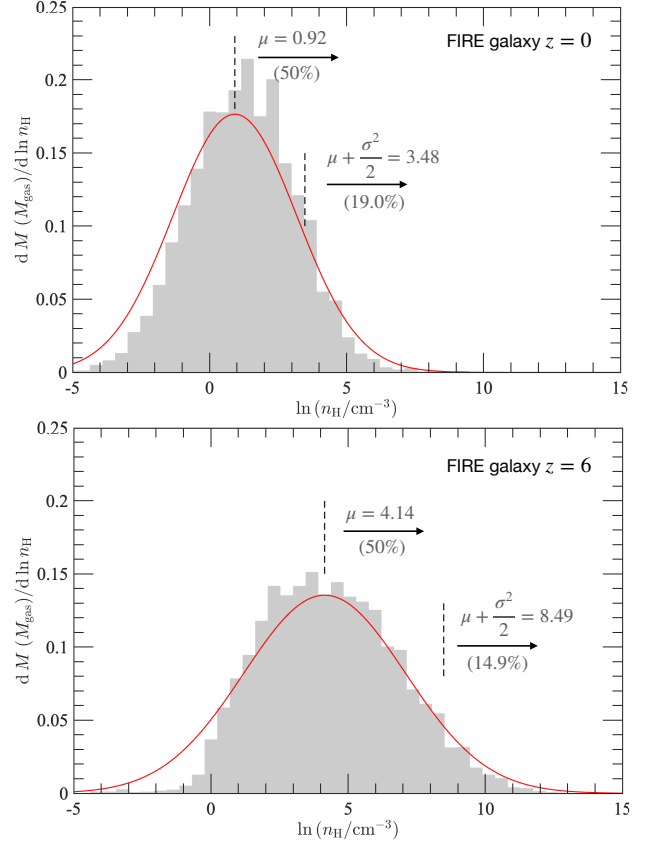


Figure G2. The [C_{II}]-luminosity-weighted PDF of gas density of two selected FIRE galaxies at $z = 0$ (*upper panel*) and $z = 6$ (*lower panel*) and the best-fit lognormal function (equation G1) to the PDF. In each panel, shaded grey area represents the original PDF whereas solid red line indicates the best-fit lognormal function. The luminosity-weighted mean gas density (\tilde{n}_{H} ; marked by the vertical dashed line on the right) of the galaxies is higher than the luminosity-weighted median density (\bar{n}_{H} ; marked by the vertical dashed line on the left).

selected FIRE galaxies at $z = 6$ (*lower panel*) and $z = 0$ (*upper panel*) as well as the best-fit lognormal function to their PDF (note: the same galaxies as for Fig. 11) as an example. The luminosity-weighted median gas density \bar{n}_{gas} of the $z = 0$ ($z = 6$) galaxy is 2.5 cm^{-3} (25.1 cm^{-3}), whereas its luminosity-weighted mean density \tilde{n}_{gas} is 4.2 cm^{-3} (754.4 cm^{-3}). For the $z = 6$ ($z = 0$) galaxy, only 19.0% (14.9%) of the total [C_{II}] luminosity originates from the gas at density above \tilde{n}_{gas} . It is therefore not statistically representative for the bulk of the gas in galaxies emitting [C_{II}].

APPENDIX H: LUMINOSITY-WEIGHTED GAS METALLICITY OF GALAXIES

In Fig. H1, we show the relation between the luminosity-weighted median (\bar{Z}_{gas}) and the luminosity-weighted mean gas metallicity (\tilde{Z}_{gas}) of the FIRE galaxy sample at $z = 0 - 8$. \bar{Z}_{gas} and \tilde{Z}_{gas} are very close to each other. The former is higher by only 0.02 dex (4%) on average.

Both \bar{Z}_{gas} and \tilde{Z}_{gas} of the galaxies are similar to their mass-weighted gas metallicity ($\bar{Z}_{\text{gas, MW}}$). In the same figure, we show the \bar{Z}_{gas} vs. $\bar{Z}_{\text{gas, MW}}$ relation for the FIRE sample. \bar{Z}_{gas} is on average higher than $\bar{Z}_{\text{gas, MW}}$ by 0.10 dex (20%).

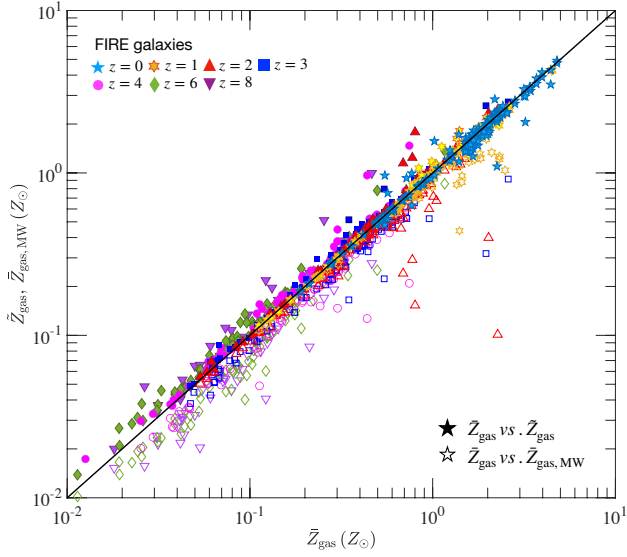


Figure H1. The \bar{Z}_{gas} vs. \bar{Z}_{gas} relation and the \bar{Z}_{gas} (filled coloured symbols) vs. $\bar{Z}_{\text{gas, MW}}$ (empty symbols) relation of the FIRE sample at $z = 0 - 8$, where \bar{Z}_{gas} , \bar{Z}_{gas} and $\bar{Z}_{\text{gas, MW}}$ represent the luminosity-weighted median, luminosity-weighted mean and mass-weighted median gas metallicity, respectively. The solid black line indicates the one-to-one relationship. \bar{Z}_{gas} , \bar{Z}_{gas} and $\bar{Z}_{\text{gas, MW}}$ of the galaxies are very similar to each other.

This paper has been typeset from a $\text{\TeX}/\text{\LaTeX}$ file prepared by the author.